



January 2012

Modal Testing And Analysis Techniques And Their Application On A Small Uas

Kaci Lemler

Follow this and additional works at: <https://commons.und.edu/theses>

Recommended Citation

Lemler, Kaci, "Modal Testing And Analysis Techniques And Their Application On A Small Uas" (2012). *Theses and Dissertations*. 1359.
<https://commons.und.edu/theses/1359>

This Thesis is brought to you for free and open access by the Theses, Dissertations, and Senior Projects at UND Scholarly Commons. It has been accepted for inclusion in Theses and Dissertations by an authorized administrator of UND Scholarly Commons. For more information, please contact zeinebyousif@library.und.edu.

MODAL TESTING AND ANALYSIS TECHNIQUES AND THEIR
APPLICATION ON A SMALL UAS

by

Kaci Jo Lemler
Bachelor of Science, University of North Dakota, 2011

A Thesis

Submitted to the Graduate Faculty

of the

University of North Dakota

in partial fulfillment of the requirements

for the degree of

Master of Science

Grand Forks, North Dakota

December

2012

Copyright 2012 Kaci J. Lemler

This thesis, submitted by Kaci J. Lemler in partial fulfillment of the requirements for the Degree of Master of Science from the University of North Dakota, has been read by the Faculty Advisory Committee under whom the work has been done and is hereby approved.

William Semke, Chairperson

Jeremiah Neubert

Marcellin Zahui

This thesis is being submitted by the appointed advisory committee as having met all of the requirements of the Graduate School of the University of North Dakota and is hereby approved.

Wayne Swisher
Dean of the Graduate School

Date

Title Modal Testing and Analysis Techniques and their Application on a Small UAS

Department Mechanical Engineering

Degree Master of Science

In presenting this thesis in partial fulfillment of the requirements for a graduate degree from the University of North Dakota, I agree that the library of this University shall make it freely available for inspection. I further agree that permission for extensive copying for scholarly purposes may be granted by the professor who supervised my thesis work or, in his absence, by the Chairperson of the department or the dean of the Graduate School. It is understood that any copying or publication or other use of this thesis or part thereof for financial gain shall not be allowed without my written permission. It is also understood that due recognition shall be given to me and to the University of North Dakota in any scholarly use which may be made of any material in my thesis.

Kaci Lemler
December 14, 2012

TABLE OF CONTENTS

LIST OF FIGURES	viii
LIST OF TABLES	xvi
ACKNOWLEDGEMENTS	xvii
ABSTRACT	xviii
CHAPTER	
I. INTRODUCTION	1
Description of Project	1
Need for Project	2
Unmanned Aircraft Systems Engineering	4
II. TEST OVERVIEW	7
Theory	7
Wing Pod Design	8
Testing Setup	10
Test Procedure	13
III. BASE MODEL	16
Test Description	16
Results	18

	Discussion.....	26
	Tests with Payload	27
IV.	CHANNEL REDUCTION	29
	Introduction.....	29
	Stick Model.....	30
	Test Description	30
	Results.....	30
	Discussion/Comparison	36
	Dangers of Channel Reduction	37
	Description	37
	Results and Discussion	39
	WHV Model.....	42
	Test Description	42
	Results.....	43
	Discussion/Comparison	48
	WH Model	49
	Test Description	49
	Results.....	50
	Discussion/Comparison	56
	W Model	57
	Test Description	57

	Results.....	58
	Discussion/Comparison	63
V.	SENSOR LOCATION IDENTIFICATION METHOD.....	64
	Introduction.....	64
	Test Description	65
	Results.....	67
	Statistical Method	71
VI.	DETERMINATION OF AIRWORTHINESS.....	76
	Flutter Overview	76
	Flutter Results	79
	Flight Test	80
VII.	CONCLUSION.....	82
	APPENDICES	85
	REFERENCES	106

LIST OF FIGURES

Figure	Page
1. Small unmanned aircraft system with wing pods installed (wing pods circled).....	2
2. Uninterrupted field of view from mounting antennas on the wings.	4
3. Unmanned Aircraft System Engineering team with the UAS they operate.....	5
4. Payload bay in the Super Hauler.....	6
5. Side view of wing payload pod.....	8
6. Wing payload pod with antenna array installed.....	9
7. Wing pods installed in the Super Hauler.	9
8. The Super Hauler in the test rig while instrumented with accelerometers.	10
9. The shaker setup with stinger, load cell, and suction cup.....	11
10. Shaker excitation locations.	12
11. National Instruments cDAQ-9178 data acquisition board used for the testing	12
12. Sample frequency response function with curve fit over the targeted mode.	15
13. Identifying multiple modes within a range in ModalVIEW.	15
14. Base model accelerometer locations (red = uni-axial, blue = tri-axial).....	16
15. Pod accelerometer locations.	18
16. Mode shape corresponding to a frequency of 12.4 Hz without pods (left) and 11.0 Hz with pods (right).....	19

17. Mode shape corresponding to a frequency of 17.3 Hz without pods (left) and 15.6 Hz with pods (right).....	19
18. Mode shape corresponding to a frequency of 20.8 Hz without pods (left) and 18.9 Hz with pods (right).....	20
19. Mode shape corresponding to a frequency of 26.7 Hz without pods.....	20
20. Mode shape corresponding to a frequency of 28.9 Hz without pods (left) and 20.6 Hz with pods (right).....	21
21. Mode shape corresponding to a frequency of 29.5 Hz without pods (left) and 23.2 Hz with pods (right).....	21
22. Mode shape corresponding to a frequency of 30.2 Hz without pods (left) and 24.8 Hz with pods (right).....	22
23. Mode shape corresponding to a frequency of 33.8 Hz without pods.....	22
24. Mode shape corresponding to a frequency of 39.9 Hz without pods.....	23
25. Mode shape corresponding to a frequency of 45.0 Hz without pods (left) and 34.0 Hz with pods (right).....	23
26. Mode shape corresponding to a frequency of 51.4 Hz without pods (left) and 38.3 Hz with pods (right).....	24
27. Mode shape corresponding to a frequency of 40.9 Hz with pods.....	24
28. Mode shape corresponding to a frequency of 63.7 Hz without pods (left) and 47.4 Hz with pods (right).....	25
29. Mode shape corresponding to a frequency of 72.3 Hz without pods.....	25
30. Mode shape corresponding to a frequency of 74.4 Hz without pods (left) and 53.6 Hz with pods (right).....	26
31. Stick model and accelerometer locations (red = uni-axial, blue = tri-axial).....	30
32. Mode shape corresponding to a frequency of 12.4 Hz for the stick model (left) and 12.4 Hz for the base model (right).	31
33. Mode shape corresponding to a frequency of 17.5 Hz for the stick model (left) and 17.3 Hz for the base model (right).	31

34. Mode shape corresponding to a frequency of 20.9 Hz for the stick model (left) and 20.8 Hz for the base model (right).	32
35. Mode shape corresponding to a frequency of 25.7 Hz for the stick model (left) and 26.7 Hz for the base model (right).	32
36. Mode shape corresponding to a frequency of 27.4 Hz for the stick model (left) and 28.9 Hz for the base model (right).	32
37. Mode shape corresponding to a frequency of 31.0 Hz for the stick model (left) and 30.2 Hz for the base model (right).	33
38. Mode shape corresponding to a frequency of 37.9 Hz for the stick model (left) and 33.8 Hz for the base model (right).	33
39. Mode shape corresponding to a frequency of 39.9 Hz for the stick model (left) and 39.9 Hz for the base model (right).	34
40. Mode shape corresponding to a frequency of 44.9 Hz for the stick model (left) and 45.0 Hz for the base model (right).	34
41. Mode shape corresponding to a frequency of 50.4 Hz for the stick model (left) and 51.4 Hz for the base model (right).	35
42. Mode shape corresponding to a frequency of 64.1 Hz for the stick model (left) and 63.7 Hz for the base model (right).	35
43. Mode shape corresponding to a frequency of 72.8 Hz for the stick model (left) and 72.3 Hz for the base model (right).	36
44. Mode shape corresponding to a frequency of 76.2 Hz for the stick model (left) and 74.4 Hz for the base model (right).	36
45. Impact hammer excitation locations and directions.....	38
46. PCB Piezotronics 086C03 impact hammer used for excitation.....	38
47. Mode shape corresponding to a frequency of 12 Hz without pods.....	40
48. Mode shapes corresponding to a frequency of 27 Hz without pods (left) and 11 Hz with pods (right).	40
49. Mode shapes corresponding to a frequency of 28 Hz without pods (left) and 13 Hz with pods (right).	40

50. Mode shapes corresponding to a frequency of 73 Hz without pods (left) and 20 Hz with pods (right).	40
51. Mode shapes corresponding to a frequency of 91 Hz without pods (left) and 28 Hz with pods (right).	41
52. WHV accelerometer locations.	42
53. Mode shape corresponding to a frequency of 12.4 Hz for WHV (left) and 12.4 Hz for the base model (right).	43
54. Mode shape corresponding to a frequency of 17.5 Hz for WHV (left) and 17.3 Hz for the base model (right).	43
55. Mode shape corresponding to a frequency of 20.8 Hz for WHV (left) and 20.8 Hz for the base model (right).	44
56. Mode shape corresponding to a frequency of 26.0 Hz for WHV (left) and 26.7 Hz for the base model (right).	44
57. Mode shape corresponding to a frequency of 28.2 Hz for WHV (left) and 28.9 Hz for the base model (right).	45
58. Mode shape corresponding to a frequency of 30.8 Hz for WHV (left) and 30.2 Hz for the base model (right).	45
59. Mode shape corresponding to a frequency of 36.5 Hz for WHV (left) and 33.8 Hz for the base model (right).	45
60. Mode shape corresponding to a frequency of 39.7 Hz for WHV (left) and 39.9 Hz for the base model (right).	46
61. Mode shape corresponding to a frequency of 44.9 Hz for WHV (left) and 45.0 Hz for the base model (right).	46
62. Mode shape corresponding to a frequency of 51.0 Hz for WHV (left) and 51.4 Hz for the base model (right).	47
63. Mode shape corresponding to a frequency of 61.1 Hz for WHV (left) and 63.7 Hz for the base model (right).	47
64. Mode shape corresponding to a frequency of 73.3 Hz for WHV (left) and 72.3 Hz for the base model (right).	48

65. Mode shape corresponding to a frequency of 75.9 Hz for WHV (left) and 74.4 Hz for the base model (right).....	48
66. WH accelerometer locations.....	50
67. Mode shape corresponding to a frequency of 12.4 Hz for WH (left) and 12.4 Hz for the base model (right).....	50
68. Mode shape corresponding to a frequency of 17.5 Hz for WH (left) and 17.3 Hz for the base model (right).....	51
69. Mode shape corresponding to a frequency of 20.8 Hz for WH (left) and 20.8 Hz for the base model (right).....	51
70. Mode shape corresponding to a frequency of 26.0 Hz for WH (left) and 26.7 Hz for the base model (right).....	52
71. Mode shape corresponding to a frequency of 28.1 Hz for WH (left) and 28.9 Hz for the base model (right).....	52
72. Mode shape corresponding to a frequency of 30.8 Hz for WH (left) and 30.2 Hz for the base model (right).....	53
73. Mode shape corresponding to a frequency of 36.1 Hz for WH (left) and 33.8 Hz for the base model (right).....	53
74. Mode shape corresponding to a frequency of 39.8 Hz for WH (left) and 39.9 Hz for the base model (right).....	53
75. Mode shape corresponding to a frequency of 44.9 Hz for WH (left) and 45.0 Hz for the base model (right).....	54
76. Mode shape corresponding to a frequency of 51.7 Hz for WH (left) and 51.4 Hz for the base model (right).....	54
77. Mode shape corresponding to a frequency of 62.9 Hz for WH (left) and 63.7 Hz for the base model (right).....	55
78. Mode shape corresponding to a frequency of 72.0 Hz for WH (left) and 72.3 Hz for the base model (right).....	55
79. Mode shape corresponding to a frequency of 75.9 Hz for WH (left) and 74.4 Hz for the base model (right).....	56

80. W accelerometer locations.....	57
81. Mode shape corresponding to a frequency of 12.4 Hz for W (left) and 12.4 Hz for the base model (right).....	58
82. Mode shape corresponding to a frequency of 17.5 Hz for W (left) and 17.3 Hz for the base model (right).....	58
83. Mode shape corresponding to a frequency of 21.0 Hz for W (left) and 20.8 Hz for the base model (right).....	59
84. Mode shape corresponding to a frequency of 25.9 Hz for W (left) and 26.7 Hz for the base model (right).....	59
85. Mode shape corresponding to a frequency of 28.1 Hz for W (left) and 28.9 Hz for the base model (right).....	60
86. Mode shape corresponding to a frequency of 30.7 Hz for W (left) and 30.2 Hz for the base model (right).....	60
87. Mode shape corresponding to a frequency of 39.8 Hz for W (left) and 39.9 Hz for the base model (right).....	60
88. Mode shape corresponding to a frequency of 44.7 Hz for W (left) and 45.0 Hz for the base model (right).....	61
89. Mode shape corresponding to a frequency of 50.6 Hz for W (left) and 51.4 Hz for the base model (right).....	61
90. Mode shape corresponding to a frequency of 64.1 Hz for W (left) and 63.7 Hz for the base model (right).....	62
91. Mode shape corresponding to a frequency of 71.9 Hz for W (left) and 72.3 Hz for the base model (right).....	62
92. Mode shape corresponding to a frequency of 75.8 Hz for W (left) and 74.4 Hz for the base model (right).....	62
93. Laser vibrometer testing setup.....	66
94. Excitation (blue) and measurement (red) locations for laser vibrometer tests.	67
95. Sample data from the laser vibrometer.....	68

96. (a) Raw laser vibrometer data. (b) Data with outliers removed and adjusted for an average of zero.	69
97. A zoomed in graph of Figure 96 (b).	70
98. Average RMS values for laser vibrometer measurement locations with 95% confidence intervals.	71
99. Pareto diagram for laser vibrometer test.	73
100. The Super Hauler in flight with the wing pods installed.	81
101. Main window for ModalVIEW.	86
102. 3D Structure Model window.	87
103. Initial point placement in Structure 3D View window.	88
104. Setting coordinates for the points in the structure.	89
105. Adding lines to the structure.	89
106. Completed structure.	90
107. Performing Measurement window.	91
108. Selecting the DAQ.	91
109. DAQ Setup window.	92
110. DAQ Setup window, Acquisition tab.	93
111. Test Setup window.	94
112. Test Setup window, Post-process tab.	95
113. Test Setup window, Measurement Sets tab.	96
114. Channels generated in the Measurement Sets tab.	97
115. Appropriate DOFs selected in Measurement Sets tab.	98
116. Signal Generator Excitation window.	99
117. Signal options in Excitation window.	100

118. Experimental or Operational Modal Analysis window.	101
119. Measurement bounds.	102
120. Estimated curve fit.	103
121. Good curve fit in modal estimation.	103
122. Further modal analysis.	104
123. Modal Shape Animation window.	105

LIST OF TABLES

Table	Page
1. Test equipment information.....	13
2. Summarized natural frequencies (Hz) and damping ratios (%) for the base model with and without pods and percent difference between natural frequencies.	26
3. Summary of natural frequencies for unloaded and loaded configurations.	28
4. Stick model natural frequency summary.	37
5. Summary of preliminary test natural frequencies.	39
6. Adjusted preliminary test mode identification.....	41
7. WHV natural frequency summary.....	49
8. WH natural frequency summary.....	56
9. W natural frequency summary.....	63
10. Data used to create the Pareto diagram.....	73
11. Summary of natural frequencies.	74
12. Summary of wing modes.	80
13. Summary of potential horizontal stabilizer flutter modes.....	80

ACKNOWLEDGEMENTS

I would like to thank my advisor, Dr. William Semke, for all of his support and efforts during my time as a student at the University of North Dakota. I would also like to thank my committee members, Dr. Jeremiah Neubert and Dr. Marcellin Zahui, for their input throughout my research.

This research was supported in part by Department of Defense contract number FA4861-06-C-C006, "Unmanned Aerial System Remote Sense and Avoid System and Advanced Payload Analysis and Investigation," the Air Force Research Laboratory, "MEMS Antenna for Wireless Communications Supporting Unmanned Aerial Vehicles in the Battlefield," and the North Dakota Department of Commerce, "UND Center of Excellence for UAV and Simulation Applications." Additionally, I must thank the Unmanned Aircraft Systems Engineering (UASE) Laboratory team members who have helped me throughout this process and have made my experience at UND one that I will never forget.

Finally, a special thanks needs to be given to my family and friends, especially my parents, Dan and Inger, and my sister, Jessi, for their unwavering support throughout my entire college career. I could not have done it without them.

ABSTRACT

This thesis focuses on experimental structural analysis using contemporary testing techniques. This includes modal testing topics such as data acquisition, data processing, sensor placement, and multiple excitation methods. It also presents a novel sensor placing procedure that uses a laser vibrometer to identify key sensor locations. These techniques are applied in a case study on a small unmanned aerial system, (UAS). The airframe, the BTE Super Hauler, is a small UAS used by the Unmanned Aircraft Systems Engineering (UASE) Laboratory at the University of North Dakota as a test platform for flight testing multiple payloads. An antenna system, designed for use in sense and avoid applications, was developed that requires the addition of wing pods to the current airframe to minimize electro-magnetic interference from the engine of the UAS. Modal testing is used to determine the effect of two wing pods on the structural dynamic behavior of the UAS. Flutter analysis is also performed to ensure that the surface bending and torsional modes of the UAS do not create an unstable airframe.

Data acquisition was performed using ModalVIEW, a structural analysis program supported by LabVIEW. ModalVIEW outputs a frequency response function to which various windowing methods can be applied. The aircraft was excited both by an impact hammer and a shaker.

The new sensor placement procedure was developed to assist in placing sensors in key locations in an efficient method to reduce the number of channels needed. It is also a fast, non-contact method implementing a laser vibrometer. A statistical method was used to determine appropriate sensor locations.

CHAPTER I

INTRODUCTION

Description of Project

Modal analysis is the study of the vibration modes and natural frequencies of a structure. Modal analysis is essential to a full understanding of a structure's vibration characteristics. This is an especially important step in the development of aircraft as vibration can be a large factor in the safety and structural integrity. Not only should modal analysis be performed in the development of a new aircraft, but it is necessary when structural changes are made on an existing aircraft.

Modal analysis on a small Unmanned Aircraft System (UAS) was made necessary by the addition of wing pods. Modal analysis was performed both with and without the wing pods and the results were compared to identify the effect the wing pods have on the vibration characteristics of the UAS. The UAS with the wing pods installed can be seen in Figure 1.

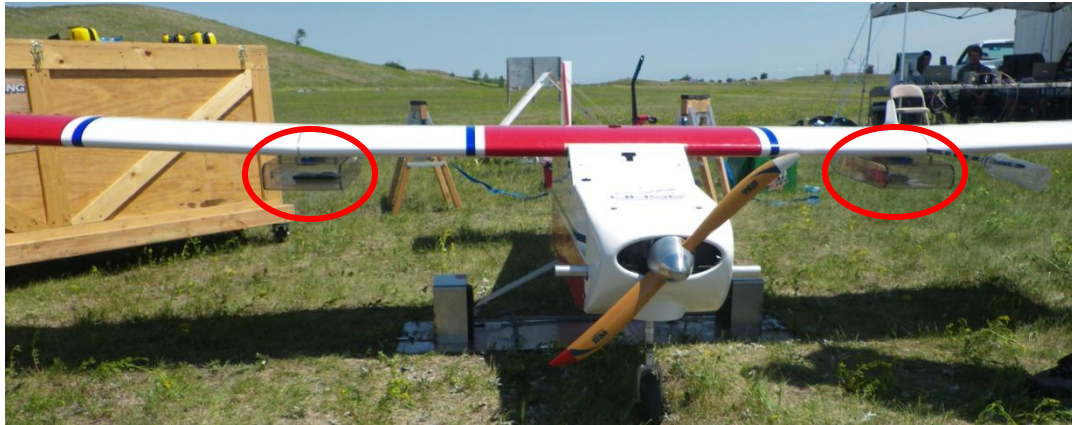


Figure 1. Small unmanned aircraft system with wing pods installed (wing pods circled).

It is desirable to use as few sensors as possible in modal analysis. Because of this, channel reduction was investigated as well. Several tests were performed that had different types and levels of channel reduction and the results were compared to a base test to analyze which setups still captured all of the necessary information.

There are several existing sensor placement techniques but they generally use complex and time consuming models. A novel experimental sensor placement method was developed that uses a laser vibrometer to quickly and easily identify important sensor locations. Important sensor locations were identified from the laser vibrometer data through the use of a Pareto diagram.

Need for Project

As UAS are being integrated into the National Air Space it is important that steps be taken to develop and implement sense and avoid systems into said UAS [1]. These systems are necessary to enable UAS to sense and avoid obstacles such as uncooperative aircraft, birds, power lines, buildings, and other obstacles [2].

The Unmanned Systems Aircraft Engineering (UASE) team at the University of North Dakota has done work in the field of sense and avoid systems for small UAS. One system that was developed uses an Automatic Dependent Surveillance-Broadcast (ADS-B) transponder to track cooperative aircraft that also have ADS-B transponders. This system works well to predict and avoid collision scenarios with cooperative aircraft but doesn't assist in sense and avoid applications for uncooperative obstacles. Because of this, work is also being done on a small phased array radar system that can be installed into the small UAS along with the ADS-B to provide the ability to track uncooperative obstacles as well as cooperative.

This phased array radar system includes an antenna that locates objects by radiating a narrow beam of electromagnetic energy in the direction of interest [2]. This beam is also steerable so that it can locate objects at all locations around the UAS. Because this antenna radiates electromagnetic energy, it needs to have a clear field of view, containing no metal components, between it and its target [3]. This introduces a need to mount the antennas on the wings to reduce the effect of the engine, landing gear, and assorted fuselage components that could block the view of the antennas if mounted in the fuselage. An illustration of this is shown in Figure 2. The use of wing pods reduces any unwanted view interference and provides a payload bay on the wings in which to mount the antennas.

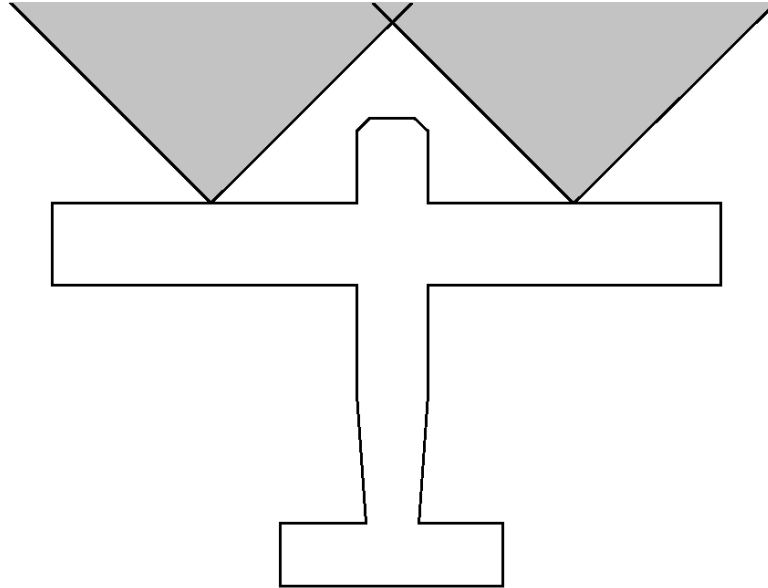


Figure 2. Uninterrupted field of view from mounting antennas on the wings.

The wing pods can dramatically change the structural and flight characteristics of the aircraft. This change in the characteristics could result in the introduction of flutter, a potentially catastrophic phenomenon where the aerodynamic forces drive bending and torsion motion on a flight surface. This behavior can be observed through experimental structural analysis. Therefore, a study on the structural analysis of the Super Hauler, both with and without the wing pods installed, is necessary to prove airworthiness of the modified aircraft. An in-depth discussion on flutter can be found in Chapter VI.

Unmanned Aircraft Systems Engineering

The UASE team consists of a combination of undergraduate and graduate students in mechanical engineering and electrical engineering. The purpose of the lab is to design, build, and test payloads for UAS.



Figure 3. Unmanned Aircraft System Engineering team with the UAS they operate.

UASE has performed over 80 missions and has developed payloads relating to phased array radar, search and rescue, precision agriculture, sense and avoid, laser communications, and more. Flight testing is performed at Camp Grafton South, a military training facility in central North Dakota. This facility has restricted airspace, allowing UASE to safely and legally operate its UAS fleet.

UASE operates multiple UAS, one of which is the Bruce Tharpe Engineering Super Hauler, (henceforth referred to as the Super Hauler). The Super Hauler is the red and white aircraft in Figure 3 and is a gas powered UAS constructed of plywood, balsa wood, and Monokote. It has a 12 foot wingspan and a dry weight of 48 pounds. The engine is a 2-cylinder, 9.8 horsepower Desert Aircraft engine. The Super Hauler is capable of carrying payloads that weigh up to 30 pounds and has an electromagnetically shielded payload bay measuring 21 inches by 11 inches by 12 inches which can be seen in Figure 4.



Figure 4. Payload bay in the Super Hauler.

The following chapters will discuss the modal testing performed on the Super Hauler. Chapter 2 will discuss in detail the test setup and procedure of the modal tests. Chapter 3 presents the results from the modal testing using a base model of the Super Hauler. Chapter 4 enters into a study on channel reduction and examines several different tests that were performed to analyze the effects of channel reduction. A novel sensor location identification method is presented in Chapter 5. Finally, the effects of the wing pods on the airworthiness of the Super Hauler are discussed in Chapter 6.

CHAPTER II

TEST OVERVIEW

Theory

The structural modes and natural frequencies of a structure can be obtained through ground vibration tests (GVTs). GVTs are important tests to perform on an aircraft because they are used to predict flutter and assess the significance of modifications made to the structure [4].

The main tool used in a GVT is the frequency response function (FRF). This function can be based on the displacement, velocity, or acceleration response of a system to an applied force [5]. The expression for any FRF can be written as

$$H_{jk}(\omega) = \frac{X_j}{F_k} \quad (1)$$

where X_j is the harmonic response in one of the degrees of freedom, j , caused by F_k which is a harmonic force at a different degree of freedom, k [6]. Modal analysis is performed by curve-fitting the FRF obtained from the testing to obtain modes then applying that data to a model of the structure to find the associated mode shapes.

A method of checking the quality of a mode is the Modal Assurance Criterion (MAC). It is mainly used to compare mode shapes obtained from experiments to those from analytical models such as finite element models [7]. The MAC represents the

normalized least squares deviation from the best straight line fitted to the data of corresponding vector entries in the mode shapes [8]. The value of the MAC can be calculated from

$$MAC_{jk} = \frac{|\phi_{mj}^T \phi_{ak}|^2}{(\phi_{ak}^T \phi_{ak})(\phi_{mj}^T \phi_{mj})} \quad (2)$$

where ϕ_{mj} is a measured mode and ϕ_{ak} is an analytical mode [7]. The MAC varies from 0 to 1 where 0 indicates no correspondence and 1 indicates consistent correspondence [9].

Wing Pod Design

As stated previously, the modal analyses were made necessary by the addition of wing pods to the Super Hauler. The wing pods used to hold the antennas were designed and built by members of UASE. The pods are made entirely of polycarbonate to eliminate any electromagnetic interference [3]. The aerodynamic shape of the pods results in less drag which decreases the effect of the pods on flight performance.

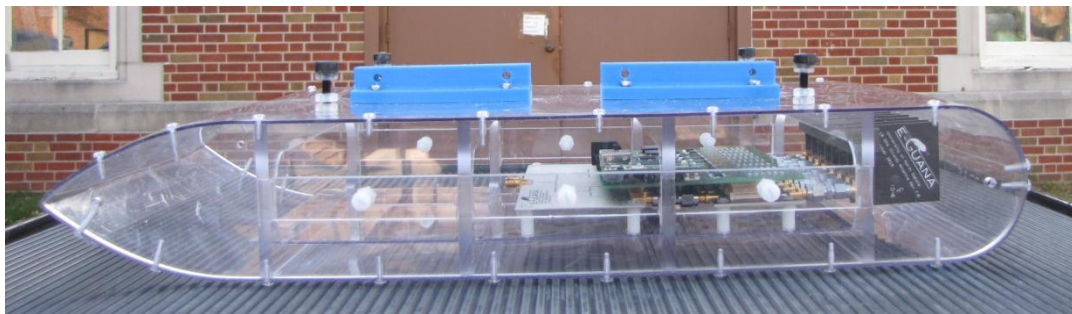


Figure 5. Side view of wing payload pod.

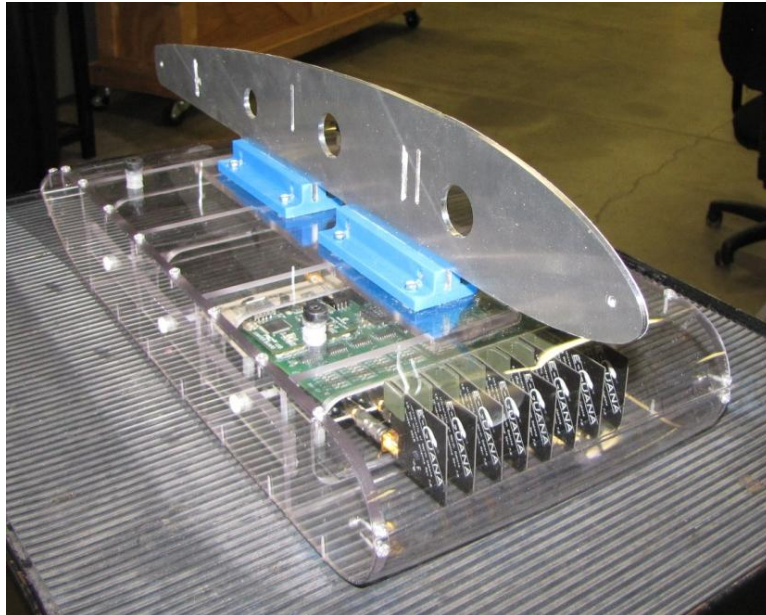


Figure 6. Wing payload pod with antenna array installed.

The payload pods mount at the intersections of the wing segments using an aluminum mounting rib that follows the contour of the wing at this location. The overall dimensions of the pods are 7.75 inches long by 11 inches wide by 2.5 inches deep and each pod can carry up to 5 pounds.



Figure 7. Wing pods installed in the Super Hauler.

The pods will most often be used in pairs to equalize the wing loading and provide a symmetric load on the airframe. Any electrical and power connectors and wiring will be routed inside of the wing to keep them out of the airflow over the wing.

Testing Setup

The Super Hauler was isolated by suspending it on bungee cords in a test rig so that all the wheels were 1.25 inches off of the ground. This setup simulates a free-free boundary condition for modal testing [10]. The Super Hauler was then instrumented with uni-axial and tri-axial accelerometers in key locations. The instrumented Super Hauler in the test rig can be seen in Figure 8.



Figure 8. The Super Hauler in the test rig while instrumented with accelerometers.

Excitation of the Super Hauler was achieved by a small shaker. The shaker that was used was the Mini SmartShaker™ with an integrated power amplifier from The Modal Shop Inc. The setup of the shaker can be seen in Figure 9 where it was attached to the aircraft through the use of a suction cup.



Figure 9. The shaker setup with stinger, load cell, and suction cup.

A load cell was attached in line with the shaker's stinger to measure input force. The aircraft was excited at several different locations, all in the Z direction, that are identified by the red dots in Figure 10.

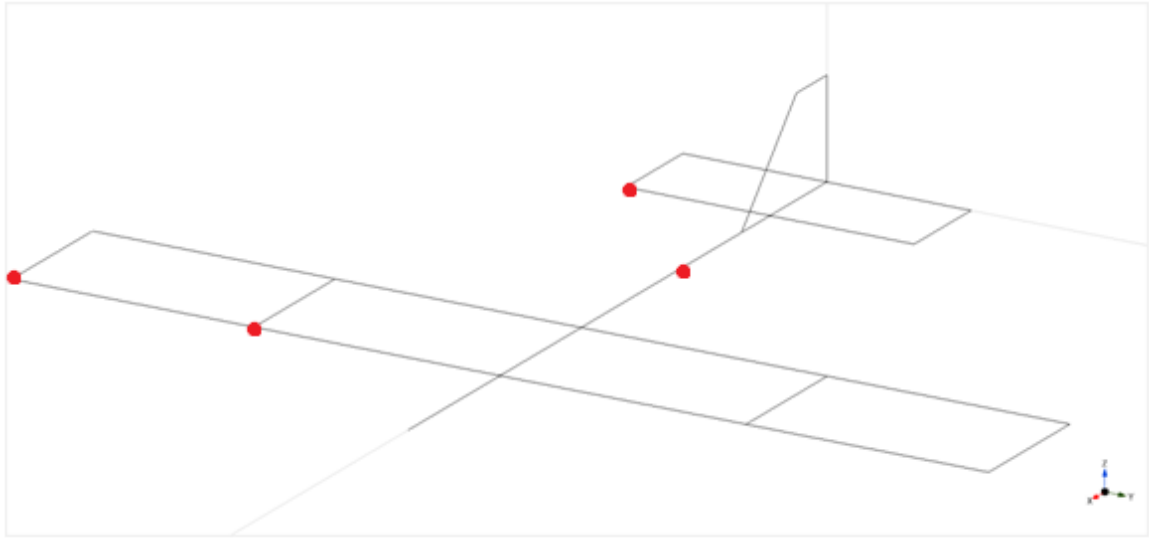


Figure 10. Shaker excitation locations.

The accelerometers and excitation devices were routed through a National Instruments data acquisition board that was connected directly to a computer. This board can be seen in Figure 11.



Figure 11. National Instruments cDAQ-9178 data acquisition board used for the testing

Data capture and analysis was performed using ModalVIEW, a software designed specifically for modal testing and analysis. Information on the equipment that was used is shown in Table 1.

Table 1. Test equipment information.

Description	Model	Sensitivity	Resolution
Uni-axial Accelerometer	PCB Piezotronics 352C18	10 mV/g	0.0005 g
Uni-axial Accelerometer	PCB Piezotronics 352C33	100 mV/g	0.00015 g
Tri-axial Accelerometer	PCB Piezotronics 356A32	100 mV/g	0.0003 g
Load Cell	PCB Piezotronics 208C02	50 mV/g	0.0004 g
Shaker	The Modal Shop Inc. K2007E01	-	-
Data Acquisition Board	National Instruments cDAQ-9178	-	-
Data Acquisition Module	National Instruments 9234	-	-

Tests were performed with and without the wing pods installed. For all of the tests with the pods, weight was added to the pods so that a total weight of 5 pounds was attached to each wing. There was no payload in the payload bay during the testing.

Test Procedure

The settings in ModalVIEW were as follows. The shaker was set to random excitation with an amplitude setting of 0.3 with a Hanning window applied. The amplitude of excitation was chosen to be an amplitude that provided enough excitation while not being so large that it would cause damage to the shaker or the aircraft. The measurement type was set to FRF-EMA for an experimental modal analysis. The sampling rate was left at the default of 1651.61 Hz with the resolution set to 0.1 Hz. ModalVIEW automatically selects a sampling duration based on the resolution so all the user has to do is tell it to start collecting data and it will stop sampling and open a dialog

window when it has collected enough data to obtain the resolution specified by the user. This resolution, combined with the lowest accelerometer resolution through a root of sum of squares calculation, results in an overall system resolution of 0.10000045 which we will round to 0.1. Thus, all results are presented out to the tenths digit. It can be seen that the system resolution is dominated by the resolution that is set in ModalVIEW so this value should be set to a resolution that is acceptable for the tests.

The shaker was activated so that the Super Hauler was excited with random excitation. ModalVIEW was then prompted to record data from the accelerometers and when ModalVIEW was done sampling the shaker was turned off. This was repeated so that two data sets were gathered at each loading and excitation configuration then the shaker was moved to the next excitation location and the process was rerun.

Once all of the vibration data was gathered, analysis was performed using ModalVIEW and followed the steps outlined below. First, ModalVIEW automatically generated FRFs from the data for each channel. A curve could then be fit to the FRF to find the modes by selecting a frequency range for ModalVIEW to analyze and the number of modes within that range. This can be seen in Figure 12. The ranges selected varied and depended on the curve. The ranges were chosen so that a good curve fit could be obtained. If there was a good curve fit the mode(s) would then be added to the mode list for that test.

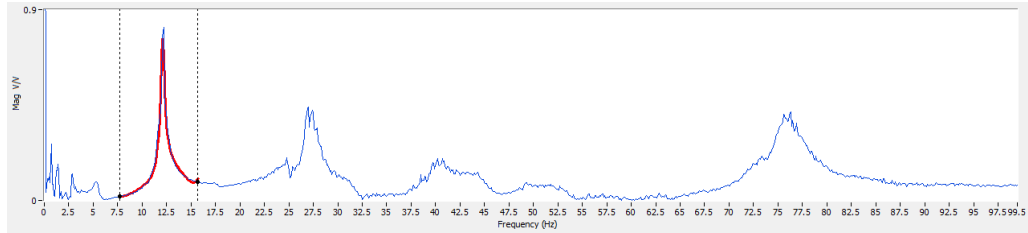


Figure 12. Sample frequency response function with curve fit over the targeted mode.

An example of using ModalVIEW to identify more than one mode within a range can be seen in Figure 13. The FRFs were analyzed in this manner until a list of modes and natural frequencies was created for each test. Each FRF was analyzed to find the modes that lay within 0 Hz to 80 Hz. This range was chosen because the lower frequencies are the ones of interest but, since the operating frequency of the aircraft is unknown, the range needed to be large enough to capture all potential operating frequencies.

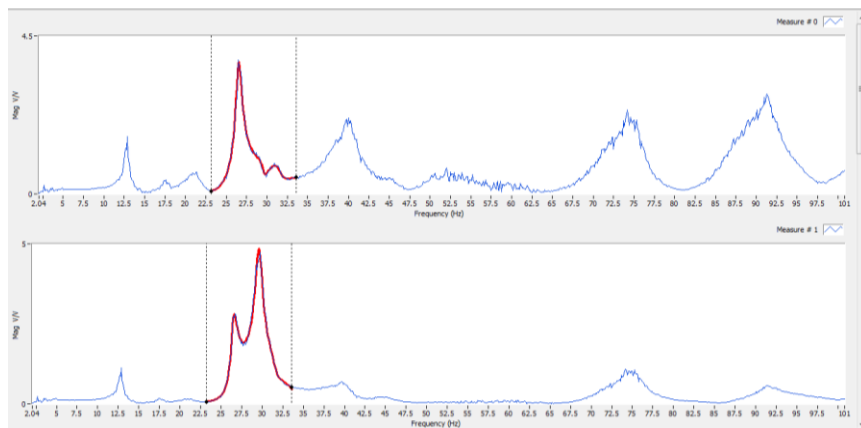


Figure 13. Identifying multiple modes within a range in ModalVIEW.

ModalVIEW was then used to build a model of the Super Hauler. The accelerometers were assigned to their respective nodes and degrees of freedom. The structure could then be animated with the motion and mode shape associated with each natural frequency that was found.

CHAPTER III

BASE MODEL

Test Description

The base model consisted of a planar model of the aircraft with 12 uni-axial accelerometers and 4 tri-axial accelerometers in the locations shown in Figure 14. All of the uni-axial accelerometers were mounted to measure acceleration in the Z direction except for the one on the vertical stabilizer, which was mounted to measure in the Y direction.

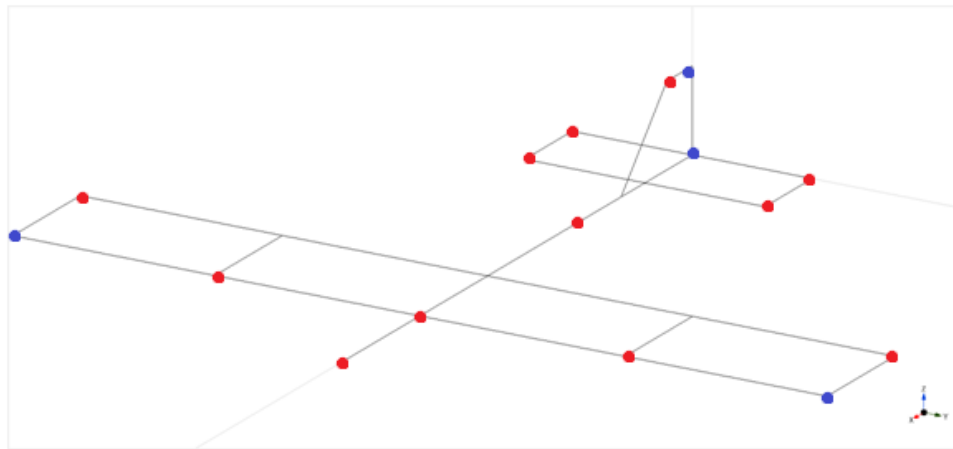


Figure 14. Base model accelerometer locations (red = uni-axial, blue = tri-axial).

Proper sensor placement is a major topic in modal analysis. There is a balance to strike between having a limited number of sensors and placing sensors on most of the structure to capture all of the modes. Most sensor placement methods use complex

computer or mathematical modeling to identify important locations to place sensors. A discussion on several methods that have been developed for optimal sensor placement can be found in Chapter V. However, adequate sensor locations can be identified more simply through a knowledge of similar structures. This was the approach taken in placing the sensors for the base model. The placement locations were chosen based on a combination of an understanding of traditional aircraft motion and some preliminary testing that was performed. A literature review showed that the primary motion is bending and torsion in the wings with motion also occurring in the horizontal and vertical stabilizers and the fuselage [5, 11, 12]. Also, to identify torsion motion for use in flutter analysis, sensors needed to be placed on the front and back of the wings and horizontal stabilizer. The sensor locations decided upon for the base model are not optimized or ideal locations but provide an adequate base for the testing.

The test was performed both with and without pods. When the pods were installed four more uni-axial accelerometers were added to measure the motion of the pods. The pod accelerometer locations are shown in Figure 15 where the two on the side of the pod were mounted in the Y direction and the two on the bottom of the pod were mounted in the Z direction.

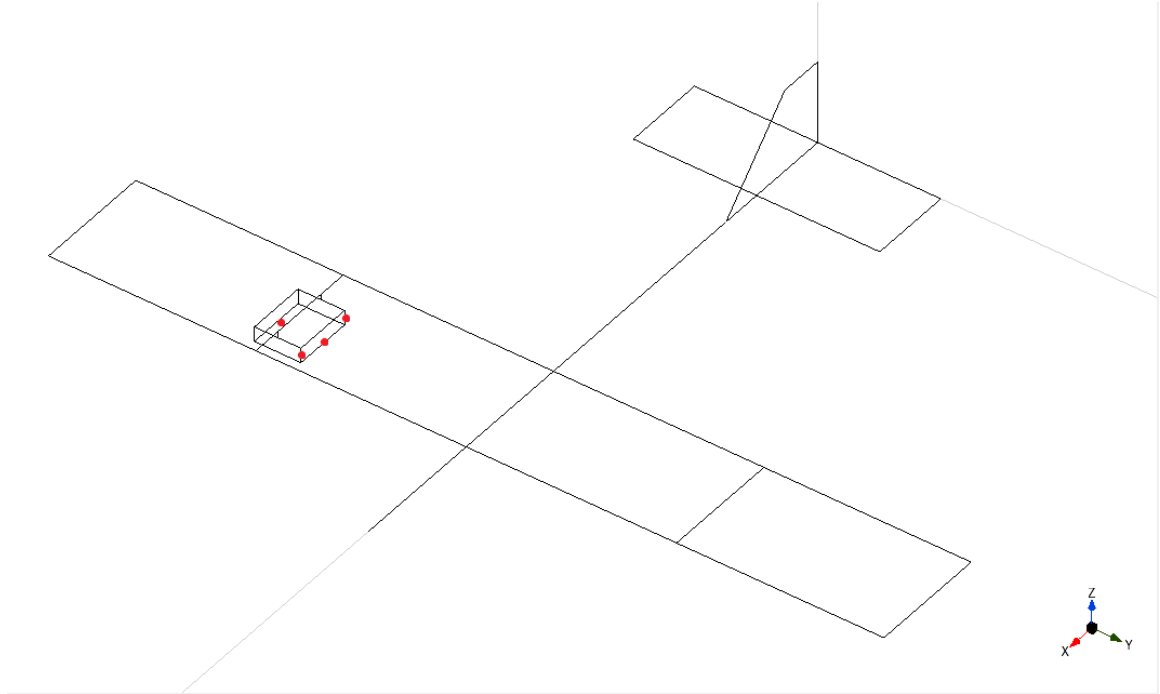


Figure 15. Pod accelerometer locations.

The shaker was used to excite the aircraft at the excitation locations shown in Figure 10 with two tests being performed at each of the four excitation locations and two loading conditions (pods and no pods). This gives a total of 16 tests in the base model configuration. The natural frequencies presented are the average of eight tests. These eight tests are comprised of two tests at each of the four excitation locations.

Results

The first mode shape that was observed was mode 1 type bending in the wings. This mode corresponded to natural frequencies of 12.4 Hz without the pods installed and 11.0 Hz when the pods were installed. A representation of this mode shape can be seen in Figure 16.

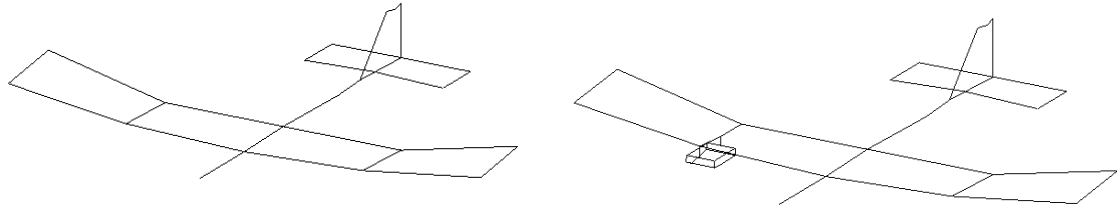


Figure 16. Mode shape corresponding to a frequency of 12.4 Hz without pods (left) and 11.0 Hz with pods (right).

The second mode shape consisted of tail torsion while the wingtips bent in opposite directions of each other. This mode corresponded to natural frequencies of 17.3 Hz without pods and 15.6 Hz with pods. A representation of this mode shape can be seen in Figure 17.

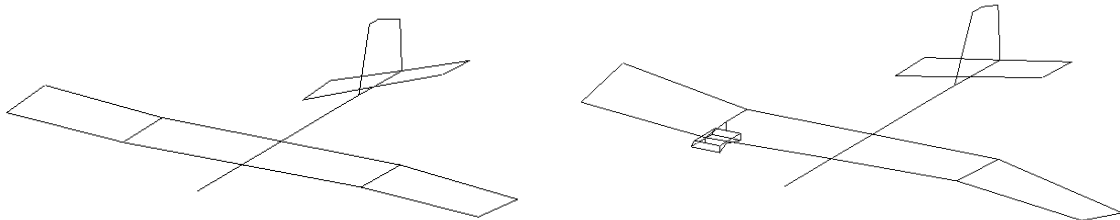


Figure 17. Mode shape corresponding to a frequency of 17.3 Hz without pods (left) and 15.6 Hz with pods (right).

The third mode shape showed wingtip, wing, tail, horizontal stabilizer, and vertical stabilizer torsion while the wingtips also bent. This mode corresponded to natural frequencies of 20.8 Hz without pods and 18.9 Hz with pods. A representation of this mode shape can be seen in Figure 18.

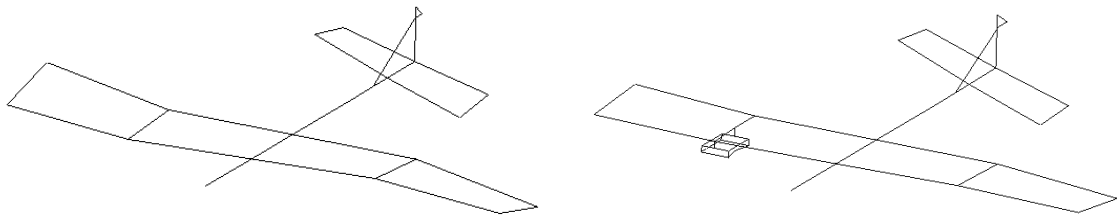


Figure 18. Mode shape corresponding to a frequency of 20.8 Hz without pods (left) and 18.9 Hz with pods (right).

The fourth mode shape only appeared in the no pods configuration. This mode consisted of wing torsion while the horizontal stabilizer bent slightly. It corresponded to a natural frequency of 26.7 Hz. A representation of this mode shape can be seen in Figure 19.

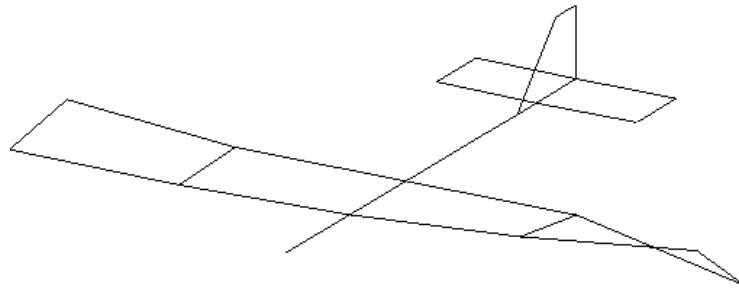


Figure 19. Mode shape corresponding to a frequency of 26.7 Hz without pods.

The fifth mode shape showed wing torsion in the same direction. This mode corresponded to natural frequencies of 28.9 Hz without pods and 20.6 Hz with pods. A representation of this mode shape can be seen in Figure 20.

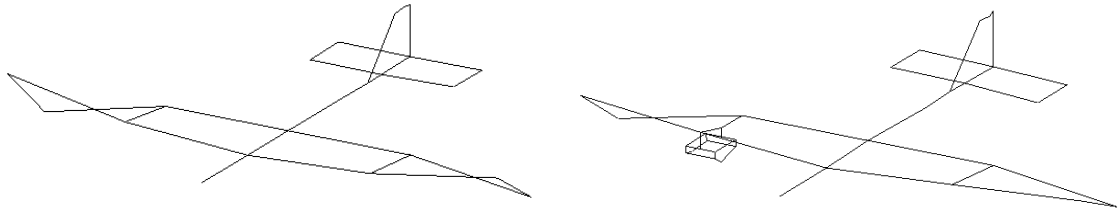


Figure 20. Mode shape corresponding to a frequency of 28.9 Hz without pods (left) and 20.6 Hz with pods (right).

The sixth mode shape showed the wingtips bending in opposite directions of each other while the tail moved side to side and the horizontal stabilizer underwent torsion and bending. The horizontal stabilizer showed signs of flutter but all discussions of flutter will be reserved for Chapter VI. This mode corresponded to natural frequencies of 29.5 Hz without pods and 23.2 Hz with pods. A representation of this mode shape can be seen in Figure 21.

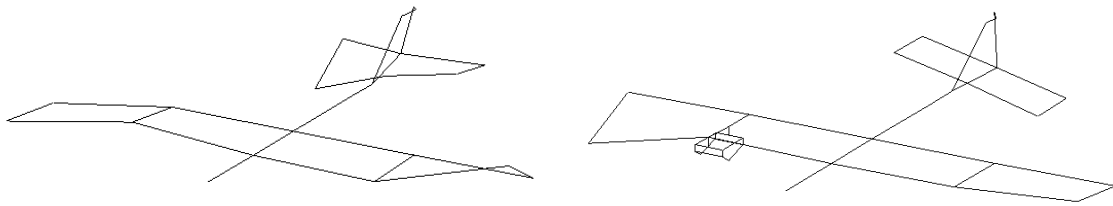


Figure 21. Mode shape corresponding to a frequency of 29.5 Hz without pods (left) and 23.2 Hz with pods (right).

The seventh mode shape showed the wingtips bending in opposite directions of each other while the tail moved side to side. This mode corresponded to natural frequencies of 30.2 Hz without pods and 24.8 Hz with pods. A representation of this mode shape can be seen in Figure 22.

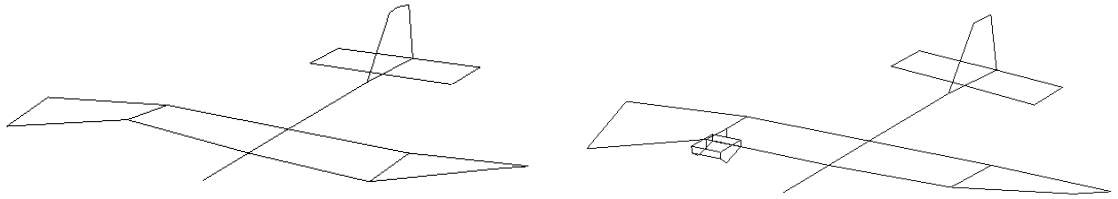


Figure 22. Mode shape corresponding to a frequency of 30.2 Hz without pods (left) and 24.8 Hz with pods (right).

The eighth mode shape showed horizontal and vertical stabilizer torsion. This mode only appeared in the no pods configuration and corresponded to a natural frequency of 33.8 Hz. A representation of this mode shape can be seen in Figure 23.

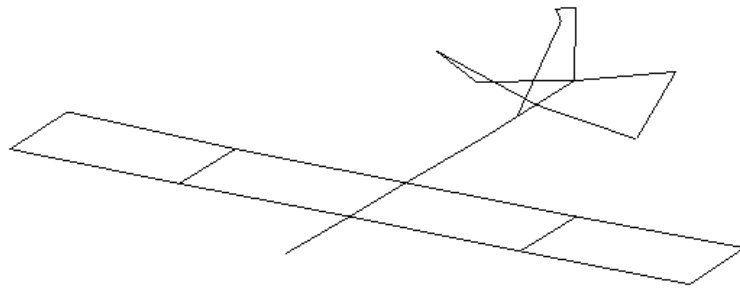


Figure 23. Mode shape corresponding to a frequency of 33.8 Hz without pods.

The ninth mode shape showed the horizontal stabilizer under bending and torsion with mode 2 bending in the wings and vertical stabilizer torsion. This mode was only visible in the no pod configuration and corresponded to a natural frequency of 39.9 Hz. A representation of this mode shape can be seen in Figure 24.

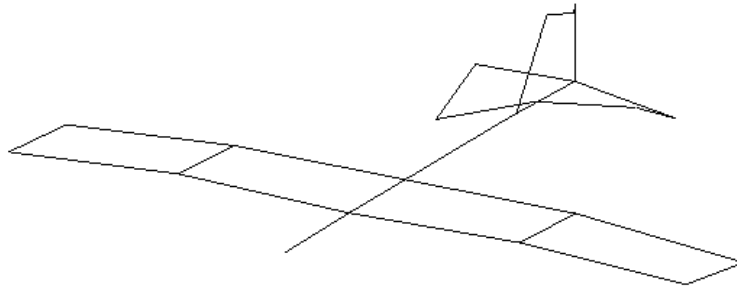


Figure 24. Mode shape corresponding to a frequency of 39.9 Hz without pods.

The tenth mode shape showed the wings experiencing mode 2 type bending with horizontal stabilizer bending and torsion. This mode corresponded to natural frequencies of 45.0 Hz without pods and 34.0 Hz with pods. A representation of this mode shape can be seen in Figure 25.

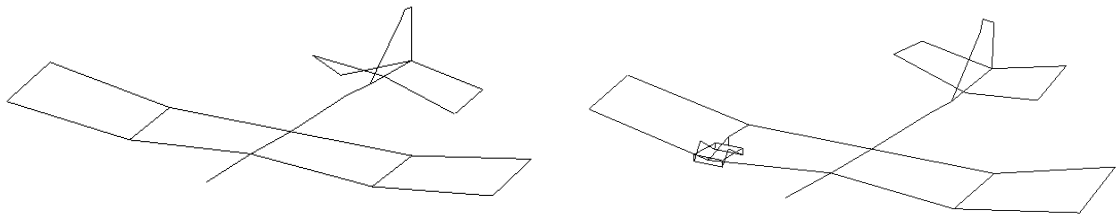


Figure 25. Mode shape corresponding to a frequency of 45.0 Hz without pods (left) and 34.0 Hz with pods (right).

The eleventh mode shape showed wing and horizontal stabilizer torsion in the same direction. This mode corresponded to natural frequencies of 51.4 Hz without pods and 38.3 Hz with pods. A representation of this mode shape can be seen in Figure 26.

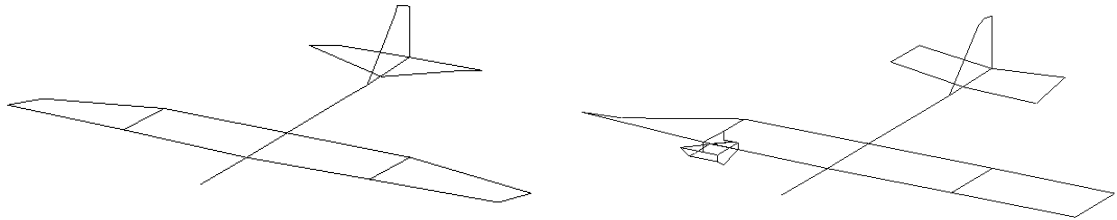


Figure 26. Mode shape corresponding to a frequency of 51.4 Hz without pods (left) and 38.3 Hz with pods (right).

The twelfth mode shape only appeared with the pods and showed the wings in torsion and the horizontal stabilizer in bending and torsion. This mode corresponded to a natural frequency of 40.9 Hz. A representation of this mode shape can be seen in Figure 27.

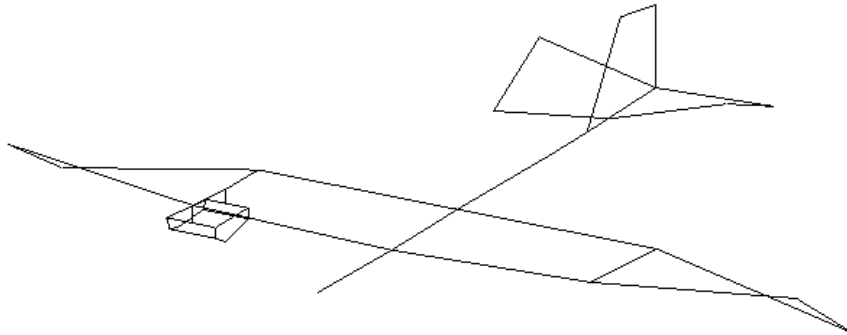


Figure 27. Mode shape corresponding to a frequency of 40.9 Hz with pods.

The thirteenth mode shape showed wing torsion in opposite directions from each other while the horizontal stabilizer and the fuselage both bent. This mode corresponded to natural frequencies of 63.7 Hz without pods and 47.4 Hz with pods. A representation of this mode shape can be seen in Figure 28.

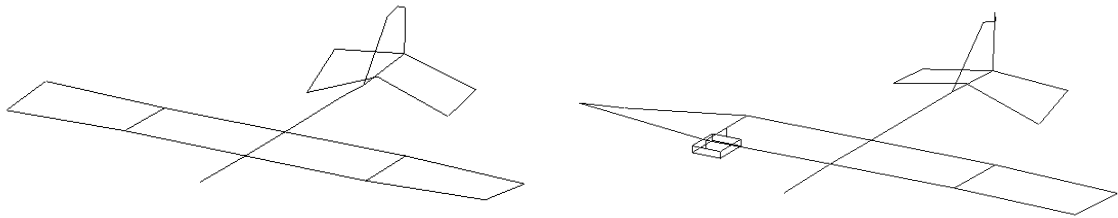


Figure 28. Mode shape corresponding to a frequency of 63.7 Hz without pods (left) and 47.4 Hz with pods (right).

The fourteenth mode shape only appeared without the pods and showed the wings undergoing mode 2 bending and torsion and the horizontal stabilizer in torsion. This mode corresponded to a natural frequency of 72.3 Hz. A representation of this mode shape can be seen in Figure 29.

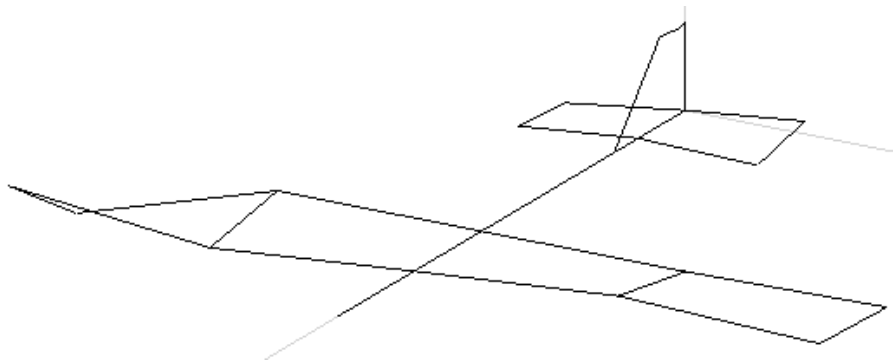


Figure 29. Mode shape corresponding to a frequency of 72.3 Hz without pods.

The fifteenth mode shape showed horizontal stabilizer torsion while the wings underwent mode 2 wing torsion. This mode corresponded to natural frequencies of 74.4 Hz without pods and 53.6 Hz with pods. A representation of this mode shape can be seen in Figure 30.

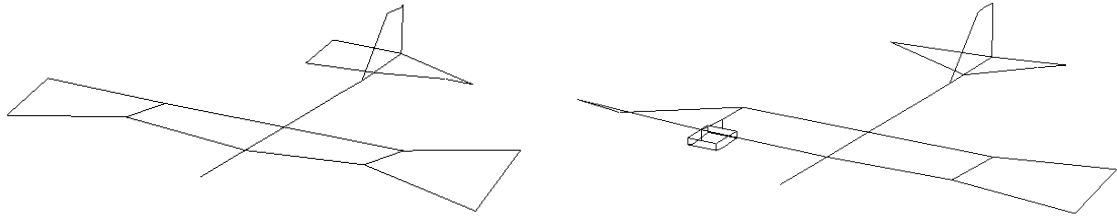


Figure 30. Mode shape corresponding to a frequency of 74.4 Hz without pods (left) and 53.6 Hz with pods (right).

Discussion

The results are summarized in Table 2. It can be seen that the natural frequencies with the pods are approximately 10%-30% smaller than the corresponding natural frequencies without pods.

Table 2. Summarized natural frequencies (Hz) and damping ratios (%) for the base model with and without pods and percent difference between natural frequencies.

No Pods		Pods		Diff	Description
Freq	Damp	Freq	Damp		
12.4	1.4	11.0	1.2	11.3	Mode 1 wing bending
17.3	2.0	15.6	1.4	9.8	Tail torsion, antisymmetric wingtip bend
20.8	2.0	18.9	2.3	9.1	Wingtip, wing, tail, HS, VS torsion, wingtip bend
26.7	1.7	-	-	-	Wing torsion, slight HS bend
28.9	1.4	20.6	2.1	28.7	Symmetric wing torsion
29.5	1.4	23.2	1.5	21.4	Wingtip bend, HS bend/torsion, tail wag
30.2	1.0	24.8	1.9	17.9	Antisymmetric wingtip bend, tail wag
33.8	0.7	-	-	-	HS, VS torsion
39.9	2.0	-	-	-	HS bend/torsion, mode 2 wing bend, VS torsion
45.0	1.8	34.0	1.8	24.4	Mode 2 wing bend, HS bend/torsion, VS torsion
51.4	0.8	38.3	3.9	25.5	Wing torsion, HS bend/torsion
-	-	40.9	2.8	-	Mode 2 wing torsion, HS bend/torsion
63.7	1.2	47.4	2.8	25.6	Wing torsion, HS bend, fuselage bend
72.3	1.2	-	-	-	Mode 2 wing bend/torsion opposite, HS torsion
74.4	1.7	53.6	1.9	28	HS torsion, mode 2 wing torsion

The decrease in the natural frequencies was expected since, when installed, the wing pods account for 20% of the total weight of the aircraft. The addition of the wing pods creates a whole new structure that may not have all of the same modes as the structure with no pods. This behavior is apparent in several tests where modes only appeared in one or the other of the loading configurations (i.e. 26.7 Hz, 33.8 Hz, 39.9 Hz, and 72.3 Hz without pods and 40.9 Hz with pods). Different levels of instrumentation or different excitation locations can change the relative sizes of the FRFs. This can affect the ability to identify certain modes. It is difficult at times to differentiate between actual modes and noise in the channels. For these tests, peaks in the FRFs were determined to be significant and to be actual modes if they appeared in several tests across multiple excitation locations, and if those tests had a well defined mode shape. There is an inherent danger that modes could be missed in the analysis. This was seen in this testing when the mode at 72.3 Hz was not identified in the initial analysis of the data but was discovered later in re-analysis once it was found in other tests.

Tests with Payload

Tests with and without the pods were also performed with a dummy payload weighing 15 pounds placed in the payload bay. A summary of the natural frequencies is presented in Table 3.

Table 3. Summary of natural frequencies for unloaded and loaded configurations.

No Pods			Pods		
Unloaded	Loaded	%Diff	Unloaded	Loaded	%Diff
12.4	12.0	3.2	11.0	11.0	-
17.3	17.5	1.2	15.6	15.3	1.9
20.8	20.9	0.5	18.9	18.8	0.5
26.7	25.2	5.6	-	-	-
28.9	27.4	5.2	20.6	20.7	0.5
29.5	-	-	23.2	23.0	0.9
30.2	30.3	0.3	24.8	24.8	0.0
33.8	32.7	3.3	-	-	-
39.9	39.2	1.8	-	-	-
45.0	45.2	0.4	34.0	33.3	2.1
51.4	51.6	0.4	38.3	37.6	1.8
-	-	-	40.9	40.4	1.2
63.7	62.7	1.6	47.4	46.9	1.1
72.3	-	-	-	-	-
74.4	74.8	0.5	53.6	54.5	1.7

As can be seen, the load in the payload bay, near the center of gravity, didn't have much effect on the values for the natural frequencies. Most of the loaded frequencies were within 3% of the corresponding unloaded frequencies with a maximum difference of 5.6%. This shows that a wing loading has much more of an effect on the structural characteristics of the aircraft than a fuselage loading.

CHAPTER IV

CHANNEL REDUCTION

Introduction

Channel reduction is an important topic in modal analysis. With every extraneous channel there are associated costs. These costs include an extra sensor as well as the time spent installing, indexing, and logging the sensor as well as processing and analyzing the data obtained from said sensor [13]. Because of this, it is important to use as few channels as possible while still keeping enough to identify the modes of the structure [14]. A key point in channel reduction is sensor location selection. A method was developed for sensor location selection and is presented in Chapter V. To examine the effects of channel reduction, several tests were performed with different types and levels of channel reduction. The first type of channel reduction that was tested was the use of a stick model rather than a planar model of the aircraft. The other type of channel reduction was the removal of different sensors. These are identified by WHV (accelerometers on the wings, horizontal stabilizer, and vertical stabilizer), WH (accelerometers on the wings and horizontal stabilizer), and W (accelerometers on the wings only). The results from these tests are presented in subsequent sections.

Stick Model

Test Description

The first method of channel reduction performed was to use a simpler model of the aircraft. This model was just a stick model and it, along with the accelerometer locations for this test, can be seen in Figure 31. All uni-axial measurements were in the Z direction.

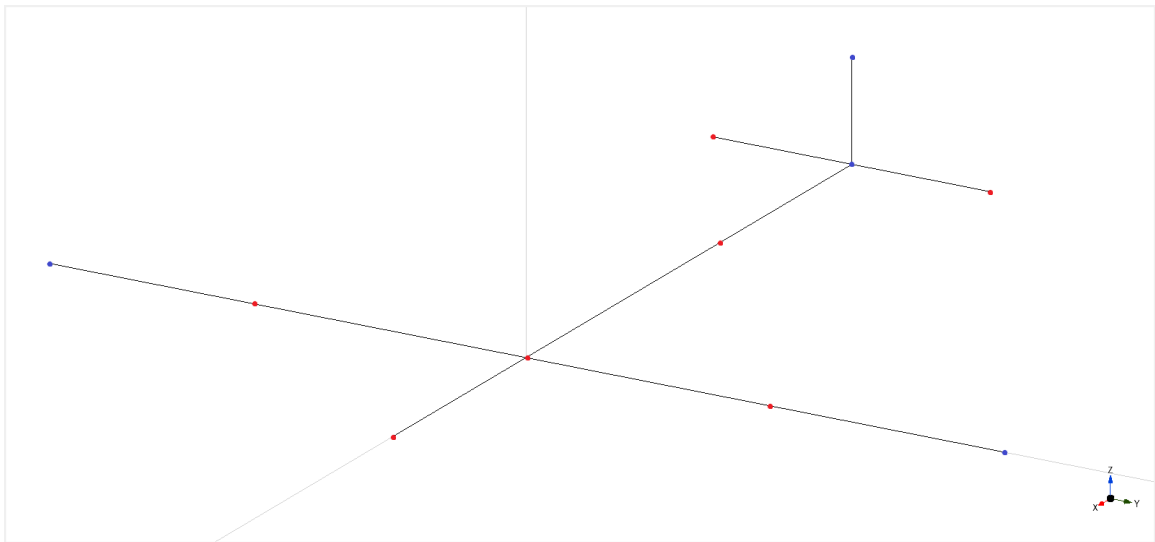


Figure 31. Stick model and accelerometer locations (red = uni-axial, blue = tri-axial).

The data obtained from the base model test, that excited the Super Hauler without pods with a random excitation, was reduced to these channels and the modal analysis was re-run.

Results

The first mode shape that was observed was mode 1 type bending in the wings. This mode corresponded to a natural frequency of 12.4 Hz and the base model's mode at 12.4 Hz. A representation of this mode shape can be seen in Figure 32.

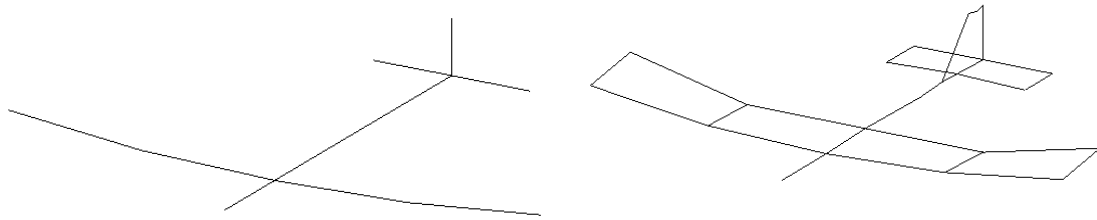


Figure 32. Mode shape corresponding to a frequency of 12.4 Hz for the stick model (left) and 12.4 Hz for the base model (right).

The second mode shape showed tail torsion while the wingtips bent in opposite directions of each other. This mode corresponded to a natural frequency of 17.5 Hz and the base model's mode at 17.3 Hz. A representation of this mode shape can be seen in Figure 33.

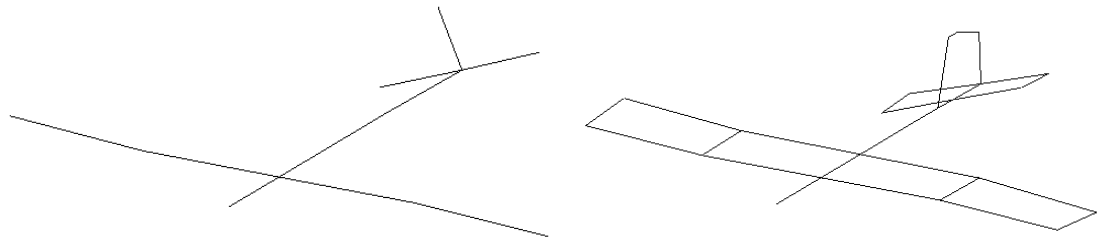


Figure 33. Mode shape corresponding to a frequency of 17.5 Hz for the stick model (left) and 17.3 Hz for the base model (right).

The third mode shape showed wing and tail torsion while the wingtips bent. This mode corresponded to a natural frequency of 20.9 Hz and the base model's mode at 20.8 Hz. A representation of this mode shape can be seen in Figure 34.

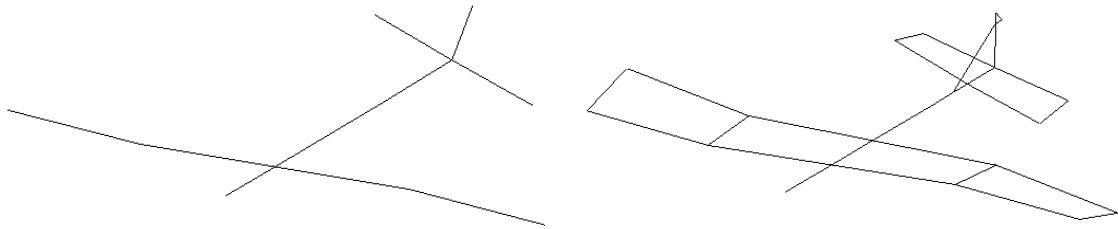


Figure 34. Mode shape corresponding to a frequency of 20.9 Hz for the stick model (left) and 20.8 Hz for the base model (right).

The fourth mode shape showed the wings bending while the horizontal stabilizer bent slightly. This mode corresponded to a natural frequency of 25.7 Hz and the base model's mode at 26.7 Hz. A representation of this mode shape can be seen in Figure 35.

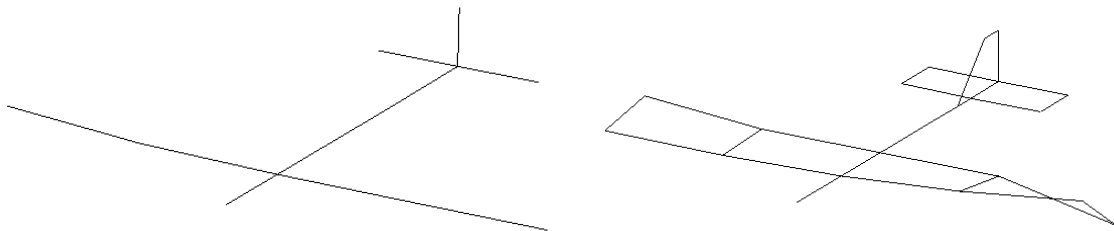


Figure 35. Mode shape corresponding to a frequency of 25.7 Hz for the stick model (left) and 26.7 Hz for the base model (right).

The fifth mode shape showed wing torsion in the same direction. This mode corresponded to a natural frequency of 27.4 Hz and the base model's mode at 28.9 Hz. A representation of this mode shape can be seen in Figure 36.

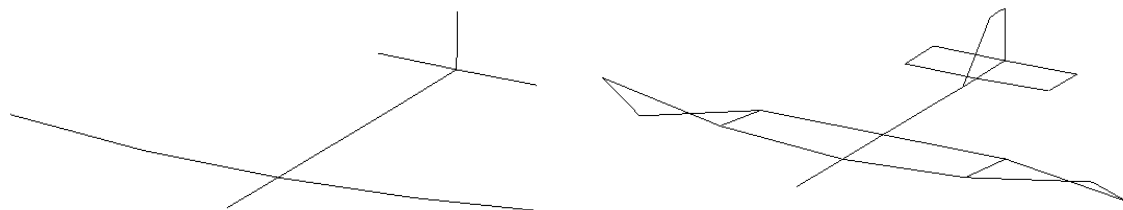


Figure 36. Mode shape corresponding to a frequency of 27.4 Hz for the stick model (left) and 28.9 Hz for the base model (right).

The sixth mode shape showed the wingtips bending in opposite directions of each other. This mode corresponded to a natural frequency of 31.0 Hz and the base model's mode at 30.2 Hz. A representation of this mode shape can be seen in Figure 37.

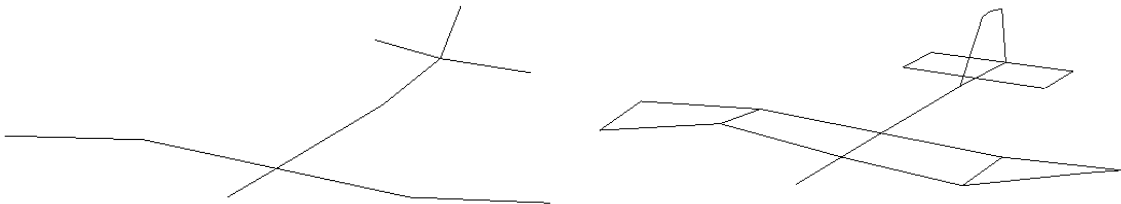


Figure 37. Mode shape corresponding to a frequency of 31.0 Hz for the stick model (left) and 30.2 Hz for the base model (right).

The seventh mode shape showed the horizontal stabilizer bending. This mode corresponded to a natural frequency of 37.9 Hz and the base model's mode at 33.8 Hz. A representation of this mode shape can be seen in Figure 38.

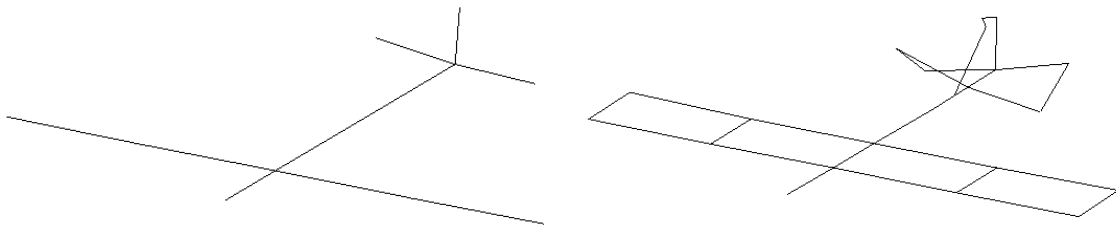


Figure 38. Mode shape corresponding to a frequency of 37.9 Hz for the stick model (left) and 33.8 Hz for the base model (right).

The eighth mode shape showed the horizontal stabilizer bending while the wings experienced mode 2 bending. This mode corresponded to a natural frequency of 39.9 Hz and the base model's mode at 39.9 Hz. A representation of this mode shape can be seen in Figure 39.

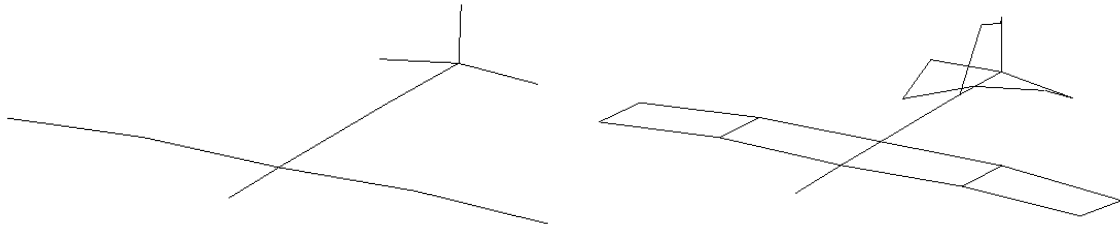


Figure 39. Mode shape corresponding to a frequency of 39.9 Hz for the stick model (left) and 39.9 Hz for the base model (right).

The ninth mode shape showed the wings experiencing mode 2 type bending while the horizontal stabilizer bent. This mode corresponded to a natural frequency of 44.9 Hz and the base model's mode at 45.0 Hz. A representation of this mode shape can be seen in Figure 40.

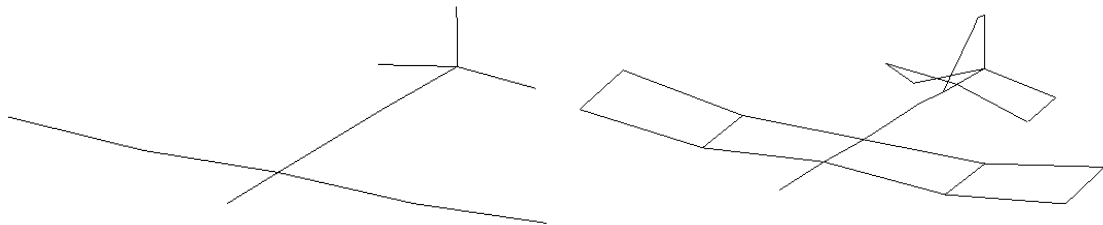


Figure 40. Mode shape corresponding to a frequency of 44.9 Hz for the stick model (left) and 45.0 Hz for the base model (right).

The tenth mode shape showed the wings and the horizontal stabilizer bending. This mode corresponded to a natural frequency of 50.4 Hz and the base model's mode at 51.4 Hz. A representation of this mode shape can be seen in Figure 41.

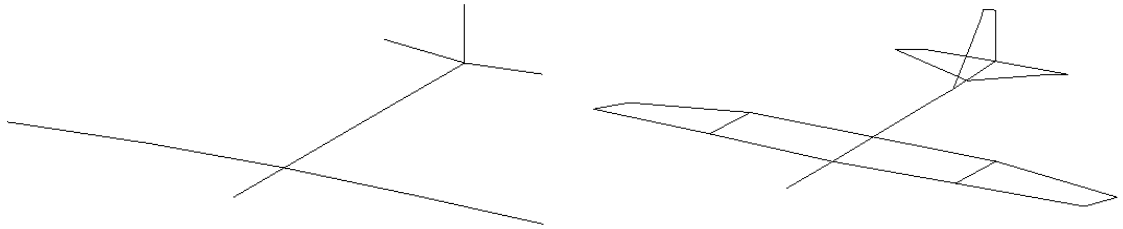


Figure 41. Mode shape corresponding to a frequency of 50.4 Hz for the stick model (left) and 51.4 Hz for the base model (right).

The eleventh mode shape showed wing torsion and the horizontal stabilizer bending. This mode corresponded to a natural frequency of 64.1 Hz and the base model's mode at 63.7 Hz. A representation of this mode shape can be seen in Figure 42.

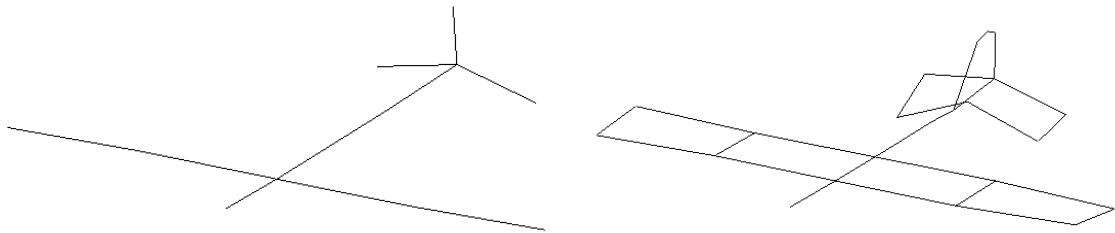


Figure 42. Mode shape corresponding to a frequency of 64.1 Hz for the stick model (left) and 63.7 Hz for the base model (right).

The twelfth mode shape showed the wings in mode 2 wing bending while the horizontal stabilizer bent. This mode corresponded to a natural frequency of 72.8 Hz and the base model's mode at 72.3 Hz. A representation of this mode shape can be seen in Figure 43.

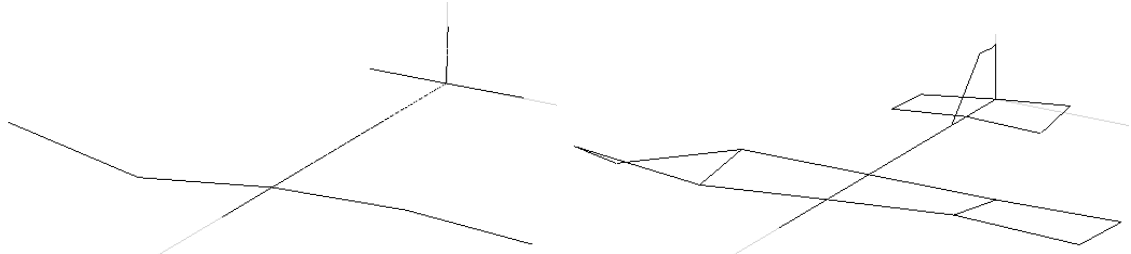


Figure 43. Mode shape corresponding to a frequency of 72.8 Hz for the stick model (left) and 72.3 Hz for the base model (right).

The thirteenth mode shape showed the horizontal stabilizer bending while the wings underwent mode 2 wing bending. This mode corresponded to a natural frequency of 76.2 Hz and the base model's mode at 74.4 Hz. A representation of this mode shape can be seen in Figure 44.

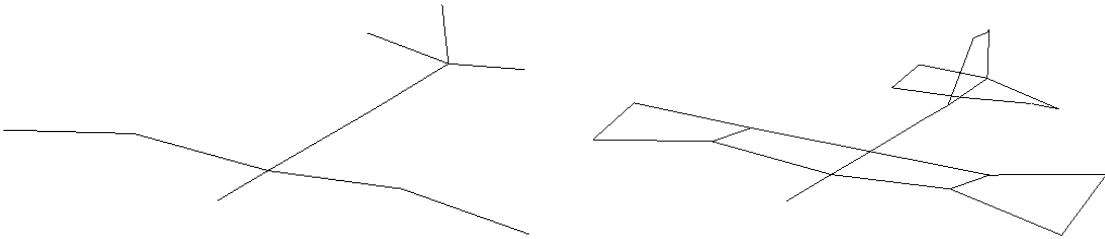


Figure 44. Mode shape corresponding to a frequency of 76.2 Hz for the stick model (left) and 74.4 Hz for the base model (right).

Discussion/Comparison

A summary of the natural frequencies found in the stick model compared to the natural frequencies for the base model with no pods can be seen in Table 4.

Table 4. Stick model natural frequency summary.

Stick Model	Base Model	%Diff	Description
12.4	12.4	0.0	Mode 1 wing bending
17.5	17.3	1.2	Tail torsion, antisymmetric wingtip bend
20.9	20.8	0.5	Wingtip, wing, tail, HS, VS torsion, wingtip bend
25.7	26.7	3.7	Wing torsion, slight HS bend
27.4	28.9	5.2	Symmetric wing torsion
31.0	30.2	2.6	Wingtips bend opposite, tail wag
37.9	33.8	12.1	HS, VS torsion
39.9	39.9	0.0	HS bend/torsion, mode 2 wing bend, VS torsion
44.9	45.0	0.2	Mode 2 wing bend, HS bend/torsion, VS torsion
50.4	51.4	1.9	Wing torsion, HS bend/torsion
64.1	63.7	0.6	Antisymmetric wing torsion, HS bend, fuselage bend
72.8	72.3	0.7	Mode 2 wing bend/torsion opposite, HS torsion
76.2	74.4	2.4	HS torsion, mode 2 wing bend and torsion

The natural frequency values match fairly well with most values differing by less than 2% with a maximum difference of 12%. As would make sense from the data that was removed, any torsional motion was undetectable using the stick model. This is a significant loss of data since the ability to detect torsional motion is a key factor in airworthiness determinations.

Dangers of Channel Reduction

Description

A preliminary test was performed before the base test where the excitation was provided through the use of an impact hammer at the locations and in the directions shown in Figure 45. The tests were performed both with and without the pods and the resulting modes were compared, demonstrating the further reduction of sensor locations.

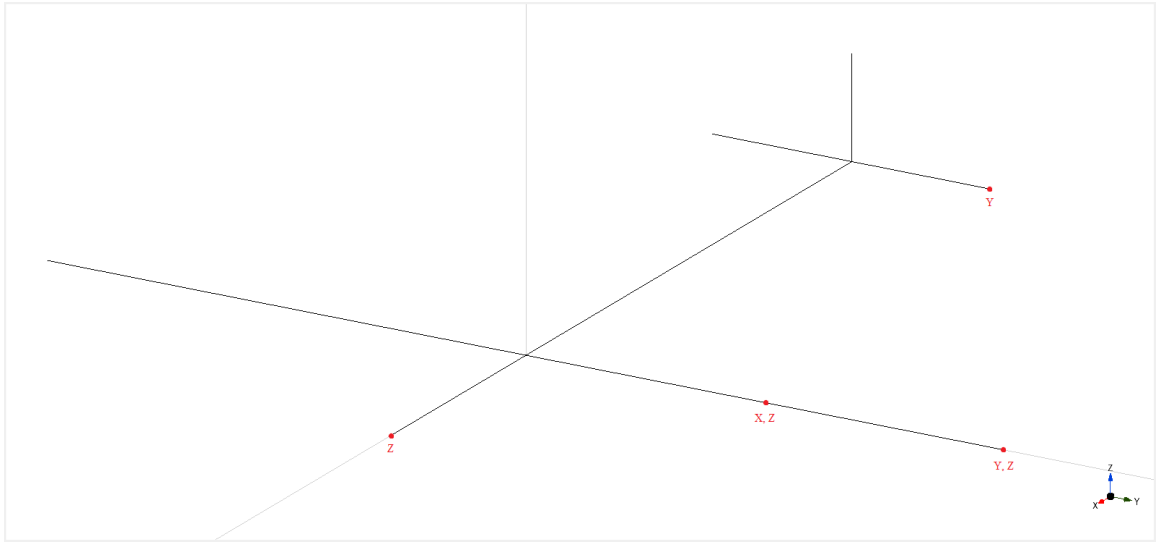


Figure 45. Impact hammer excitation locations and directions.

The impact hammer that was used was a PCB Piezotronics 086C03 impact hammer and can be seen in Figure 46. The impact hammer interfaced with the data acquisition board that was used for the other tests.



Figure 46. PCB Piezotronics 086C03 impact hammer used for excitation.

The sampling rate was left at the default of 1651.61Hz with a resolution of 1Hz. The measurement type was FRF-OMA for an operation excitation modal analysis with number of nodes set to 11. The windowing type was set to rectangle with RMS averaging and exponential weighting with a count of 3. Each of the tests consisted of impacting the Super Hauler at one of the nodes and measuring the frequency response then obtaining the natural frequencies from the frequency response function (FRF) and animating the line model with the corresponding mode shapes.

Results and Discussion

The results from this testing were published in a conference paper as shown in Table 5, and the corresponding mode shapes can be seen in the following figures [3]. However, these results were revisited after the base model test was run and it was discovered that, due to the lack of data in a stick model, several modes were originally misidentified in the preliminary test.

Table 5. Summary of preliminary test natural frequencies.

No Pods	Pods	Description
12	-	Wing-tip bending only
27	11	Tail torsion only
28	13	Wing bending opposite tail bending
73	20	Wing bending and tail torsion
91	28	Mode 2 wing bending

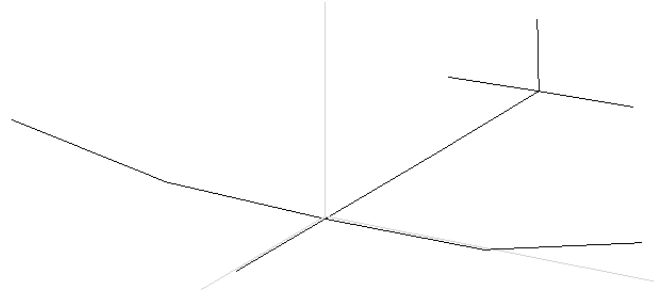


Figure 47. Mode shape corresponding to a frequency of 12 Hz without pods.

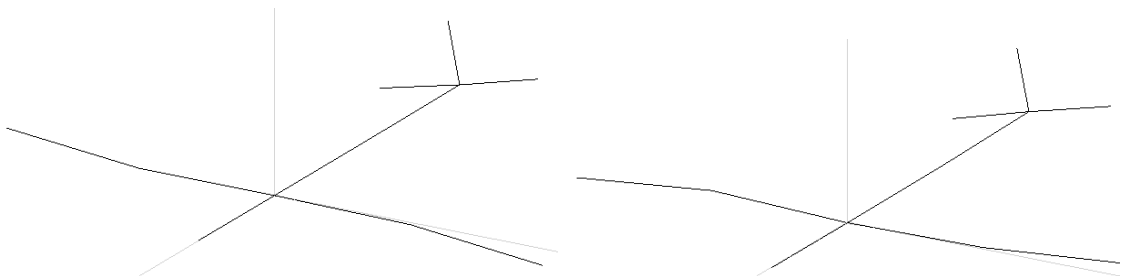


Figure 48. Mode shapes corresponding to a frequency of 27 Hz without pods (left) and 11 Hz with pods (right).

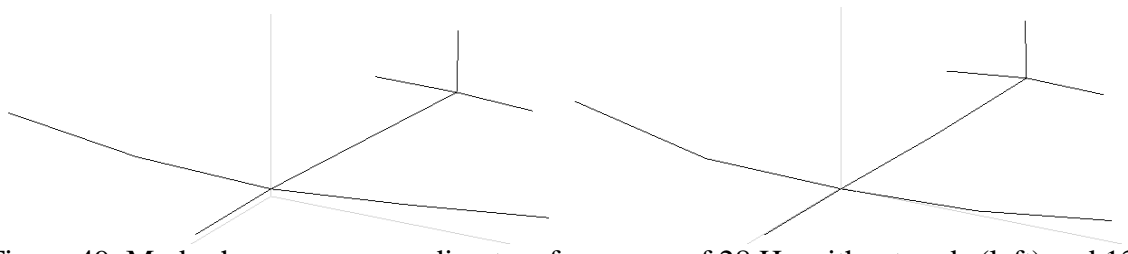


Figure 49. Mode shapes corresponding to a frequency of 28 Hz without pods (left) and 13 Hz with pods (right).

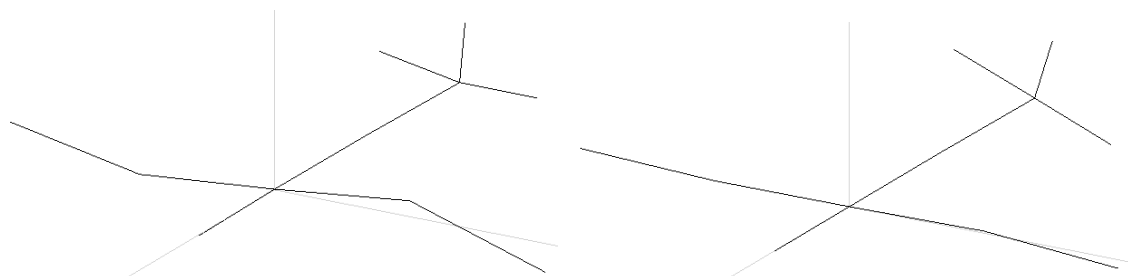


Figure 50. Mode shapes corresponding to a frequency of 73 Hz without pods (left) and 20 Hz with pods (right).

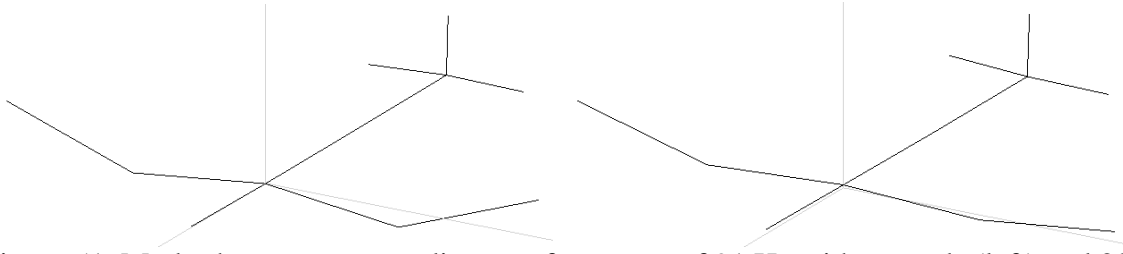


Figure 51. Mode shapes corresponding to a frequency of 91 Hz without pods (left) and 28 Hz with pods (right).

Upon further inspection and comparison to the results from the base model tests and the random excitation stick model tests, the modes were re-identified as shown in

Table 6.

Table 6. Adjusted preliminary test mode identification.

No Pods		Pods		Description
Prelim	Base	Prelim	Base	
12	12.4	-	11.0	Mode 1 wing bending
-	17.3	11	15.6	Tail torsion, antisymmetric wingtip bend
-	-	13	-	Wing, HS bending
27	20.8	20	18.9	Wingtip, wing, tail, HS, VS torsion, wingtip bend
-	26.7	-	-	Wing torsion, slight HS bend
28	28.9	-	20.6	Symmetric wing torsion
-	29.5	-	23.2	Antisymmetric wingtip bend, HS bend/torsion, tail wag
-	30.2	-	24.8	Antisymmetric wingtip bend, tail wag
-	33.8	-	-	HS, VS torsion
-	39.9	-	-	HS bend/torsion, mode 2 wing bend, VS torsion
-	45.0	28	34.0	Mode 2 wing bend, HS bend/torsion, VS torsion
-	51.4	-	38.3	Wing torsion, HS bend/torsion
-	-	-	40.9	Mode 2 wing bend and torsion
-	63.7	-	47.4	Antisymmetric wing torsion, HS bend, fuselage bend
73	72.3	-	-	Mode 2 wing bend/torsion opposite, HS torsion
-	74.4	-	53.6	HS torsion, mode 2 wing bend and torsion

It can be seen that, besides misidentifying modes, several modes were missed as well. It is believed that this is partly due to the analysis being performed on a much larger frequency range (0Hz ~ 300 Hz rather than 0Hz ~ 80 Hz), resulting in much lower resolution and a decreased ability to identify modes with smaller effects.

WHV Model

Test Description

The following channel reductions take a different approach than the stick model. The planar model is kept but data from various accelerometers are removed from the base model. For the WHV test, the data from the accelerometers along the fuselage of the aircraft, as well as the X and Y directional data from the tri-axial accelerometers and the data from uni-axial accelerometer on the vertical stabilizer were removed from the base model data set and the modal analysis was re-run. The remaining accelerometer locations can be seen in Figure 52 where all measurements were uni-axial and in the Z direction, except for the measurement on the vertical stabilizer which was in the Y direction.

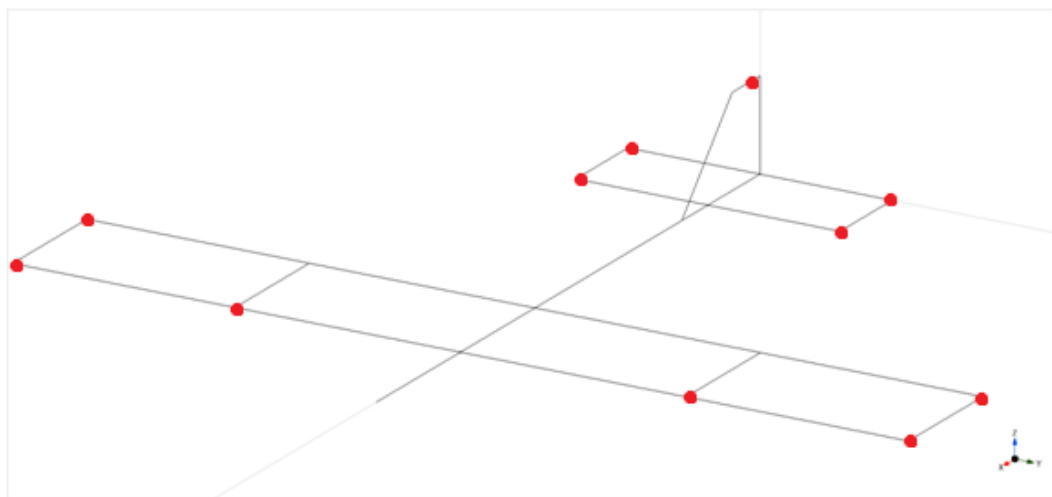


Figure 52. WHV accelerometer locations.

Results

The first mode shape that was observed was mode 1 type bending in the wings. This mode corresponded to a natural frequency of 12.4 Hz and the base model's mode at 12.4 Hz. A representation of this mode shape can be seen in Figure 53.

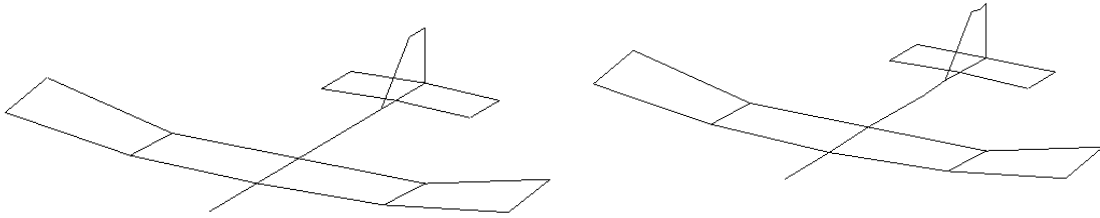


Figure 53. Mode shape corresponding to a frequency of 12.4 Hz for WHV (left) and 12.4 Hz for the base model (right).

The second mode shape showed tail torsion while the wingtips bent in opposite directions of each other. This mode corresponded to a natural frequency of 17.5 Hz and the base model's mode at 17.3 Hz. A representation of this mode shape can be seen in Figure 54.

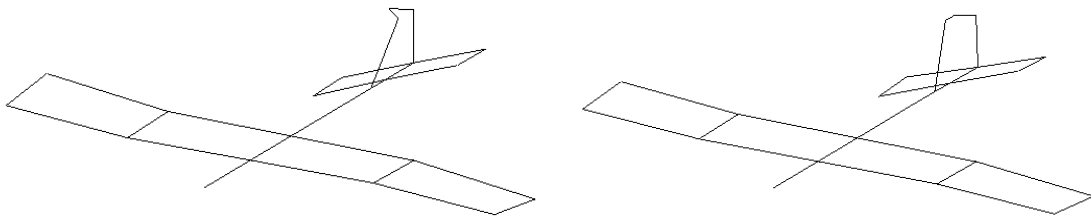


Figure 54. Mode shape corresponding to a frequency of 17.5 Hz for WHV (left) and 17.3 Hz for the base model (right).

The third mode shape showed wingtip, wing, tail, horizontal stabilizer, and vertical stabilizer torsion while the wingtips also bent. This mode corresponded to a natural frequency of 20.8 Hz and the base model's mode at 20.8 Hz. A representation of this mode shape can be seen in Figure 55.

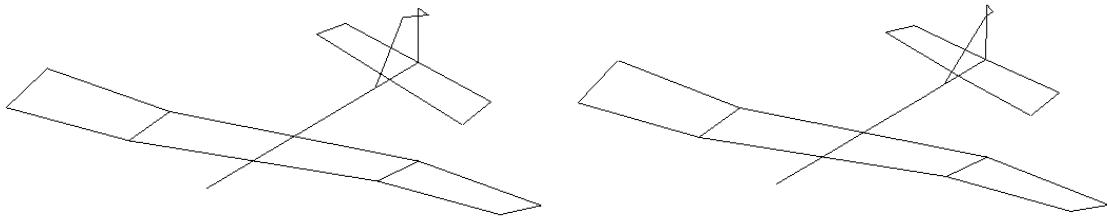


Figure 55. Mode shape corresponding to a frequency of 20.8 Hz for WHV (left) and 20.8 Hz for the base model (right).

The fourth mode shape showed wing torsion while the horizontal stabilizer bent slightly. This mode corresponded to a natural frequency of 26.0 Hz and the base model's mode at 26.7 Hz. A representation of this mode shape can be seen in Figure 56.

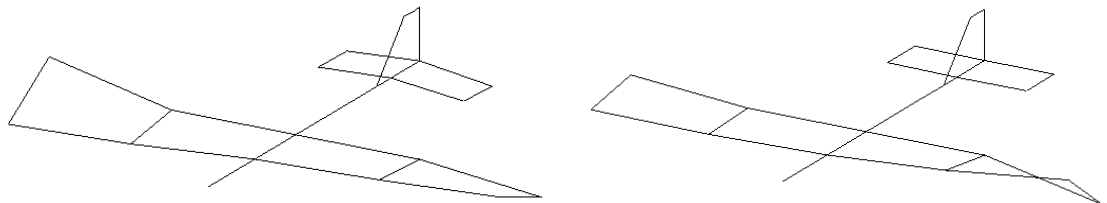


Figure 56. Mode shape corresponding to a frequency of 26.0 Hz for WHV (left) and 26.7 Hz for the base model (right).

The fifth mode shape showed wing torsion in the same direction. This mode corresponded to a natural frequency of 28.2 Hz and the base model's mode at 28.9 Hz. A representation of this mode shape can be seen in Figure 57.

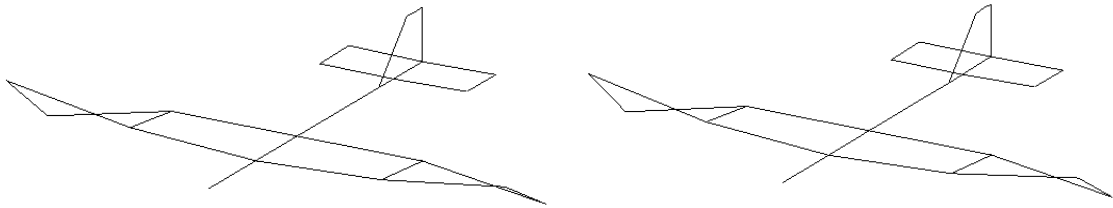


Figure 57. Mode shape corresponding to a frequency of 28.2 Hz for WHV (left) and 28.9 Hz for the base model (right).

The sixth mode shape showed the wingtips bending in opposite directions of each other. This mode corresponded to a natural frequency of 30.8 Hz and the base model's mode at 30.2 Hz. A representation of this mode shape can be seen in Figure 58.

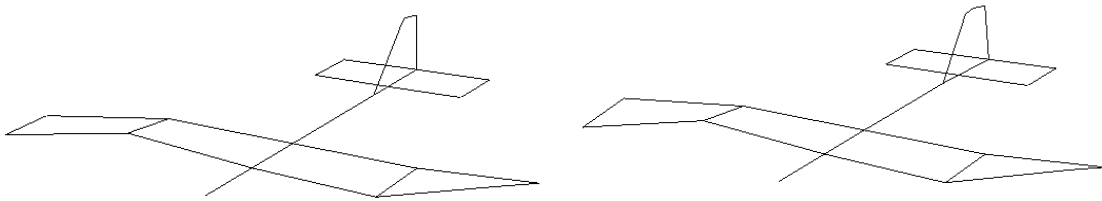


Figure 58. Mode shape corresponding to a frequency of 30.8 Hz for WHV (left) and 30.2 Hz for the base model (right).

The seventh mode shape showed horizontal and vertical stabilizer torsion. This mode corresponded to a natural frequency of 36.5 Hz and the base model's mode at 33.8 Hz. A representation of this mode shape can be seen in Figure 59.

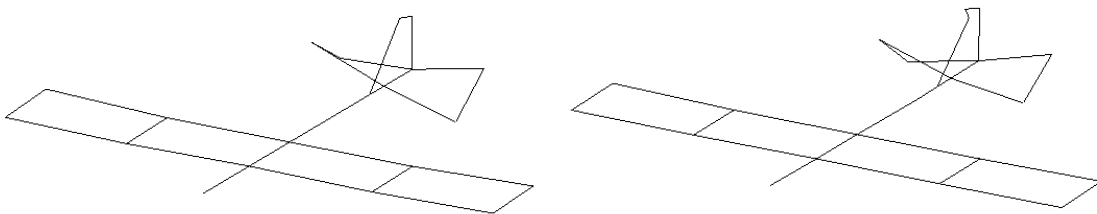


Figure 59. Mode shape corresponding to a frequency of 36.5 Hz for WHV (left) and 33.8 Hz for the base model (right).

The eighth mode shape showed horizontal stabilizer bending and torsion while the wings experienced mode 2 bending and the vertical stabilizer experienced torsion. This mode corresponded to a natural frequency of 39.7 Hz and the base model's mode at 39.9 Hz. A representation of this mode shape can be seen in Figure 60.

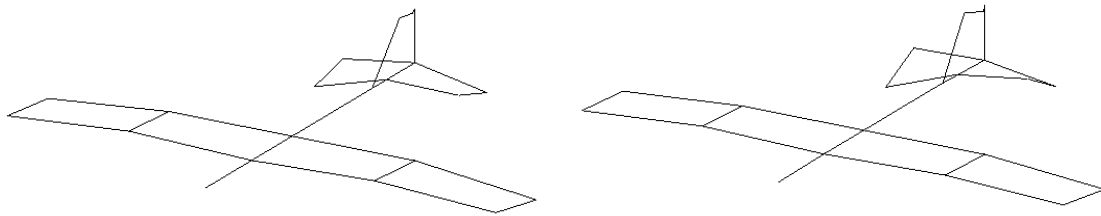


Figure 60. Mode shape corresponding to a frequency of 39.7 Hz for WHV (left) and 39.9 Hz for the base model (right).

The ninth mode shape showed the wings experiencing mode 2 type bending with horizontal stabilizer bending and torsion. This mode corresponded to a natural frequency of 44.9 Hz and the base model's mode at 45.0 Hz. A representation of this mode shape can be seen in Figure 61.

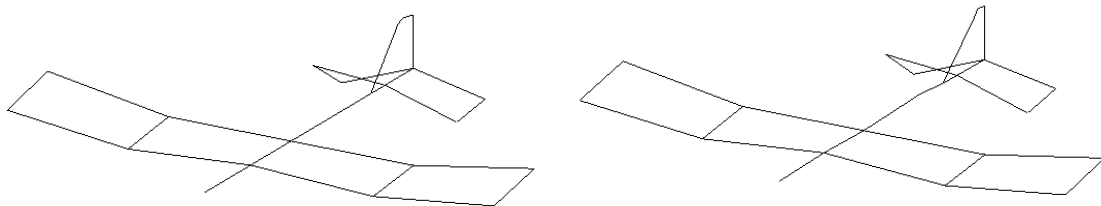


Figure 61. Mode shape corresponding to a frequency of 44.9 Hz for WHV (left) and 45.0 Hz for the base model (right).

The tenth mode shape showed wing and horizontal stabilizer torsion in the same direction. This mode corresponded to a natural frequency of 51.0 Hz and the base model's mode at 51.4 Hz. A representation of this mode shape can be seen in Figure 62.

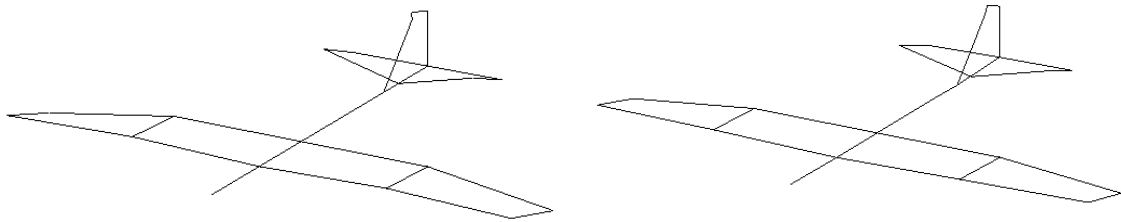


Figure 62. Mode shape corresponding to a frequency of 51.0 Hz for WHV (left) and 51.4 Hz for the base model (right).

The eleventh mode shape showed wing torsion in opposite directions from each other while the horizontal stabilizer bent. This mode corresponded to a natural frequency of 61.1 Hz and the base model's mode at 63.7 Hz. A representation of this mode shape can be seen in Figure 63.

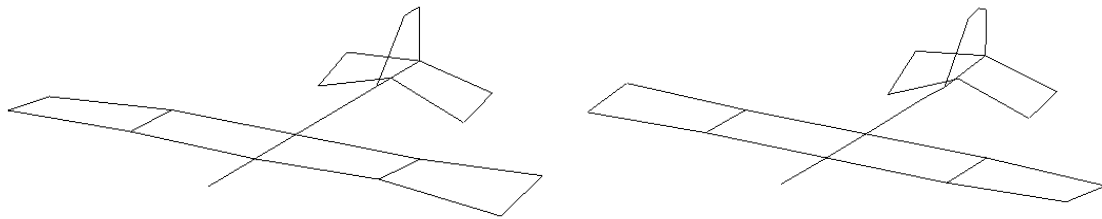


Figure 63. Mode shape corresponding to a frequency of 61.1 Hz for WHV (left) and 63.7 Hz for the base model (right).

The twelfth mode shape showed the wings undergoing mode 2 bending and torsion and the horizontal stabilizer in torsion. This mode corresponded to a natural frequency of 73.3 Hz and the base model's mode at 72.3 Hz. A representation of this mode shape can be seen in Figure 64.

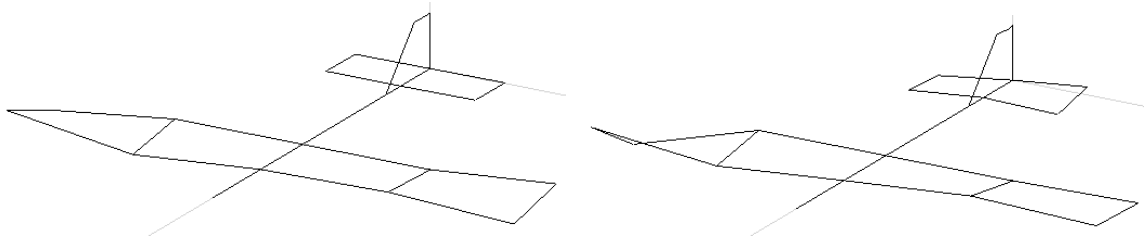


Figure 64. Mode shape corresponding to a frequency of 73.3 Hz for WHV (left) and 72.3 Hz for the base model (right).

The thirteenth mode shape showed horizontal stabilizer torsion while the wings underwent mode 2 wing bending and torsion. This mode corresponded to a natural frequency of 75.9 Hz and the base model's mode at 74.4 Hz. A representation of this mode shape can be seen in Figure 65.

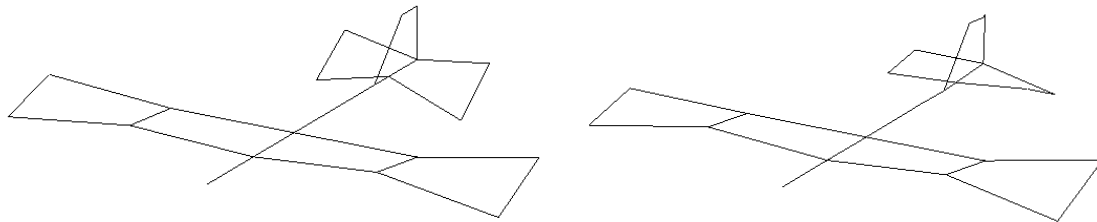


Figure 65. Mode shape corresponding to a frequency of 75.9 Hz for WHV (left) and 74.4 Hz for the base model (right).

Discussion/Comparison

A summary of the natural frequencies found in the WHV test, compared to the natural frequencies for the base model with no pods, can be seen in Table 7. The natural frequency values match fairly well with most values differing less than 2% with a maximum difference of 8%.

Table 7. WHV natural frequency summary.

WHV	Base Model	%Diff	Description
12.4	12.4	0.0	Mode 1 wing bending
17.5	17.3	1.2	Tail torsion, antisymmetric wingtip bend
20.8	20.8	0.0	Wingtip, wing, tail, HS, VS torsion, wingtip bend
26.0	26.7	2.6	Wing torsion, slight HS bend
28.2	28.9	2.4	Symmetric wing torsion
30.8	30.2	2.0	Antisymmetric wingtip bend, tail wag
36.5	33.8	8.0	HS, VS torsion
39.7	39.9	0.5	HS bend/torsion, mode 2 wing bend, VS torsion
44.9	45.0	0.2	Mode 2 wing bend, HS bend/torsion, VS torsion
51.0	51.4	0.8	Wing torsion, HS bend/torsion
61.1	63.7	4.1	Antisymmetric wing torsion, HS bend, fuselage bend
73.3	72.3	1.4	Mode 2 wing bend/torsion opposite, HS torsion
75.9	74.4	2.0	HS torsion, mode 2 wing bend and torsion

It can be seen that the WHV test captured all of the natural frequencies that were observed in the base model. However, as would make sense from the data that was removed, any motion in the fuselage was undetectable using the WHV data. Since there was relatively little activity in the fuselage when compared to the rest of the structure, the inability to observe that motion is fairly insignificant. The motion in the fuselage is also not important in flutter analysis so it doesn't factor into airworthiness determinations.

WH Model

Test Description

The data was further parsed to remove the data from the remaining accelerometer on the vertical stabilizer and the modal analysis was re-run. The remaining accelerometer locations can be seen in Figure 66 where all measurements were uni-axial and in the Z direction.

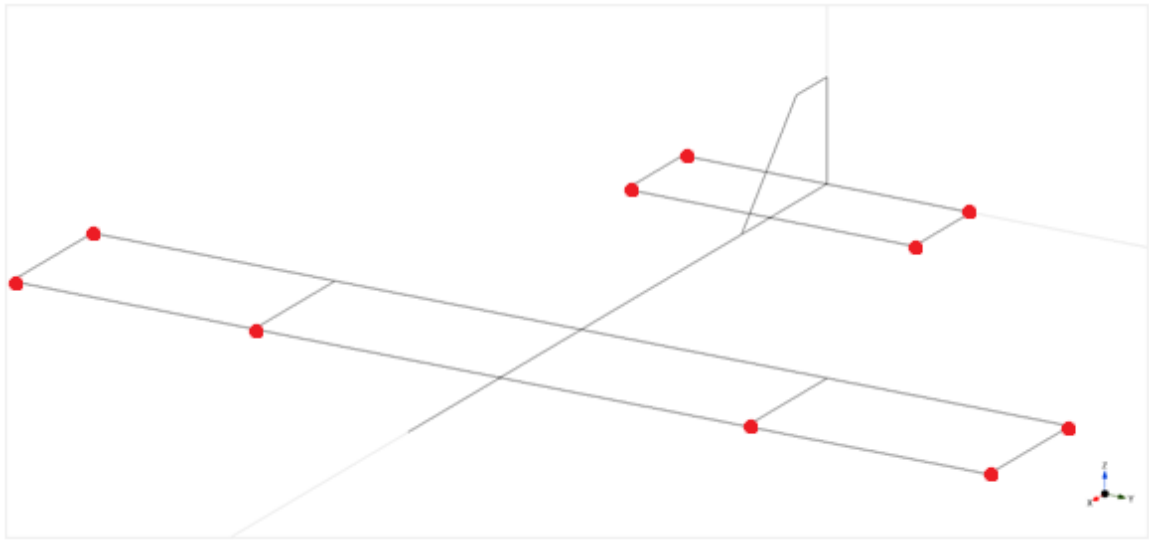


Figure 66. WH accelerometer locations.

Results

The first mode shape that was observed was mode 1 type bending in the wings. This mode corresponded to a natural frequency of 12.4 Hz and the base model's mode at 12.4 Hz. A representation of this mode shape can be seen in Figure 67.

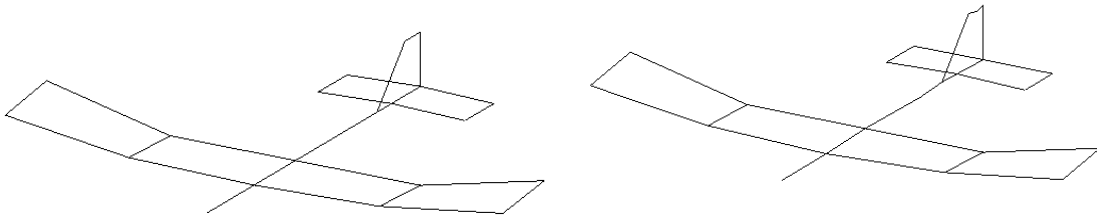


Figure 67. Mode shape corresponding to a frequency of 12.4 Hz for WH (left) and 12.4 Hz for the base model (right).

The second mode shape showed tail torsion while the wingtips bent in opposite directions of each other. This mode corresponded to a natural frequency of 17.5 Hz and the base model's mode at 17.3 Hz. A representation of this mode shape can be seen in Figure 68.

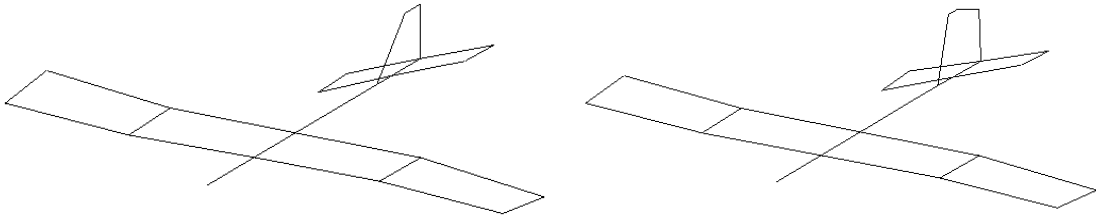


Figure 68. Mode shape corresponding to a frequency of 17.5 Hz for WH (left) and 17.3 Hz for the base model (right).

The third mode shape showed wingtip, wing, tail, and horizontal stabilizer torsion while the wingtips also bent. This mode corresponded to a natural frequency of 20.8 Hz and the base model's mode at 20.8 Hz. A representation of this mode shape can be seen in Figure 69.

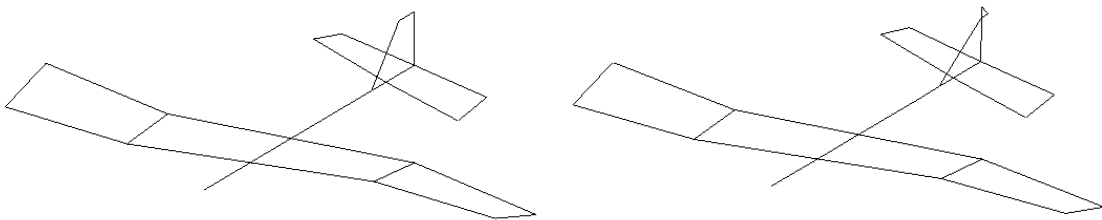


Figure 69. Mode shape corresponding to a frequency of 20.8 Hz for WH (left) and 20.8 Hz for the base model (right).

The fourth mode shape showed wing torsion while the horizontal stabilizer bent slightly. This mode corresponded to a natural frequency of 26.0 Hz and the base model's mode at 26.7 Hz. A representation of this mode shape can be seen in Figure 70.

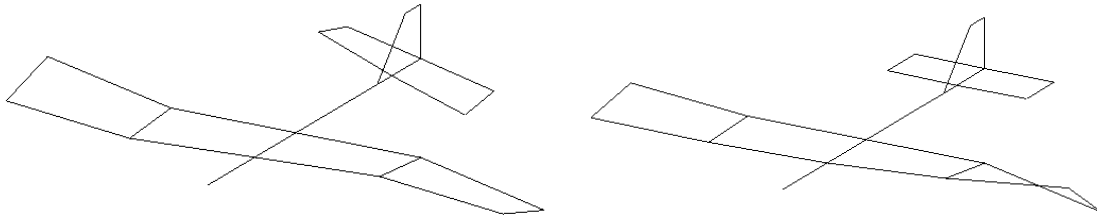


Figure 70. Mode shape corresponding to a frequency of 26.0 Hz for WH (left) and 26.7 Hz for the base model (right).

The fifth mode shape showed wing torsion in the same direction. This mode corresponded to a natural frequency of 28.1 Hz and the base model's mode at 28.9 Hz. A representation of this mode shape can be seen in Figure 71.



Figure 71. Mode shape corresponding to a frequency of 28.1 Hz for WH (left) and 28.9 Hz for the base model (right).

The sixth mode shape showed the wingtips bending in opposite directions of each other. This mode corresponded to a natural frequency of 30.8 Hz and the base model's mode at 30.2 Hz. A representation of this mode shape can be seen in Figure 72.

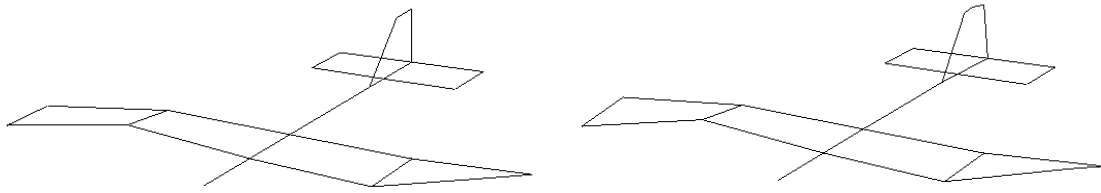


Figure 72. Mode shape corresponding to a frequency of 30.8 Hz for WH (left) and 30.2 Hz for the base model (right).

The seventh mode shape showed horizontal stabilizer torsion. This mode corresponded to a natural frequency of 36.1 Hz and the base model's mode at 33.8 Hz. A representation of this mode shape can be seen in Figure 73.

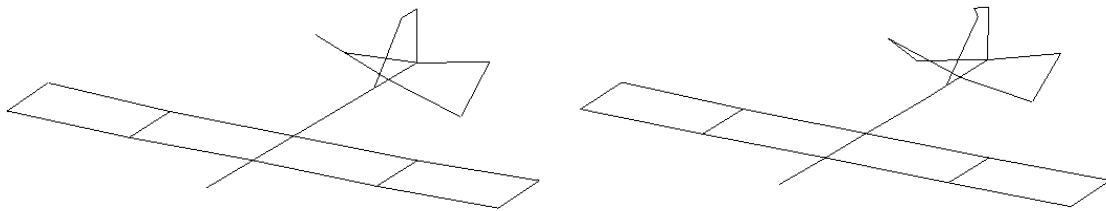


Figure 73. Mode shape corresponding to a frequency of 36.1 Hz for WH (left) and 33.8 Hz for the base model (right).

The eighth mode shape showed horizontal stabilizer bending and torsion while the wings experienced mode 2 bending. This mode corresponded to a natural frequency of 39.8 Hz and the base model's mode at 39.9 Hz. A representation of this mode shape can be seen in Figure 74.

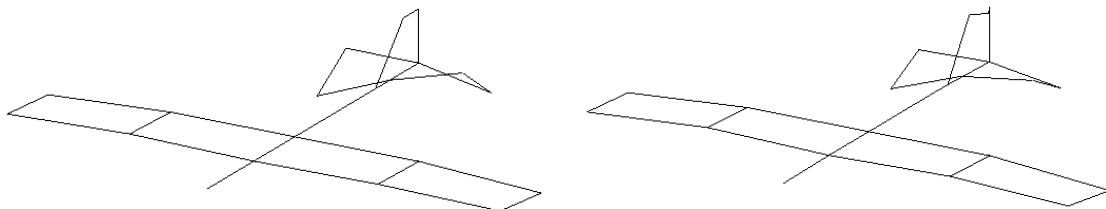


Figure 74. Mode shape corresponding to a frequency of 39.8 Hz for WH (left) and 39.9 Hz for the base model (right).

The ninth mode shape showed the wings experiencing mode 2 type bending while the horizontal stabilizer experienced bending and torsion. This mode corresponded to a natural frequency of 44.9 Hz and the base model's mode at 45.0 Hz. A representation of this mode shape can be seen in Figure 75.

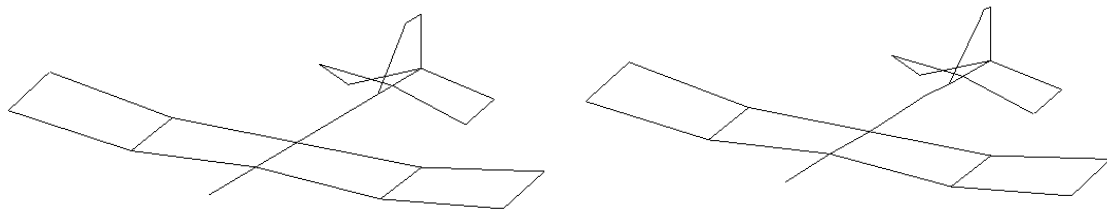


Figure 75. Mode shape corresponding to a frequency of 44.9 Hz for WH (left) and 45.0 Hz for the base model (right).

The tenth mode shape showed wing and the horizontal stabilizer torsion in the same direction. This mode corresponded to a natural frequency of 51.7 Hz and the base model's mode at 51.4 Hz. A representation of this mode shape can be seen in Figure 76.

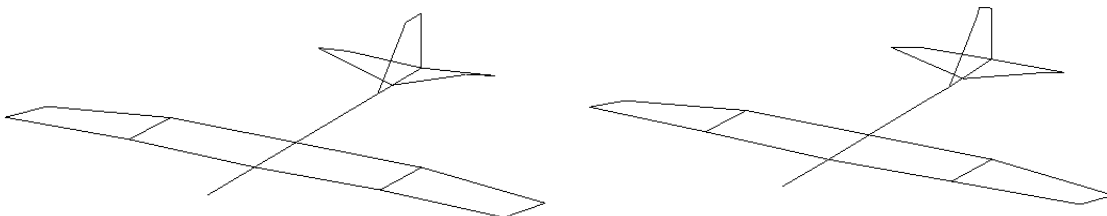


Figure 76. Mode shape corresponding to a frequency of 51.7 Hz for WH (left) and 51.4 Hz for the base model (right).

The eleventh mode shape showed wing torsion in opposite directions from each other while the horizontal stabilizer bent. This mode corresponded to a natural frequency of 62.9 Hz and the base model's mode at 63.7 Hz. A representation of this mode shape can be seen in Figure 77.

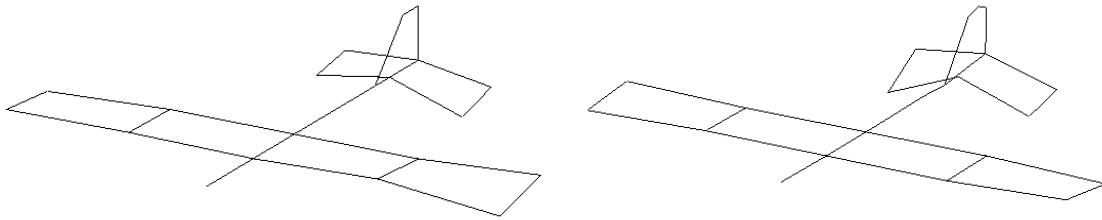


Figure 77. Mode shape corresponding to a frequency of 62.9 Hz for WH (left) and 63.7 Hz for the base model (right).

The twelfth mode shape showed the wings undergoing mode 2 bending and torsion and the horizontal stabilizer in torsion. This mode corresponded to a natural frequency of 72.0 Hz and the base model's mode at 72.3 Hz. A representation of this mode shape can be seen in Figure 78.

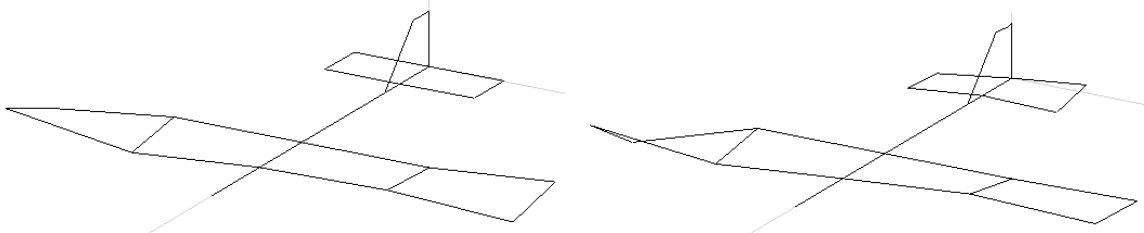


Figure 78. Mode shape corresponding to a frequency of 72.0 Hz for WH (left) and 72.3 Hz for the base model (right).

The thirteenth mode shape showed horizontal stabilizer torsion while the wings underwent mode 2 wing bending and torsion. This mode corresponded to a natural frequency of 75.9 Hz and the base model's mode at 74.4 Hz. A representation of this mode shape can be seen in Figure 79.

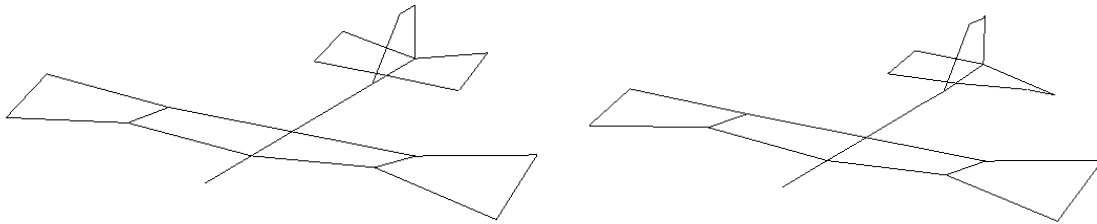


Figure 79. Mode shape corresponding to a frequency of 75.9 Hz for WH (left) and 74.4 Hz for the base model (right).

Discussion/Comparison

A summary of the natural frequencies found from the WH test, as well as the natural frequencies for the base model with no pods, can be seen in Table 8. The natural frequency values between these models match fairly well with most values differing less than 2% with a maximum difference of 7%.

Table 8. WH natural frequency summary

WH	Base Model	%Diff	Description
12.4	12.4	0.0	Mode 1 wing bending
17.5	17.3	1.2	Tail torsion, antisymmetric wingtip bend
20.8	20.8	0.0	Wingtip, wing, tail, HS, VS torsion, wingtip bend
26.0	26.7	2.6	Wing torsion, slight HS bend
28.1	28.9	2.8	Symmetric wing torsion
30.8	30.2	2.0	Antisymmetric wingtip bend, tail wag
36.1	33.8	6.8	HS, VS torsion
39.8	39.9	0.3	HS bend/torsion, mode 2 wing bend, VS torsion
44.9	45.0	0.2	Mode 2 wing bend, HS bend/torsion, VS torsion
51.7	51.4	0.6	Wing torsion, HS bend/torsion
62.9	63.7	1.3	Antisymmetric wing torsion, HS bend, fuselage bend
72.0	72.3	0.4	Mode 2 wing bend/torsion opposite, HS torsion
75.9	74.4	2.0	HS torsion same, mode 2 wing bend and torsion same

The WH test captured all of the natural frequencies that were seen in the base model. However, any motion in the fuselage or vertical stabilizer was undetectable using the WH data. The inability to observe this motion could be acceptable since the fuselage and vertical stabilizer don't experience much motion and all of the modes were detected. However, if flutter is a concern in the vertical stabilizer, this level of channel reduction would not be acceptable since the motion in the vertical stabilizer would have to be known to make an airworthiness determination. Therefore, depending on the application, this loss of ability to observe vertical stabilizer motion could be significant.

W Model

Test Description

The data was further parsed to remove all the accelerometers except for those on the wings and the modal analysis was re-run. The accelerometer locations can be seen in Figure 80 where all measurements were uni-axial and in the Z direction.

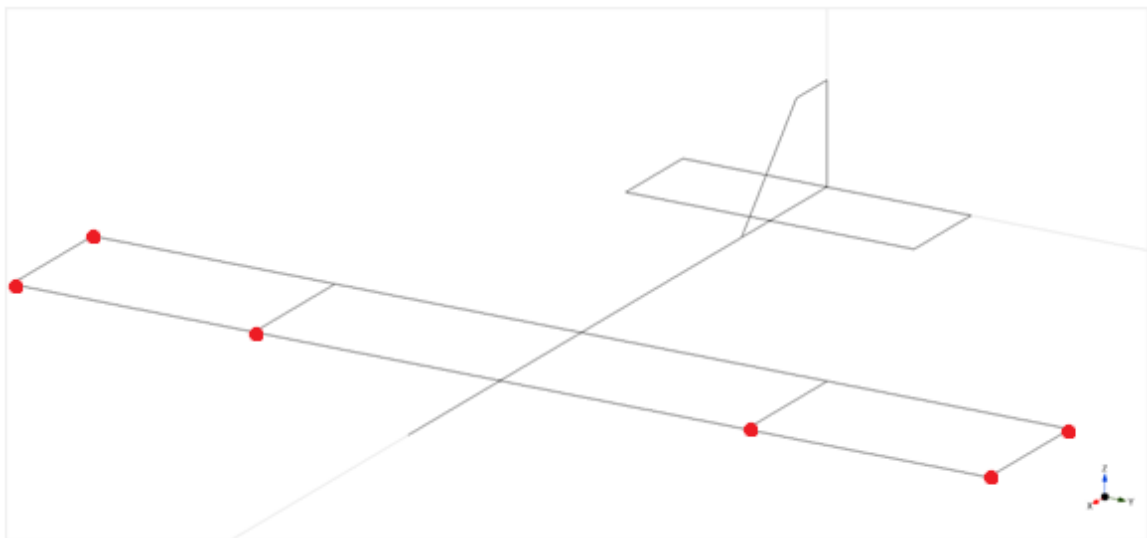


Figure 80. W accelerometer locations.

Results

The first mode shape that was observed was mode 1 type bending in the wings. This mode corresponded to a natural frequency of 12.4 Hz and the base model's mode at 12.4 Hz. A representation of this mode shape can be seen in Figure 81.

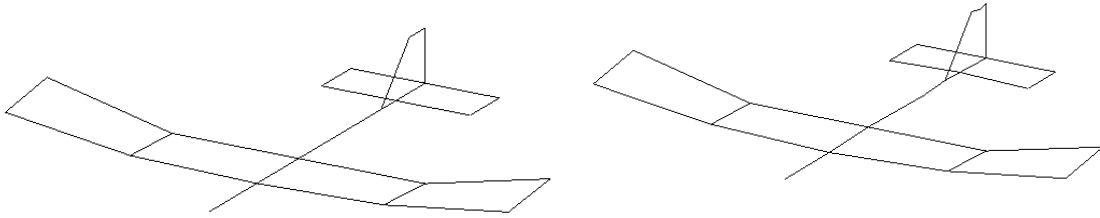


Figure 81. Mode shape corresponding to a frequency of 12.4 Hz for W (left) and 12.4 Hz for the base model (right).

The second mode shape showed tail torsion while the wingtips bent in opposite directions of each other. This mode corresponded to a natural frequency of 17.5 Hz and the base model's mode at 17.3 Hz. A representation of this mode shape can be seen in Figure 82.

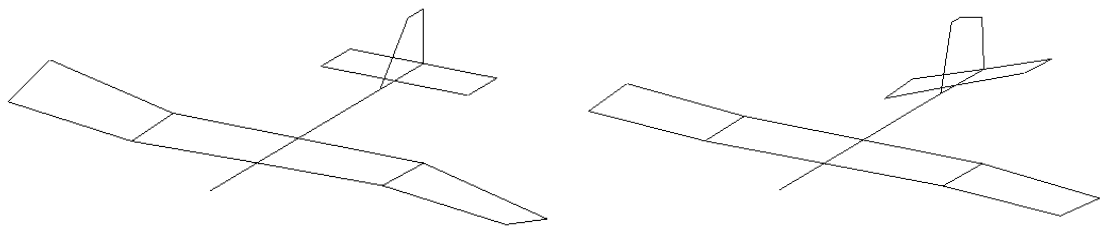


Figure 82. Mode shape corresponding to a frequency of 17.5 Hz for W (left) and 17.3 Hz for the base model (right).

The third mode shape showed wingtip and wing torsion while the wingtips also bent. This mode corresponded to a natural frequency of 21.0 Hz and the base model's mode at 20.8 Hz. A representation of this mode shape can be seen in Figure 83.

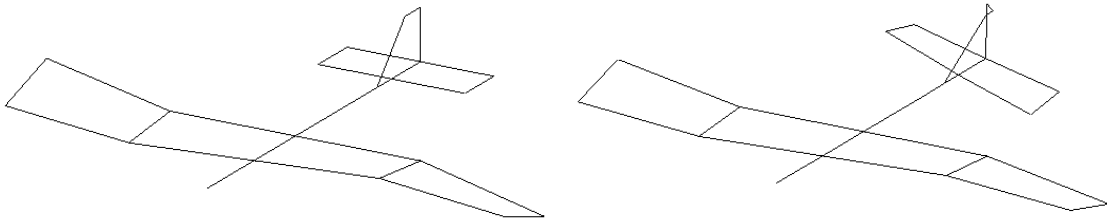


Figure 83. Mode shape corresponding to a frequency of 21.0 Hz for W (left) and 20.8 Hz for the base model (right).

The fourth mode shape showed wing torsion. This mode corresponded to a natural frequency of 25.9 Hz and the base model's mode at 26.7 Hz. A representation of this mode shape can be seen in Figure 84.

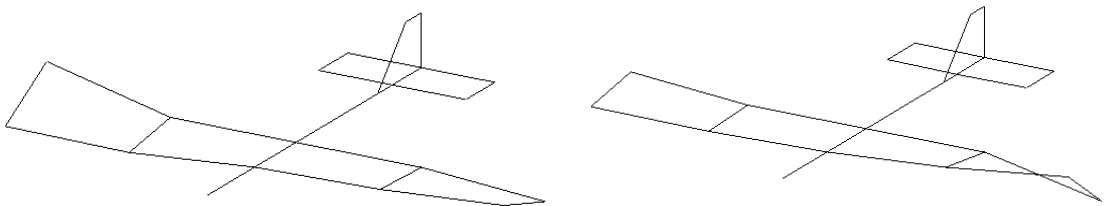


Figure 84. Mode shape corresponding to a frequency of 25.9 Hz for W (left) and 26.7 Hz for the base model (right).

The fifth mode shape showed wing torsion in the same direction. This mode corresponded to a natural frequency of 28.1 Hz and the base model's mode at 28.9 Hz. A representation of this mode shape can be seen in Figure 85.

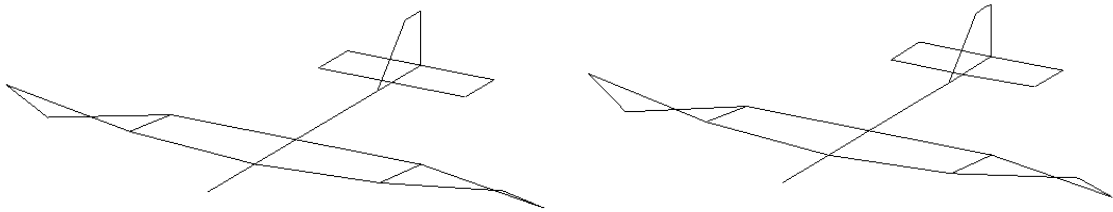


Figure 85. Mode shape corresponding to a frequency of 28.1 Hz for W (left) and 28.9 Hz for the base model (right).

The sixth mode shape showed the wingtips bending in opposite directions of each other. This mode corresponded to a natural frequency of 30.7 Hz and the base model's mode at 30.2 Hz. A representation of this mode shape can be seen in Figure 86.

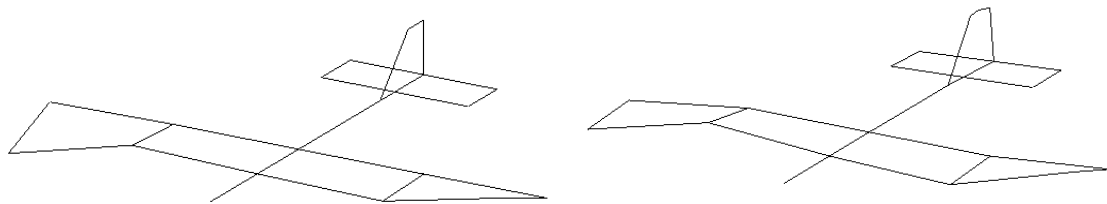


Figure 86. Mode shape corresponding to a frequency of 30.7 Hz for W (left) and 30.2 Hz for the base model (right).

The seventh mode shape showed the wings experiencing mode 2 bending. This mode corresponded to a natural frequency of 39.8 Hz and the base model's mode at 39.9 Hz. A representation of this mode shape can be seen in Figure 87.

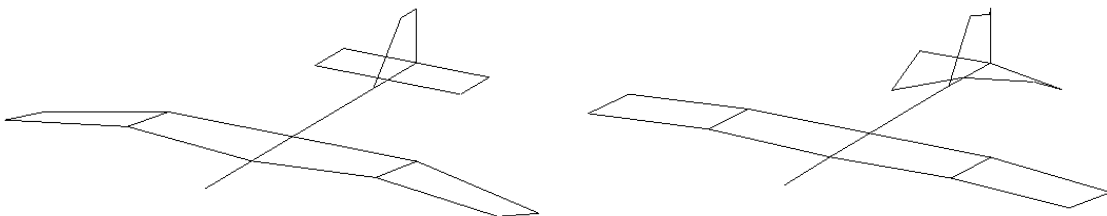


Figure 87. Mode shape corresponding to a frequency of 39.8 Hz for W (left) and 39.9 Hz for the base model (right).

The eighth mode shape showed the wings experiencing mode 2 type bending. This mode corresponded to a natural frequency of 44.7 Hz and the base model's mode at 45.0 Hz. A representation of this mode shape can be seen in Figure 88.

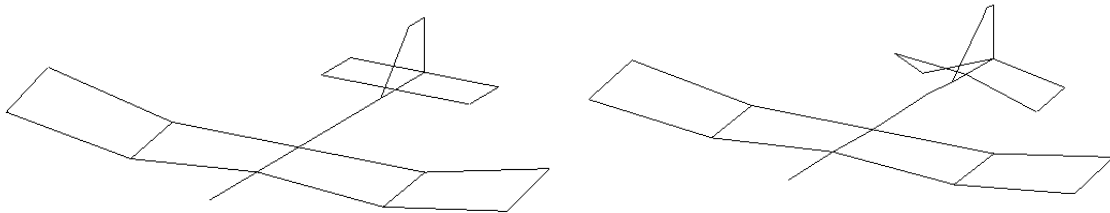


Figure 88. Mode shape corresponding to a frequency of 44.7 Hz for W (left) and 45.0 Hz for the base model (right).

The ninth mode shape showed wing torsion in the same direction. This mode corresponded to a natural frequency of 50.6 Hz and the base model's mode at 51.4 Hz. A representation of this mode shape can be seen in Figure 89.

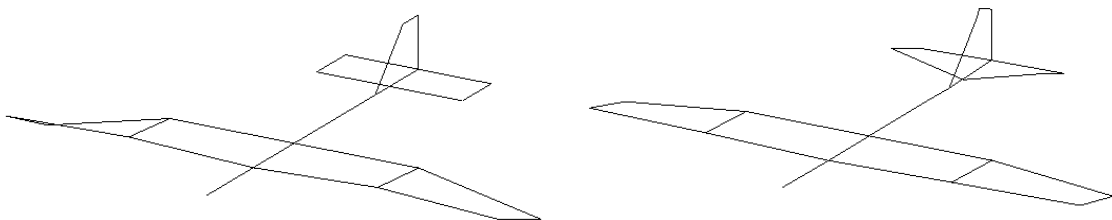


Figure 89. Mode shape corresponding to a frequency of 50.6 Hz for W (left) and 51.4 Hz for the base model (right).

The tenth mode shape showed wing torsion in opposite directions from each other. This mode corresponded to a natural frequency of 64.1 Hz and the base model's mode at 63.7 Hz. A representation of this mode shape can be seen in Figure 90.

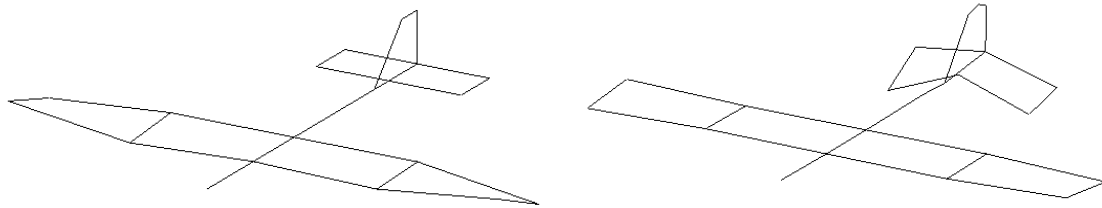


Figure 90. Mode shape corresponding to a frequency of 64.1 Hz for W (left) and 63.7 Hz for the base model (right).

The eleventh mode shape showed the wings undergoing mode 2 bending and torsion. This mode corresponded to a natural frequency of 71.9 Hz and the base model's mode at 72.3 Hz. A representation of this mode shape can be seen in Figure 91.

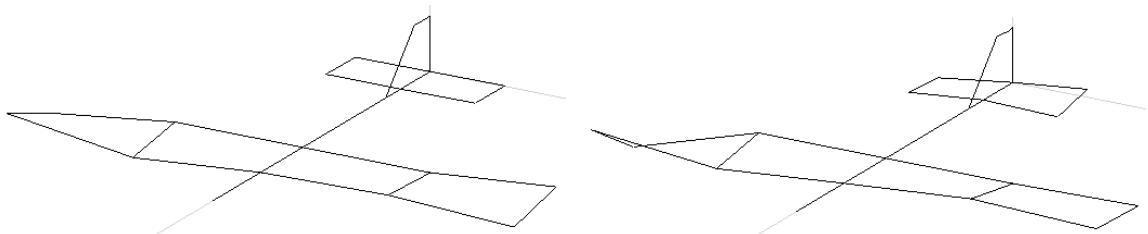


Figure 91. Mode shape corresponding to a frequency of 71.9 Hz for W (left) and 72.3 Hz for the base model (right).

The twelfth mode shape showed the wings in mode 2 wing bending and torsion. This mode corresponded to a natural frequency of 75.8 Hz and the base model's mode at 74.4 Hz. A representation of this mode shape can be seen in Figure 92.

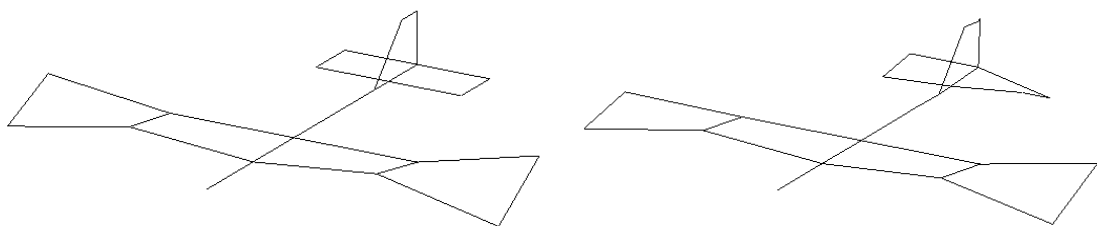


Figure 92. Mode shape corresponding to a frequency of 75.8 Hz for W (left) and 74.4 Hz for the base model (right).

Discussion/Comparison

A summary of the natural frequencies found in W, as well as the natural frequencies for the base model with no pods, can be seen in Table 9. The natural frequency values between these models match fairly well with most values differing less than 2% with a maximum difference of 3%.

Table 9. W natural frequency summary.

W	Base Model	%Diff	Description
12.4	12.4	0.0	Mode 1 wing bending
17.5	17.3	1.2	Tail torsion, antisymmetric wingtip bend
21.0	20.8	1.0	Wingtip, wing, tail, HS, VS torsion, wingtip bend
25.9	26.7	3.0	Wing torsion, slight HS bend
28.1	28.9	2.8	Symmetric wing torsion
30.7	30.2	1.7	Antisymmetric wingtip bend, tail wag
-	33.8	-	HS, VS torsion
39.8	39.9	0.3	HS bend/torsion, mode 2 wing bend, VS torsion
44.7	45.0	0.7	Mode 2 wing bend, HS bend/torsion, VS torsion
50.6	51.4	1.6	Wing torsion, HS bend/torsion
64.1	63.7	0.6	Antisymmetric wing torsion, HS bend, fuselage bend
71.9	72.3	0.6	Mode 2 wing bend/torsion opposite, HS torsion
75.8	74.4	1.9	HS torsion, mode 2 wing bend and torsion

The W test captured almost all of the natural frequencies that were seen in the base model, missing one mode at 33.8 Hz. However, any motion in the fuselage or tail was undetectable in this test. The inability to detect a mode at 33.8 Hz can be traced to this fact since that mode consists of horizontal and vertical stabilizer motion. This factors into airworthiness determinations because of the inability to see motion in the horizontal stabilizer. This lack of important information leads to the conclusion that this is too much channel reduction and that the important surfaces of the aircraft should be instrumented.

CHAPTER V

SENSOR LOCATION IDENTIFICATION METHOD

Introduction

As stated previously, channel reduction is an important topic in modal testing and proper sensor location identification is key to using as few channels as possible. Several methods for identifying important locations for sensors have been developed.

One methodology uses a finite element model in which sensor sets are found which maximize the ability to observe modes while constraining each sensor to contribute unique information [15]. Another method selects sensor locations that make the corresponding target mode shape partitions as linearly independent as possible while maximizing the signal strength of the target modal responses within the sensor data [16]. Yet another method uses a genetic algorithm to identify sensor locations by starting with a relatively small number of possible final locations and evolving these locations to the best set [17]. There is also a method that locates sensors at the maximum response position of an orthogonal sequence of vectors [18].

There are several more methods for sensor location identification but the majority of them require extensive finite element modeling, algorithm development, or mathematical modeling or a combination thereof. It was desired to develop a relatively quick and easy, non-contact, experimental method with which to identify important

sensor locations for complex systems that are difficult and time consuming to model. This was achieved through the use of a laser vibrometer. A laser vibrometer is a suitable tool to use for this purpose because of its mobility and its capability to gather vibration data in a non-contact manner. Laser vibrometers measure surface motion using the Doppler shift concept to measure the velocity of surface vibration [19]. Multi-point laser vibrometers have been used for several years for modal analysis but they have not been used for identifying important sensor locations. A test was performed in which a single beam laser vibrometer was used to measure the velocity of the surface of the aircraft at several locations. These values were then used to identify locations of high interaction.

Test Description

The laser vibrometer that was used for the tests was a Polytech OFV 2601 Laser Vibrometer Controller with a Polytech CLV Laser Unit and a Polytech CLV 700 Laser Head. To perform the laser vibrometer testing, the Super Hauler was placed in the test rig and the shaker was attached in the location marked by the blue dot in Figure 94. The Super Hauler was in the no pods and unloaded condition.



Figure 93. Laser vibrometer testing setup.

The laser vibrometer was mounted on a stand and directed to measure the vibration of the aircraft at the locations shown in Figure 94. All measurements were in the Z direction except for the two on the vertical stabilizer which were in the Y direction.

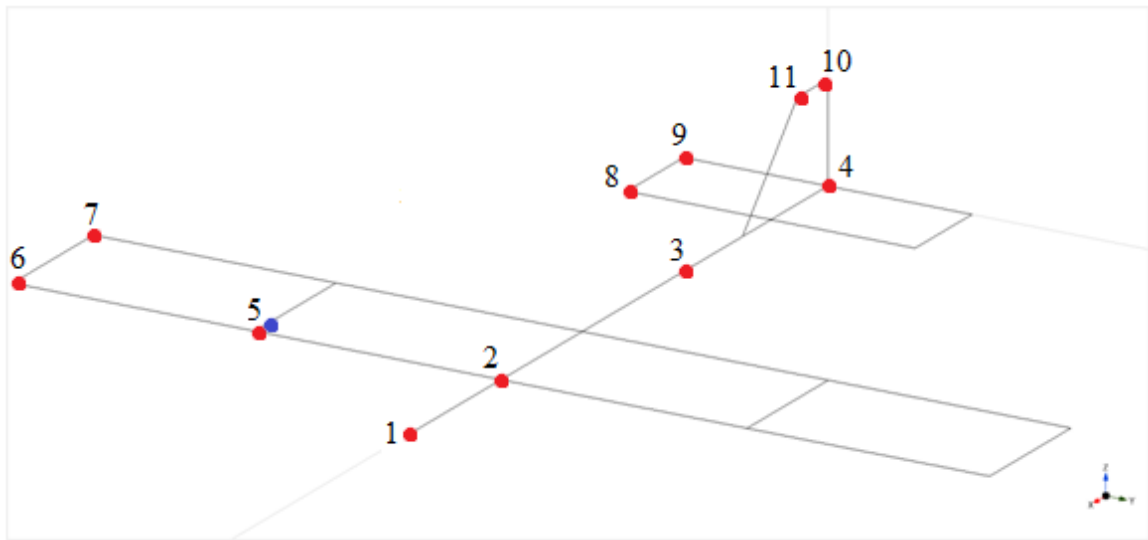


Figure 94. Excitation (blue) and measurement (red) locations for laser vibrometer tests.

The first step in the test procedure was to move the laser vibrometer to a measurement location and focus the laser to get a strong, clear signal. Next, the shaker was activated to vibrate the aircraft with random excitation. LabVIEW Signal Express was used to record the data from the vibrometer over a ten second period and export it to an Excel worksheet. These steps were repeated until three sets of data were gathered from each measurement location.

Results

A sample of the data gathered is shown in Figure 95. The graph shows the voltage measurements taken by the laser vibrometer of a test location versus time with the voltage corresponding to amplitude. As can be seen, the data wasn't centered around zero and there were some outliers due to noise in the laser vibrometer.

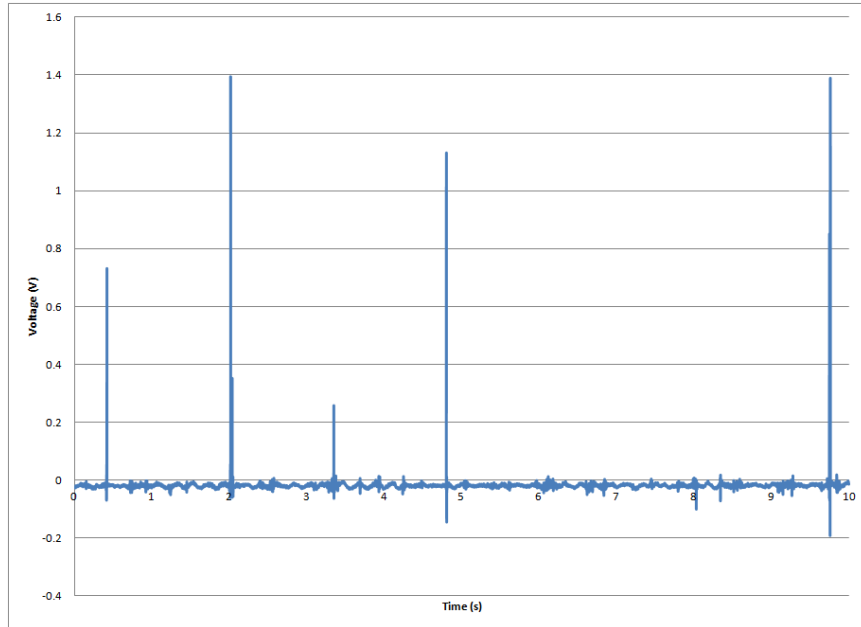
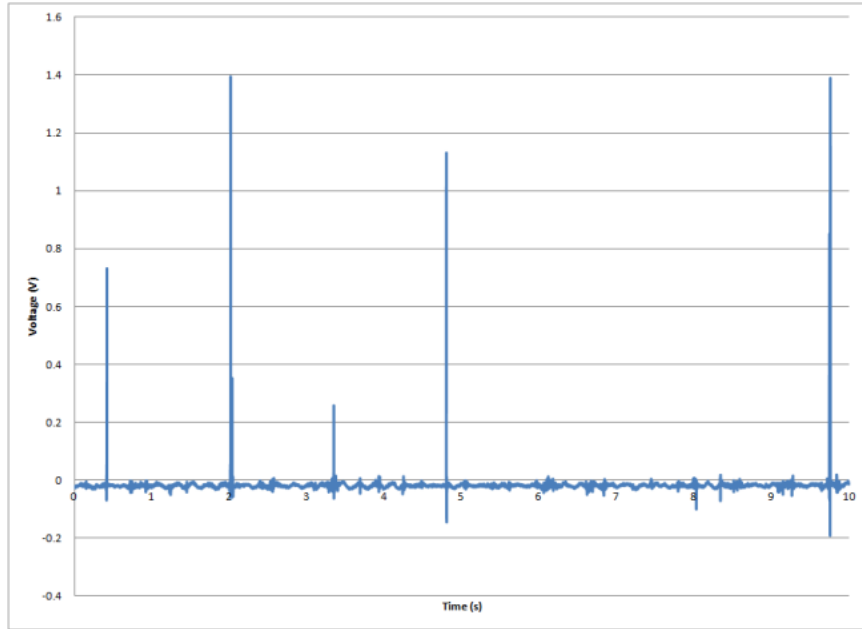


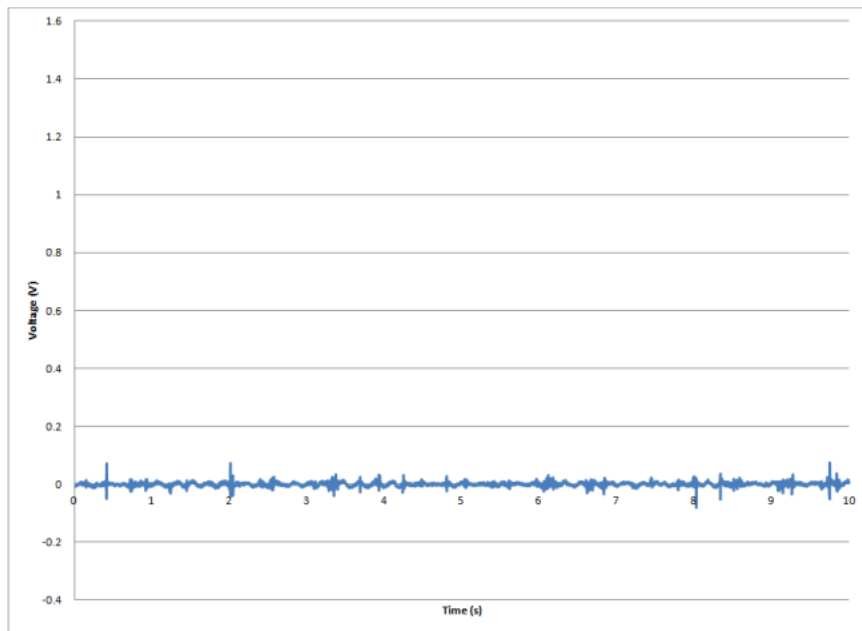
Figure 95. Sample data from the laser vibrometer.

Post processing was manually performed in Microsoft Excel to remove the outliers and then shift the data sets so that they had an average of zero. This was accomplished by manually deleting the outliers and then subtracting the average voltage from each value.

An example of a data set before and after post processing can be seen in Figure 96.



(a)



(b)

Figure 96. (a) Raw laser vibrometer data. (b) Data with outliers removed and adjusted for an average of zero.

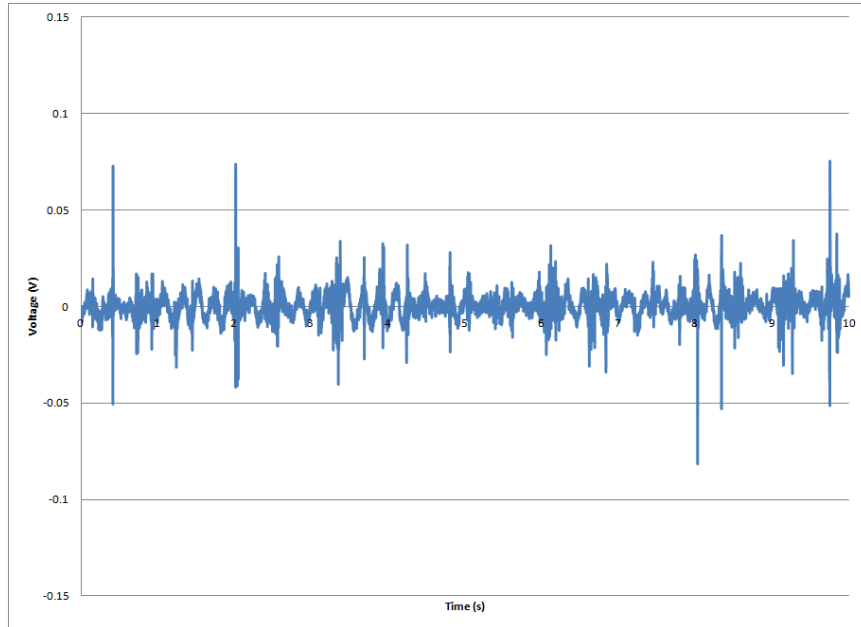


Figure 97. A zoomed in graph of Figure 96 (b).

To find an effective measure of the magnitude of vibration at each location, Equation (3) was used to calculate the Root Mean Square (RMS) value for each data set.

$$x_{rms} = \sqrt{\frac{1}{n}(x_1^2 + x_2^2 + \dots + x_n^2)} \quad (3)$$

A representative RMS value for each measurement location was then found by calculating the average of the three RMS values from the three data sets at each location.

The average RMS values can be seen in Figure 98.

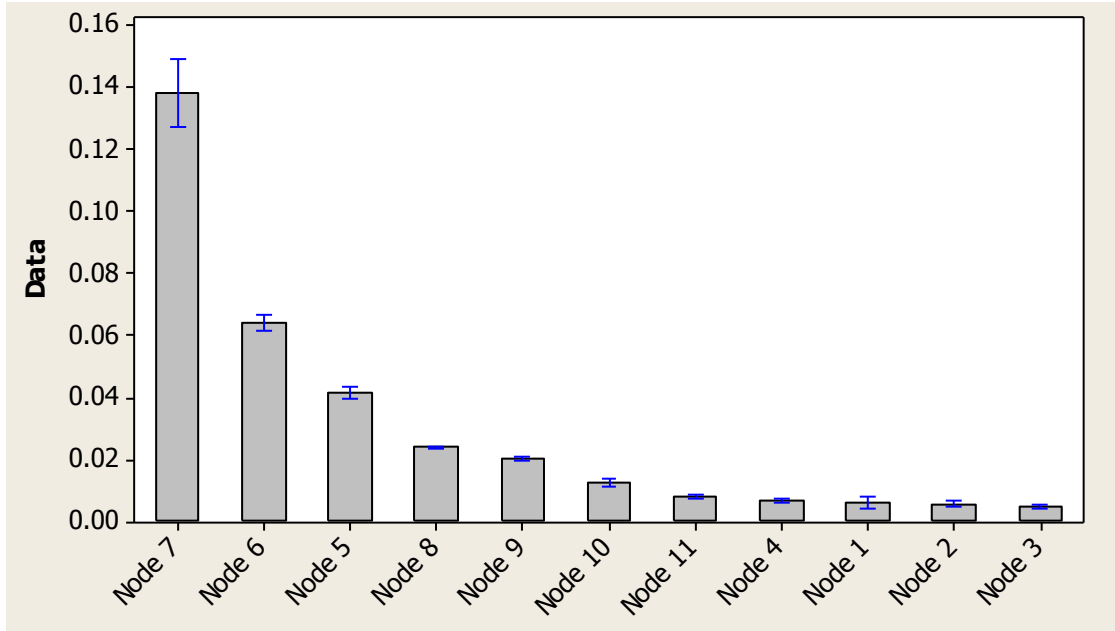


Figure 98. Average RMS values for laser vibrometer measurement locations with 95% confidence intervals.

This chart was created using Minitab with 95% confidence intervals. It can be seen that the nodes are distinctly different and the relatively small size of the error bars show that the tests were repeatable.

Statistical Method

Once the average RMS values were calculated, it was desirable to establish a statistical method to select the important modes at which accelerometers need to be placed. The method that was selected was a Pareto diagram.

Pareto diagrams were introduced in the field of quality control and are used to determine the most significant aspects of a body of information [20]. Resources can then be used on the important aspects and not wasted on trivial aspects. The general rule on which the Pareto principle is based is that 20% of the defects cause 80% of the problems.

The Pareto diagram method was applied to this test by first assuming all of the motion of the aircraft was captured by the measured locations. The average RMS values were then ordered from largest to smallest and the individual percentages of the total were calculated. These percentages were then summed to find a running cumulative percentage of the total aircraft motion captured. These results were then graphed and are shown in Figure 99. The average RMS values for each locations are shown in Table 10. A thorough screening of potential sensor locations must be conducted to help ensure that all the motion of interest is captured. The use of a laser vibrometer makes this process effective due to the efficiency of collecting data.

This diagram and table can be used to determine which locations should be measured. To capture 75% of the measured motion, nodes 5, 6, and 7, which are the nodes on the wings, should be instrumented. This corresponds to the W test. Alternatively, to capture 90% of the measured motion of the aircraft, nodes 8 and 9 would have to be instrumented as well. Nodes 8 and 9 are on the horizontal stabilizer so this level of instrumentation would correspond to the WH test. To capture even more motion, nodes 10 and 11 could be instrumented as well to bring the measured motion up to 95%. These nodes are on the vertical stabilizer so their addition would almost correspond to the WHV test, (node 11 wasn't included in WHV).

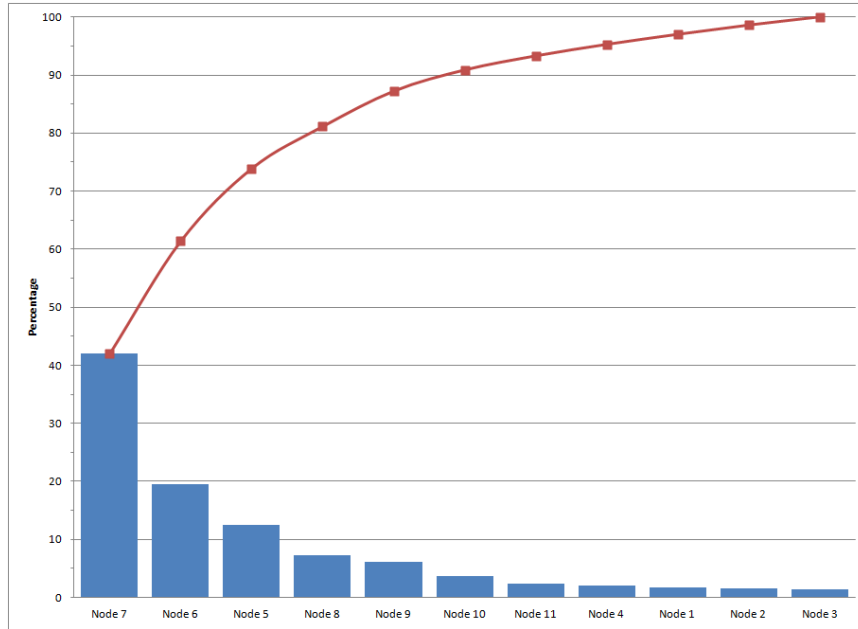


Figure 99. Pareto diagram for laser vibrometer test.

Table 10. Data used to create the Pareto diagram.

Location	Avg RMS	% of Total	Cum %
Node 7	0.1382	42	42
Node 6	0.0640	19	61
Node 5	0.0412	13	74
Node 8	0.0239	7	81
Node 9	0.0201	6	87
Node 10	0.0120	4	91
Node 11	0.0080	2	93
Node 4	0.0065	2	95
Node 1	0.0057	2	97
Node 2	0.0053	2	99
Node 3	0.0046	1	100
Total	0.3294		

A summary of the results from each of the tests, from the base test to the W test, are presented in Table 11.

Table 11. Summary of natural frequencies.

Base	WHV	WH	W	Description
12.4	12.4	12.4	12.4	Mode 1 wing bending
17.3	17.5	17.5	17.5	Tail torsion, antisymmetric wingtip bend
20.8	20.8	20.8	21.0	Wingtip, wing, tail, HS, VS torsion, wingtip bend
26.7	26.0	26.0	25.9	Wing torsion, slight HS bend
28.9	28.2	28.1	28.1	Symmetric wing torsion
30.2	30.8	30.8	30.7	Antisymmetric wingtip bend, tail wag
33.8	36.5	36.1	-	HS, VS torsion
39.9	39.7	39.8	39.8	HS bend/torsion, mode 2 wing bend, VS torsion
45.0	44.9	44.9	44.7	Mode 2 wing bend, HS bend/torsion, VS torsion
51.4	51.0	51.7	50.6	Wing torsion, HS bend/torsion
63.7	61.1	62.9	64.1	Antisymmetric wing torsion, HS bend, fuselage bend
72.3	73.3	72.0	71.9	Mode 2 wing bend/torsion opposite, HS torsion
74.4	75.9	75.9	75.8	HS torsion, mode 2 wing bend and torsion

It can be seen that, according to this test, 90% of the motion should be captured by sensors if all of the modes are to be recognized. The values chosen in this case were chosen because they coincide with the various surfaces of the aircraft. The WHV test corresponded to 95% of the measured motion being captured by sensors and consisted of the wings, horizontal stabilizer, and vertical stabilizer being instrumented. The WH test corresponded to 90% and sensors on the wings and horizontal stabilizer and the W test corresponded to 75% and the wings. Since the correct level is case dependent, this value should be left to user discretion.

It is recommended that, when using this method, the response is measured at grid points over the entire structure. However, this method is very sensitive to grid size since it can't distinguish if it is repeatedly capturing the same mode and so, if the grid is too fine, could identify multiple points as significant that all correspond to the same response.

Therefore, good candidate measurement locations are critical in using this method. The grid needs to be fine enough that all of the modes of interest (i.e. bending, torsion) are captured but not so fine that the same behavior is captured by several locations. A good candidate grid can be established from the structural response of similar structures, finite element results, or previous experience. However, additional points to those that are deemed potentially significant should be included as there could be unexpected participating modes. This method can help capture these unexpected modes that occur due to complex structural interactions or complex structural response.

CHAPTER VI

DETERMINATION OF AIRWORTHINESS

Flutter Overview

One of the main reasons that a ground vibration test on the Super Hauler was conducted was to determine if the aircraft was still airworthy after the addition of wing pods. A major concern in aircraft is aeroelastic flutter. Aeroelastic flutter is defined as involving the interaction of aerodynamic, elastic, and inertial forces on structures that produces an unstable oscillation that often results in structural failure [21]. Flutter is typically observed on surfaces, such as wings and tails, that encounter large aerodynamic loads [22].

Flutter occurs when the aerodynamic forces associated with motion in two modes of vibration (i.e. wing bending/torsion) cause the modes to couple adversely [23]. An uncontrolled increase in vibration amplitude is observed when the aircraft is moving fast enough that the structural damping is insufficient to quell the motion coming from aerodynamic energy being added to the surface [24]. Because of this, flutter can be disastrous when it occurs on an aircraft; even causing the wings to vibrate in increasing amplitude until they fall off of the aircraft.

Flutter is a complex field and much work has been done on developing methods and tests to identify and predict flutter. These tests include both ground vibration tests

and flight tests that include structural excitation, response measurement, and data analysis for stability [21]. Many flutter identification methods have been developed and a few are discussed below.

The most commonly used method is damping extrapolation [25]. This method is based on flight data and consists of extrapolating trends of modal damping [21]. When flutter starts, the damping of at least one mode goes to zero so this method notes the variation in the modal damping values with airspeed and extrapolates the values to find a critical airspeed where damping is zero.

The envelope function method predicts flutter using the time-domain measurements from sensors that measure the response to an impulse excitation [26]. This method states that the envelope bounding an impulse response increases as damping decreases. So a loss of damping, and thus the start of flutter, is indicated by the size and shape of the response envelope. A time centroid is also needed to establish stability since the amplitude of the envelope can be affected by the size and shape of the impulse. The final step in this method is to predict the flutter using a shape parameter which is the inverse of the time centroid and is assumed to be a polynomial function of airspeed. The flutter speed can then be calculated from the shape parameter.

The Zimmerman-Weissenburger margin method states that the flutter margin is an indicator of distance to flutter in terms of dynamic pressure [27]. This method was developed using the equations of motion for a classical aeroelastic system with bending and torsion modes. The method uses the characteristic polynomial that describes the

continuous-time aeroelastic system. The stability of the system is then established using the Routh stability criterion to find a parameter that is positive if the corresponding system is stable. The onset of flutter is then calculated by noting that the parameter that was found varies with dynamic pressure, thus the dynamic pressure at which flutter starts can be calculated from this parameter.

A flutterometer is a tool that can be used to predict flutter speeds using both theoretical models and FRFs [28]. This approach is based on μ -method analysis which computes a stability measure that is robust with respect to an uncertainty description. The largest increase in airspeed where the theoretical model remains stable with respect to the uncertainty is then the flutter speed.

New aircraft are investigated for flutter from the early stages of design and are tested for flutter with GVTs and flight flutter tests [29-35]. GVTs are used to find the structural properties of an aircraft which are then used to validate the quality of an analytical model and its flutter predictions. The natural frequencies, damping ratios, and mode shapes found from the GVT are used to determine the error and uncertainty in the analytical model and are necessary in determining aeroelastic characteristics such as flutter [36, 5]. The results can also be used in wind tunnel tests or flight flutter tests [37, 38]. These tests are performed to determine the flight envelope of an aircraft, including the flight flutter speed and frequency.

The results from the GVTs were used in a preliminary flutter study. A full flutter study was not performed on the Super Hauler but the results from the GVTs could be

used for further flutter tests such as flight tests or wind tunnel tests. The Super Hauler has been flown for several missions without the wing pods so the stability of the aircraft without wing pods had been established. The tests were performed to see if the addition of the wing pods changed the modes of the aircraft to the extent that flutter would be introduced in normal flight operations. Since the aircraft was well established as stable without the wing pods, the results from the tests were examined to see if the addition of the wing pods shifted the frequencies of the bending and torsion modes so that they were coincident.

Flutter Results

The primary location on an aircraft where flutter is a concern is the wings. Table 12 summarizes the modes that were dominated by wing motion and it can be seen that none of the frequencies aligned so that there were coupled torsion and bending modes. For instance, without pods, mode 1 wing bending was observed at 12.4 Hz with a wing torsional mode at 28.9 Hz. The addition of the pods moved both of those frequencies to 11.0 Hz and 20.6 Hz, respectively, but they still remain two distinct modes. There is still a possibility that flutter could occur at a critical airspeed, but that behavior could only be established by further testing, including a flight flutter test or a wind tunnel test.

Table 12. Summary of wing modes.

No Pods	Pods	Description
12.4	11.0	Mode 1 wing bending
28.9	20.6	Symmetric wing torsion
29.5	23.2	Antisymmetric wingtip bend, HS bend/torsion, tail wag
30.2	24.8	Antisymmetric wingtip bend, tail wag
45.0	34.0	Mode 2 wing bend, HS bend/torsion, VS torsion
51.4	38.3	Wing torsion, HS bend/torsion
63.7	47.4	Antisymmetric wing torsion, HS bend, fuselage bend

The modes that were observed to contain potential for flutter with a combination of bending and torsional modes were noticed in the horizontal stabilizer and are summarized in Table 13. It can be seen that these modes appeared in the no pods configuration as well as with pods. This leads to the conclusion that the structural damping within the horizontal stabilizer is sufficient to overcome the flight loadings. As flight loadings are smaller on the horizontal stabilizer, flutter is not as significant of a problem on this surface.

Table 13. Summary of potential horizontal stabilizer flutter modes.

No Pods	Pods	Description
29.5	23.2	Antisymmetric wingtip bend, HS bend/torsion, tail wag
39.9	-	HS bend/torsion, mode 2 wing bend, VS torsion
45.0	34.0	Mode 2 wing bend, HS bend/torsion, VS torsion
-	40.9	Mode 2 wing torsion, HS bend/torsion

Flight Test

The Super Hauler was flown in July 2012 with the wing pods attached. Dummy weights were placed in the pods to simulate a payload. The weights added brought the

total weight of the pods to 5 lbs each. An image that was taken during the flight in which the pods are visible is shown in Figure 100. The flight was successful with no problems during flight and there was no noticeable change in the flight characteristics or handling of the aircraft.



Figure 100. The Super Hauler in flight with the wing pods installed.

The preliminary flutter tests showed that the addition of the wing pods didn't introduce behavior that is a significant cause for concern. This was proven by a successful flight test. However, the discovery of some flutter characteristics in the horizontal stabilizer will lead to the UASE lab increasing the tension in the stabilizer wires on the Super Hauler. This will change the frequency response in the horizontal stabilizer and help reduce potential flutter tendencies.

CHAPTER VII

CONCLUSION

A full modal analysis investigating the effect of wing pods on a small UAS was presented. The pods were shown to lower the natural frequencies for corresponding mode shapes due to the mass added to the structure. An airworthiness investigation was performed and it was discovered that no wing flutter was introduced into the system with the addition of the pods. This leads to the conclusion that the wing pods are a safe addition to the aircraft and was demonstrated by a successful flight test of the UAS with the wing pods installed. No flutter behavior was observed and no change was noticed in how the aircraft handles.

A study was done on channel reduction and five tests with different levels and types of channel reduction were performed and analyzed. The stick model was found to be a poor option for channel reduction as torsional motion was undetectable and mode identification was very difficult. It was seen that it is better to simplify the model by keeping a more complex model and removing accelerometers from different surfaces. Three tests reducing channels in this manner were performed. From these tests it was found that the sensors along the fuselage of the aircraft and on the vertical stabilizer are unnecessary for this testing since all of the modes were still identifiable and knowledge of the motion in these surfaces was unnecessary for airworthiness determinations. The

sensors on the wings and horizontal stabilizer were found to be necessary. This conclusion was reached because of the loss of ability to identify a mode involving only horizontal and vertical stabilizer motion when only the wings were instrumented. Using these findings, the number of channels used in this test could be reduced from 24 channels down to 10 channels. This reduction not only saves money by using less sensors and supporting equipment, but also saves time that would have been spent on data collection and analysis on the 14 extra channels.

A novel sensor location identification method was presented. This method was shown to provide a quick, relatively simple, non-contact, and experimental way to determine important sensor locations through the use of a laser vibrometer. The recommended testing procedure to follow when using the sensor location identification method is outlined below.

- Set up the structure in a test rig so that it has free-free boundary conditions
- Install a shaker at an location where all of the modes of the structure are excited
- Decide upon and lay out an appropriate grid pattern at which to take measurements with the laser vibrometer
- Take measurements at the grid points using the laser vibrometer
- Process the output data to remove noise and any DC offset in the data
- Calculate the RMS values
- Construct a Pareto diagram to see the strongest contributing locations from the measured values

- Decide upon an appropriate Pareto level
- Instrument the structure with accelerometers at the significant locations
- Perform modal analysis
- Extract natural frequencies and modal shapes from the FRFs
- Analyze the results

This development could be of interest to the vibration community as there hasn't been any evidence found of a similar method. The laser vibrometer was used to measure the response at several locations along the aircraft and the RMS values were calculated. A Pareto diagram was used to identify which of these locations are important to instrument by identifying which locations contribute to most of the motion experienced by the aircraft. This method would be most effectively used by measuring the motion at several locations on the structure and placing sensors at the nodes that capture a certain percentage of the motion that was measured. This provides the user with the flexibility to choose the percentage of motion that is important for that structure.

APPENDICES

Appendix A ModalVIEW Tutorial

This tutorial will highlight the steps required to set up and perform a basic modal analysis in ModalVIEW. The tutorial is split up into General Overview, Drawing 3D Structure Model, Performing Measurement, Experimental or Operational Modal Analysis, and Modal Shape Animation.

General Overview

The main window that is seen when first starting ModalVIEW is shown in Figure 101.

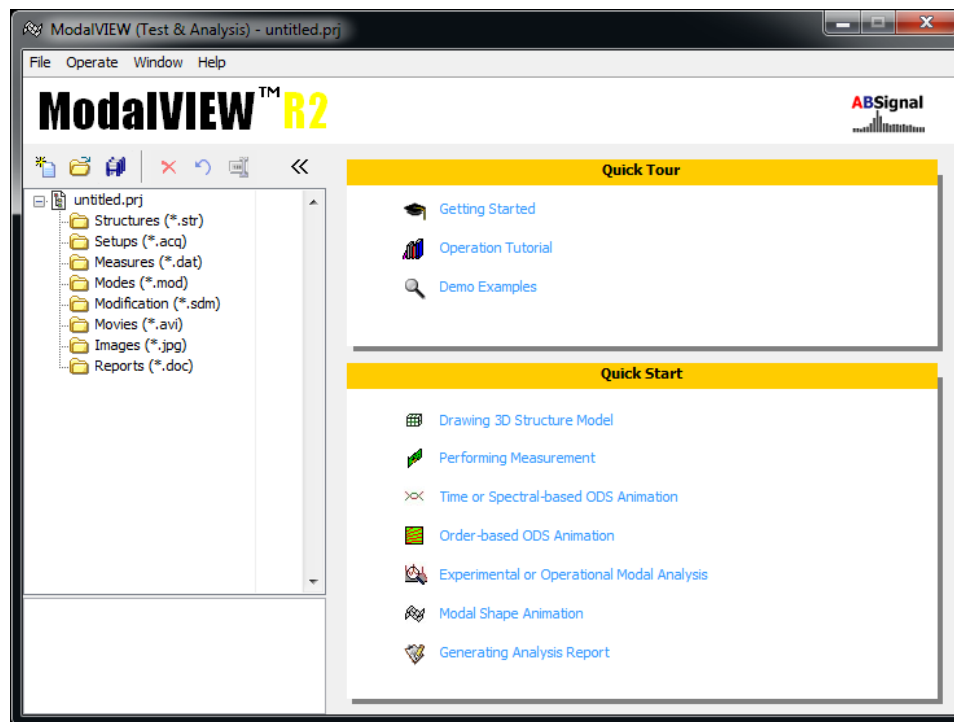



Figure 101. Main window for ModalVIEW.

Points are placed by first selecting the  (Add Object) button in the Structure Editor Window while making sure the drop down list next to the button is set to Points. Click in the Structure 3D View window in the general locations that the points should be located. Click the Add Object button again to deselect the option. This can be seen in Figure 103.

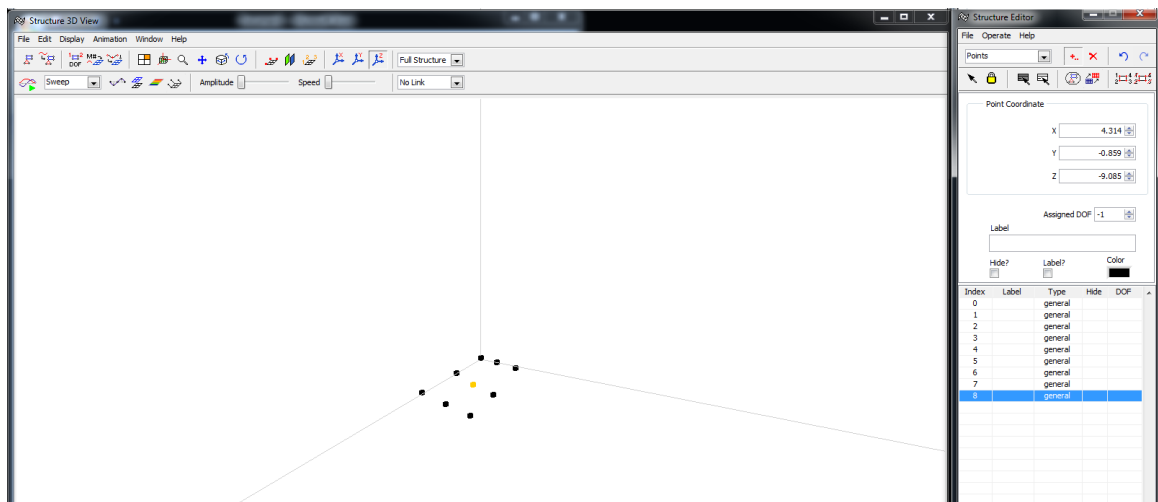


Figure 103. Initial point placement in Structure 3D View window.

The coordinates of each point can now be set by selecting the point and entering the point coordinates in the spots provided in the Structure Editor Window. The DOF of each point should also be assigned. An example of this can be seen in Figure 104.

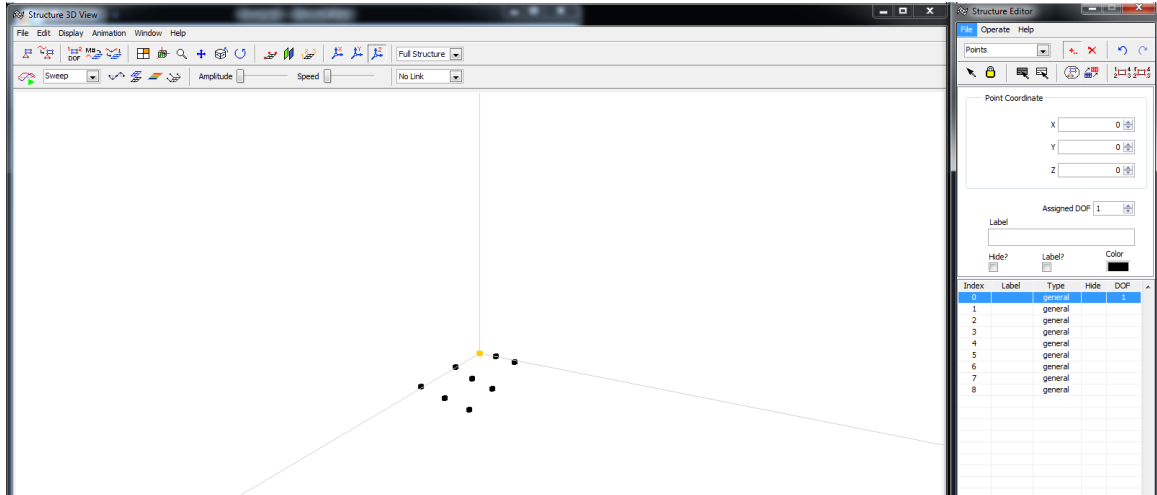


Figure 104. Setting coordinates for the points in the structure.

To zoom in or out on the structure, click on the magnifying glass in the Structure 3D View window and click and drag the mouse in the window. The next step is to add lines to the structure. To do this, select Lines needs from the drop down list and then click the Add Object button. To create a line between two points, click on each point and a line will be created.

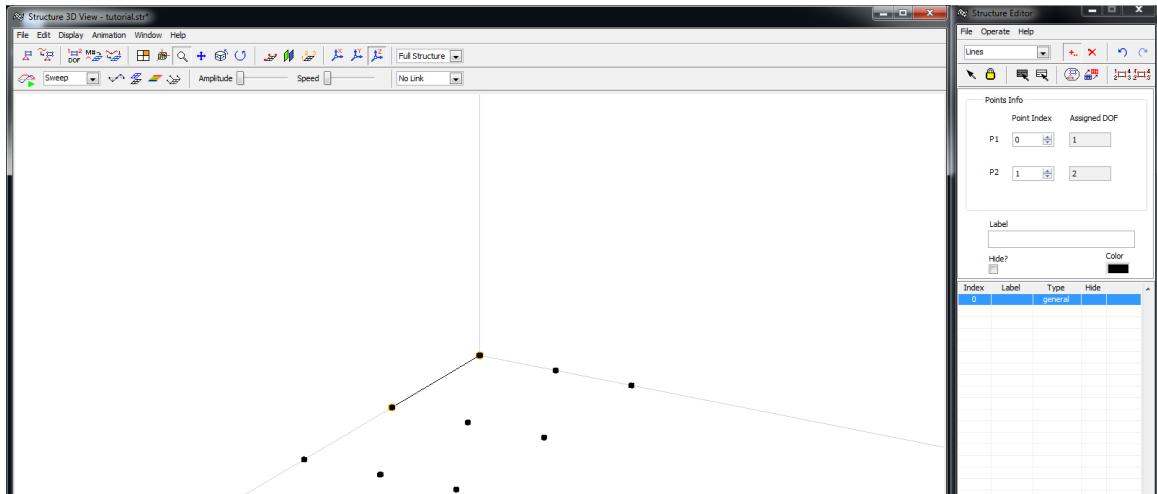


Figure 105. Adding lines to the structure.

Continue doing this until all of the lines are created. Once the structure is complete, save the structure by clicking File > Save As and enter the desired file name. The completed plate can be seen in Figure 106.

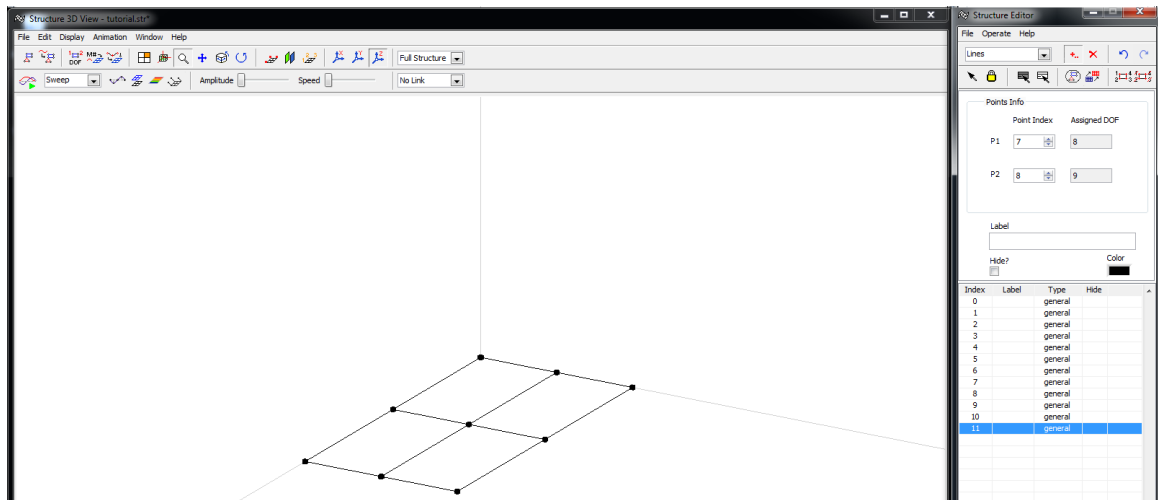


Figure 106. Completed structure.

Performing Measurement

The next step in the modal analysis process is to measure the response. First, the structure needs to be fully instrumented with the DAQ connected to the computer that is equipped with ModalVIEW. The Performing Measurement link can then be clicked and the window shown in Figure 107 will come up.

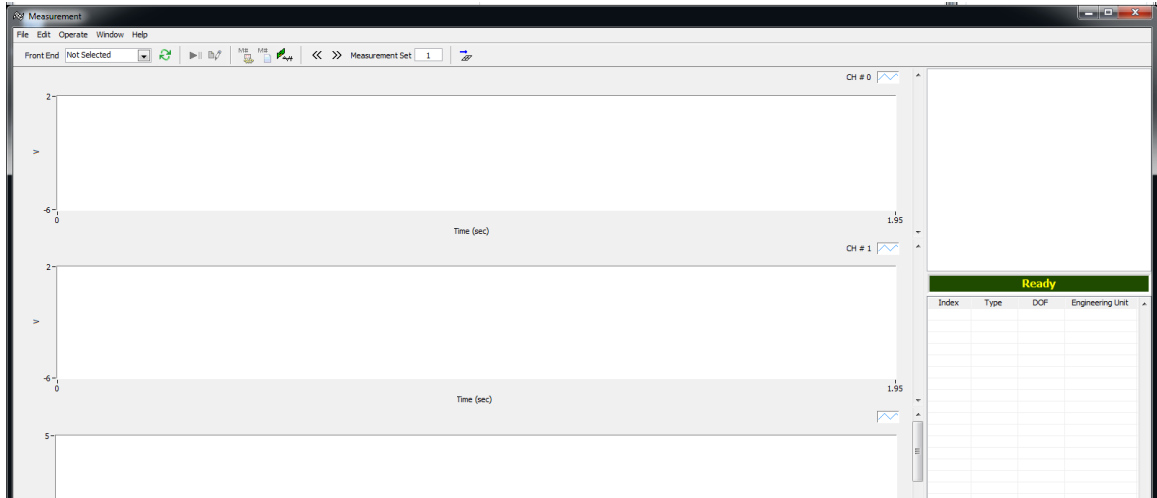


Figure 107. Performing Measurement window.

The front end, or the DAQ, needs to be selected from the drop down list in the upper left hand corner (shown in Figure 108). The settings for the measurements can then be selected.

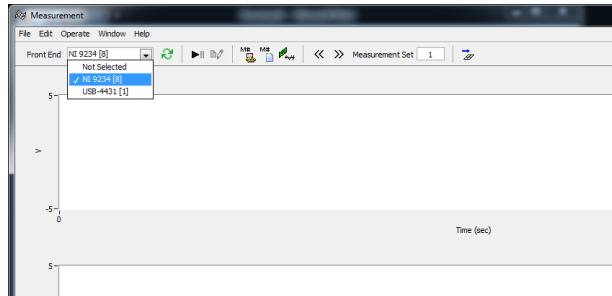



Figure 108. Selecting the DAQ.

To pull up the DAQ Setup menu, click on the  button. The following window will open.

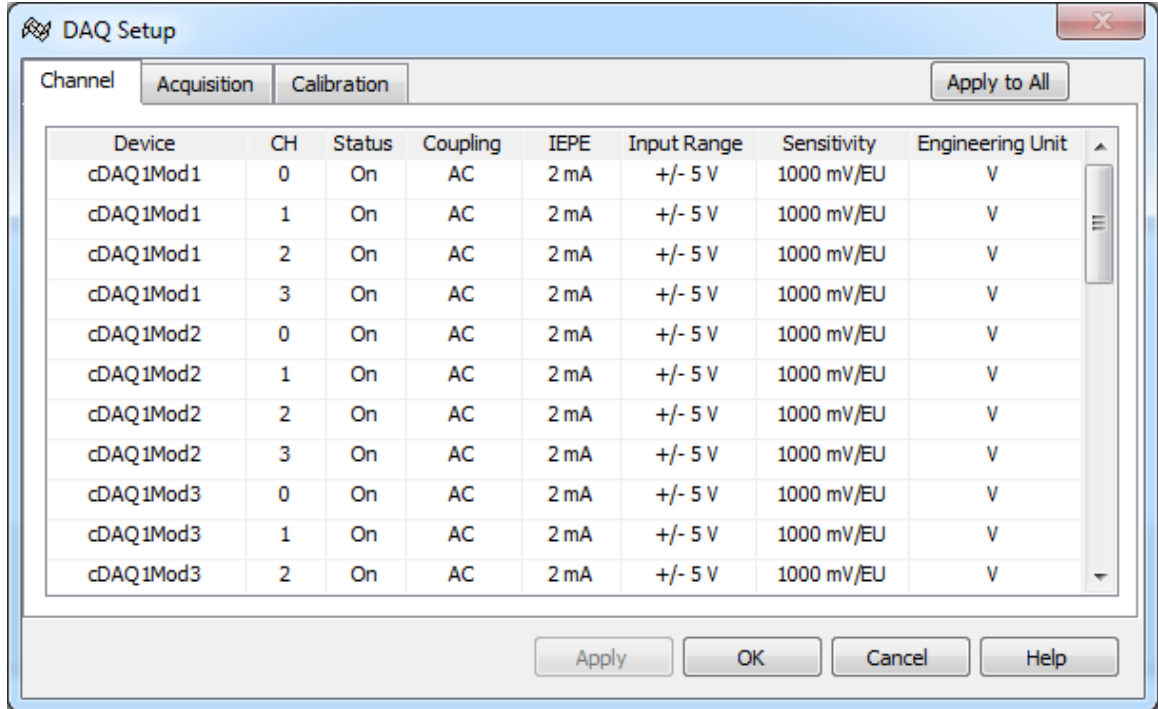


Figure 109. DAQ Setup window.

Under the Channel tab, turn off the channels that will not be used by clicking on the On in the Status column that corresponds to the unused channel and select Off. The options in the Acquisition tab can be seen in Figure 110.

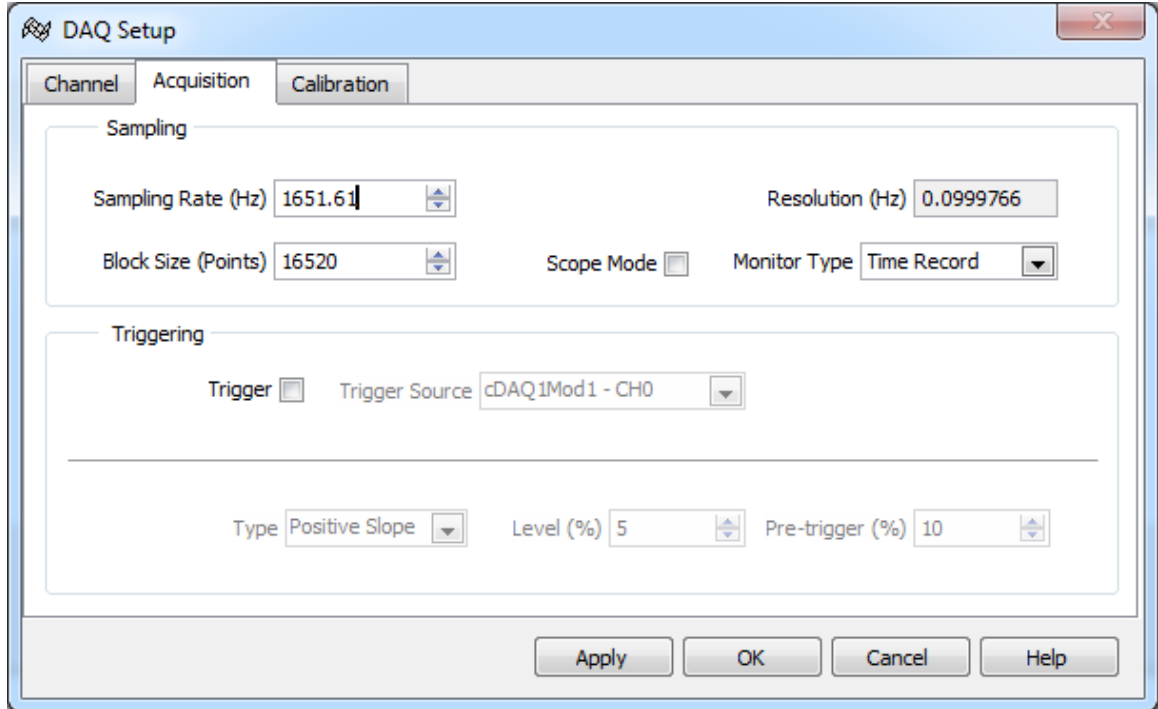



Figure 110. DAQ Setup window, Acquisition tab.

The sampling rate should be left at the default as it is specific to the DAQ and is automatically recognized by ModalVIEW, but the resolution can be adjusted by changing the Block Size. It is recommended to increase the resolution from the default of about 1 Hz to a resolution closer to 0.1 Hz. These settings can be applied by clicking Apply then OK.

To pull up the Test Setup menu, click on the  button. The following window will open.

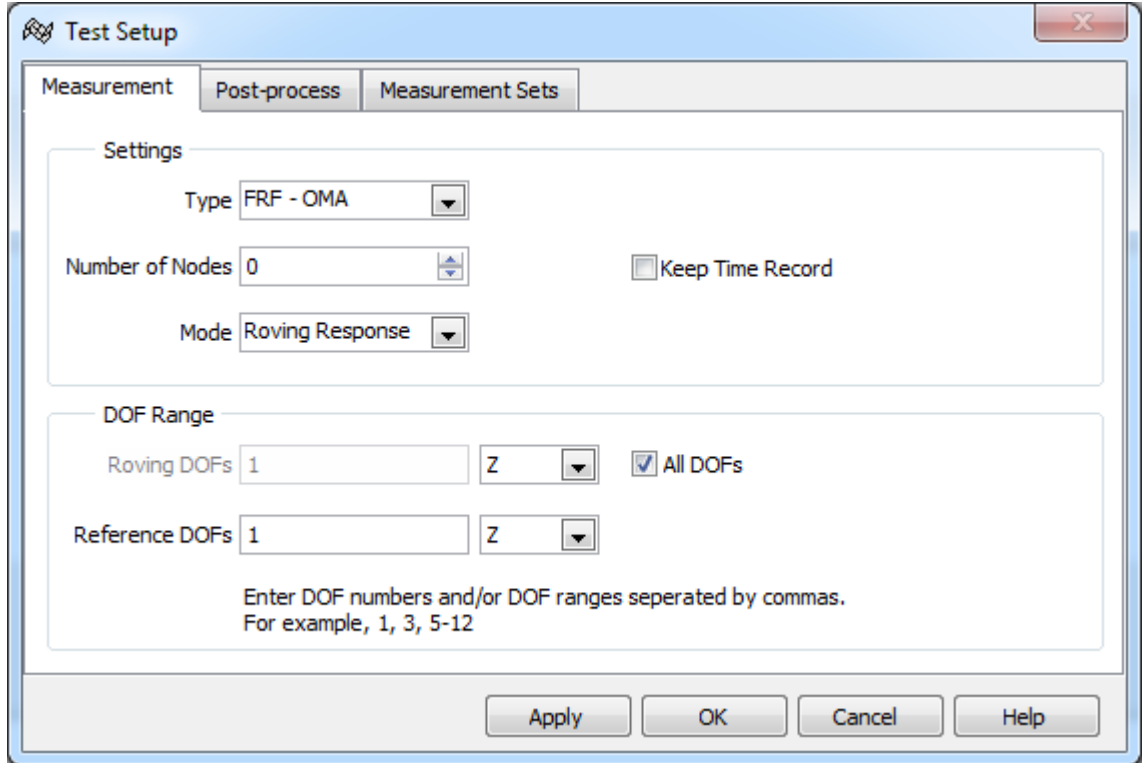


Figure 111. Test Setup window.

In the Measurements tab, set the measurement type to FRF-EMA for experimental modal analysis by selecting FRF-EMA in the Type drop down menu. Adjust the number of nodes to the number that will be instrumented. The options in the Post-Process tab can be seen in Figure 112.

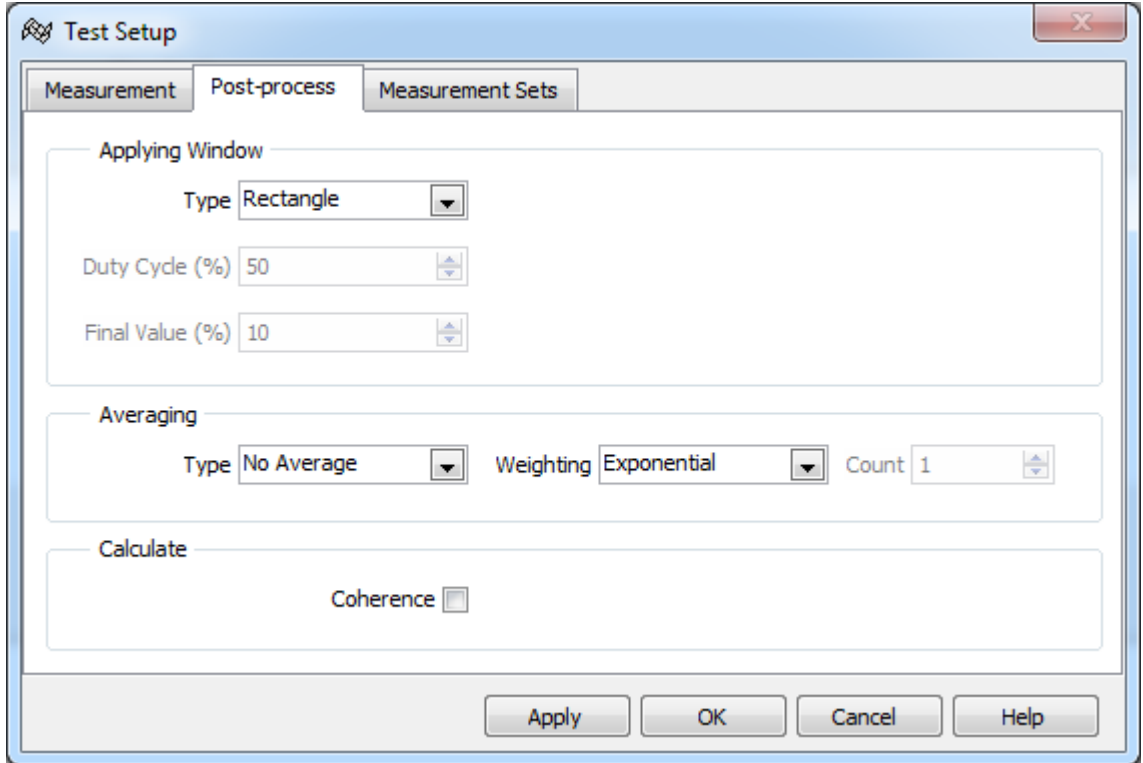


Figure 112. Test Setup window, Post-process tab.

The windowing type can be changed to the desired windowing in the type drop down menu. The options in the Measurement Sets tab can be seen in Figure 113.

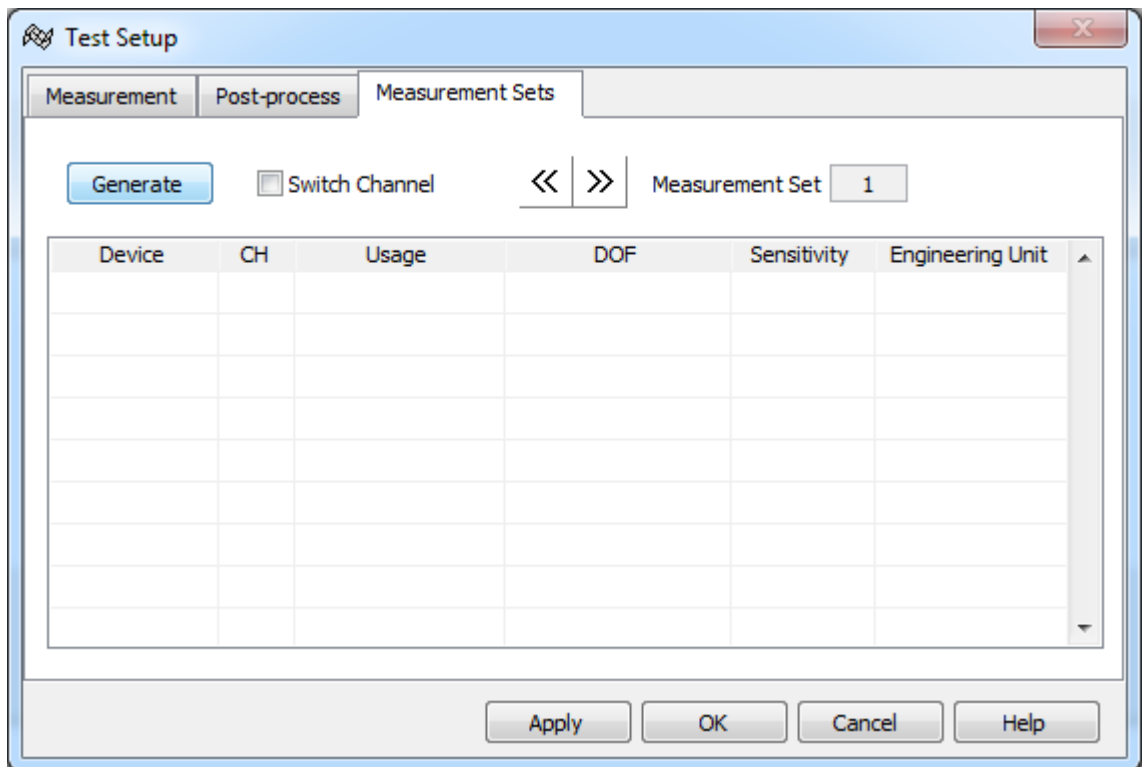


Figure 113. Test Setup window, Measurement Sets tab.

The channels are automatically generated when the Generate button is clicked.

This can be seen in Figure 114.

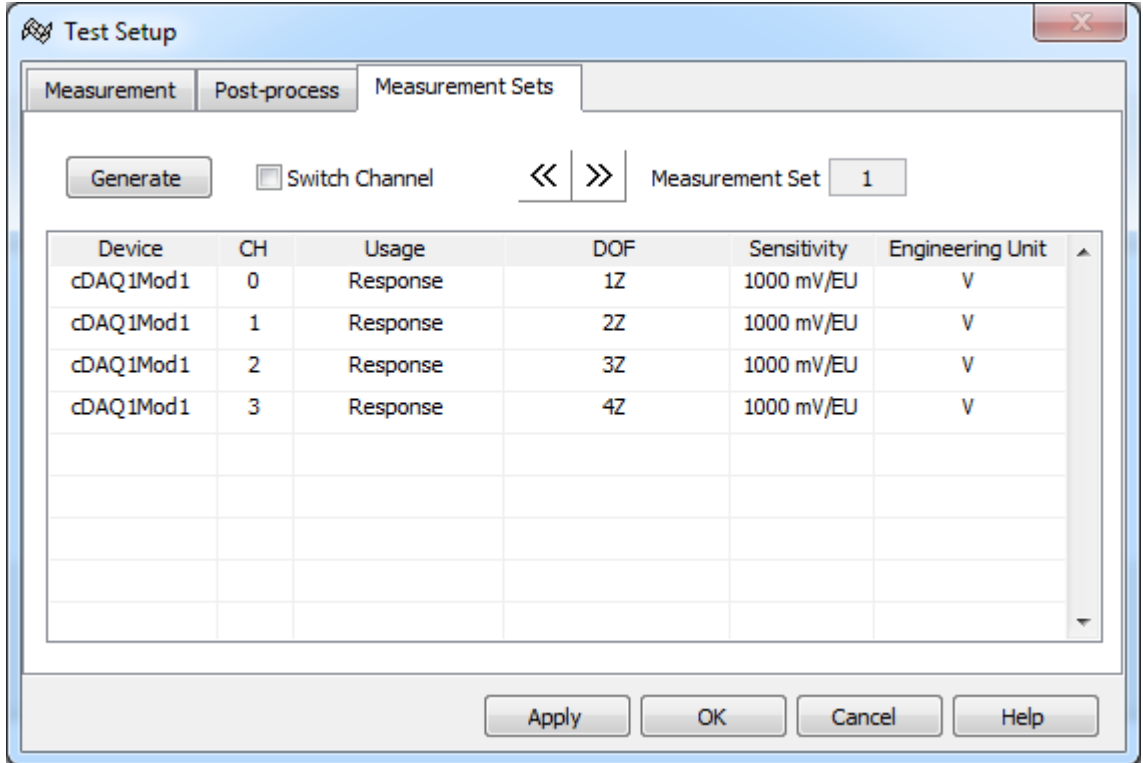


Figure 114. Channels generated in the Measurement Sets tab.

The appropriate DOF and direction which each channel measures can be set by clicking on the corresponding value in the DOF column and adjusting the value accordingly. An example of this can be seen in Figure 115.

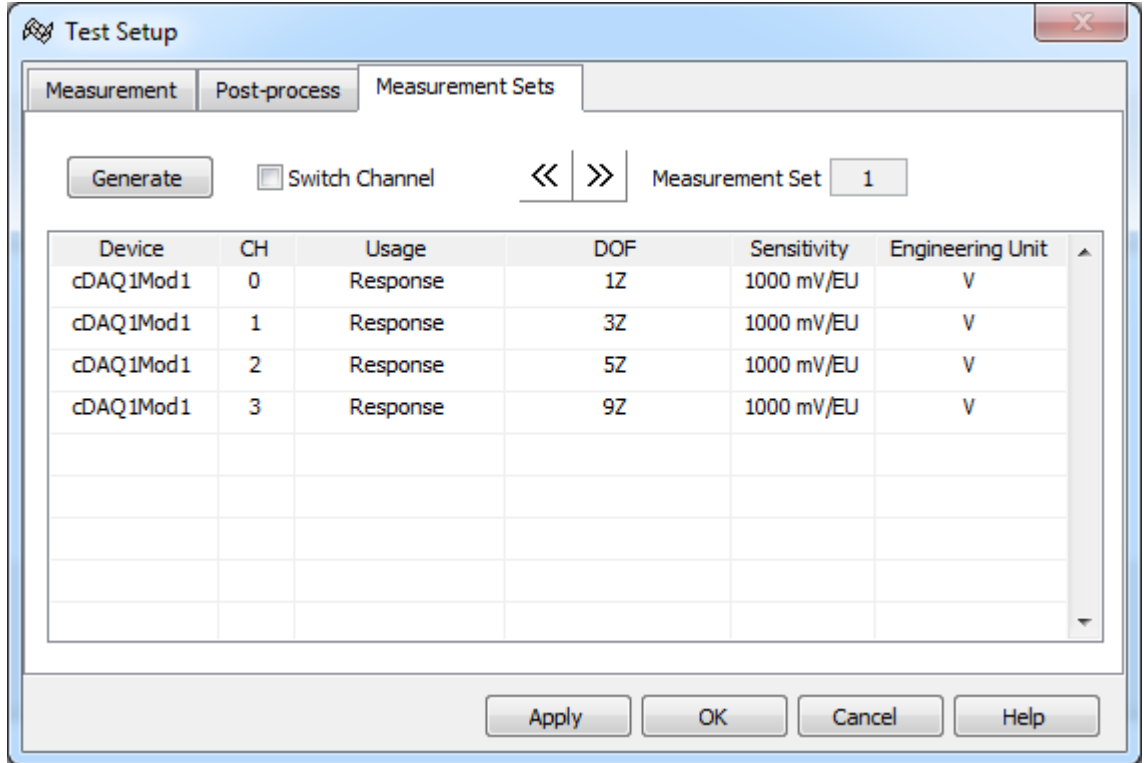



Figure 115. Appropriate DOFs selected in Measurement Sets tab.

Apply the settings by clicking Apply then OK. To save the configuration for later use, click File > Save Config As.

To pull up the Signal Generator menu, click on the  button. The following window will open.

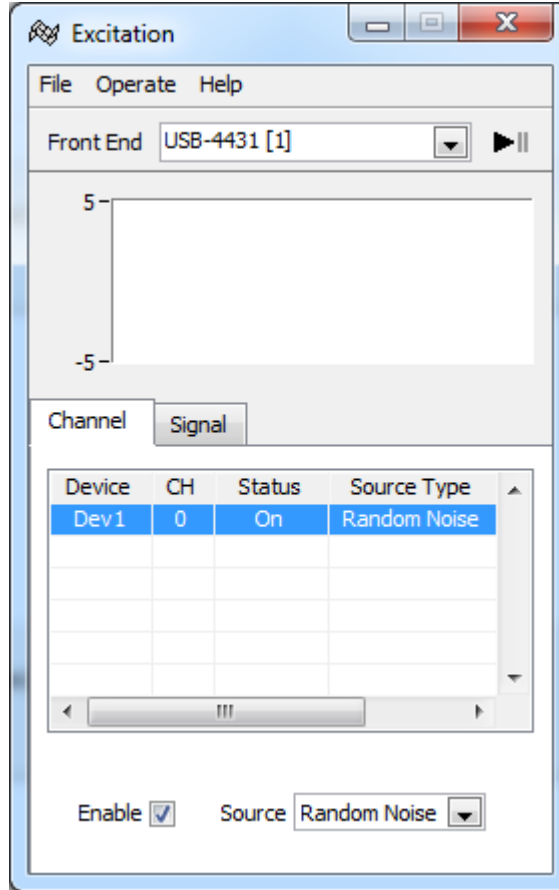


Figure 116. Signal Generator Excitation window.

Select the appropriate DAQ in the Front End drop down menu then check the Enable box to enable excitation. Select either Random Noise or Swept Sine excitation in the Source drop down menu. The signal options (such as amplitude and period) can be set in the Signal tab which can be seen in Figure 117.

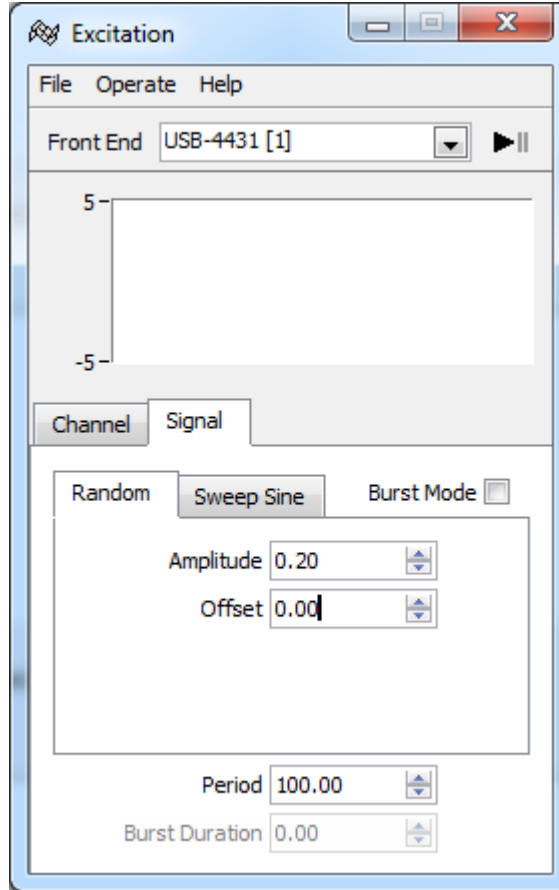




Figure 117. Signal options in Excitation window.

To start or stop the excitation click the  button in the Excitation window. To start taking measurements click the  button in the Measurement window. The program will collect measurements for the amount of time necessary for the assigned resolution and, when finished, will open a dialog window asking "Do you want to keep measurement". If the measurement looks good, click OK. Save the measurement by clicking File > Save Measurement. Delete the data from the spreadsheet when asked and repeat steps to collect another measurement.

Experimental or Operational Modal Analysis

The next step in the modal analysis process is to perform the actual modal analysis. To do so, click the Experimental or Operational Modal Analysis link in the main window. The following window will open.

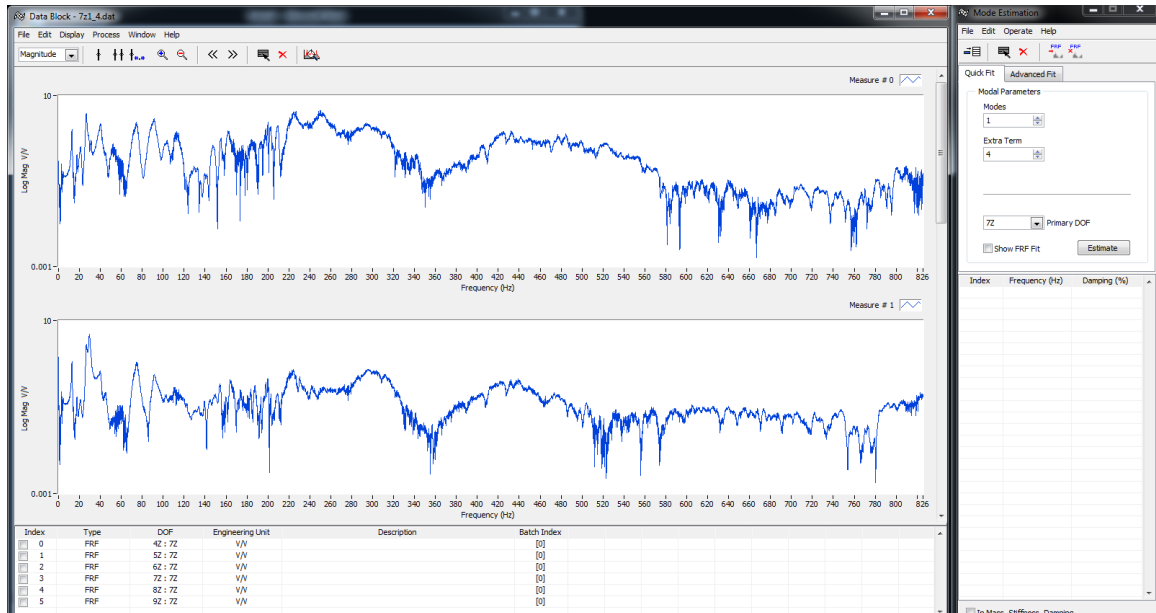



Figure 118. Experimental or Operational Modal Analysis window.

Select the measurement set to analyze by clicking File > Load. To change the axis from a log scale, right click on the axis and uncheck the log option. Zoom in on an area of interest by clicking on the + magnifying glass and selecting the area of interest. Click the Band Cursor button  to display bounds. This can be seen in Figure 119.

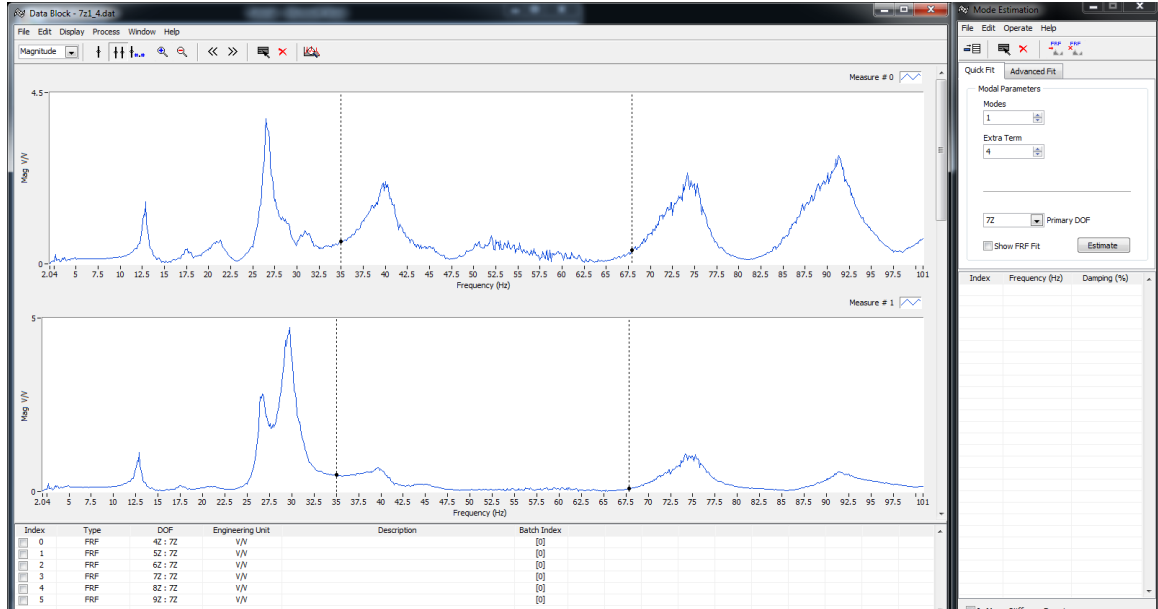


Figure 119. Measurement bounds.

Move the bands to bookend a small range. In the Mode Estimation Window check the Show FRF Fit box, adjust the Extra Term to a value around 10. Click Estimate to show an estimated curve fit. This can be seen in Figure 120.

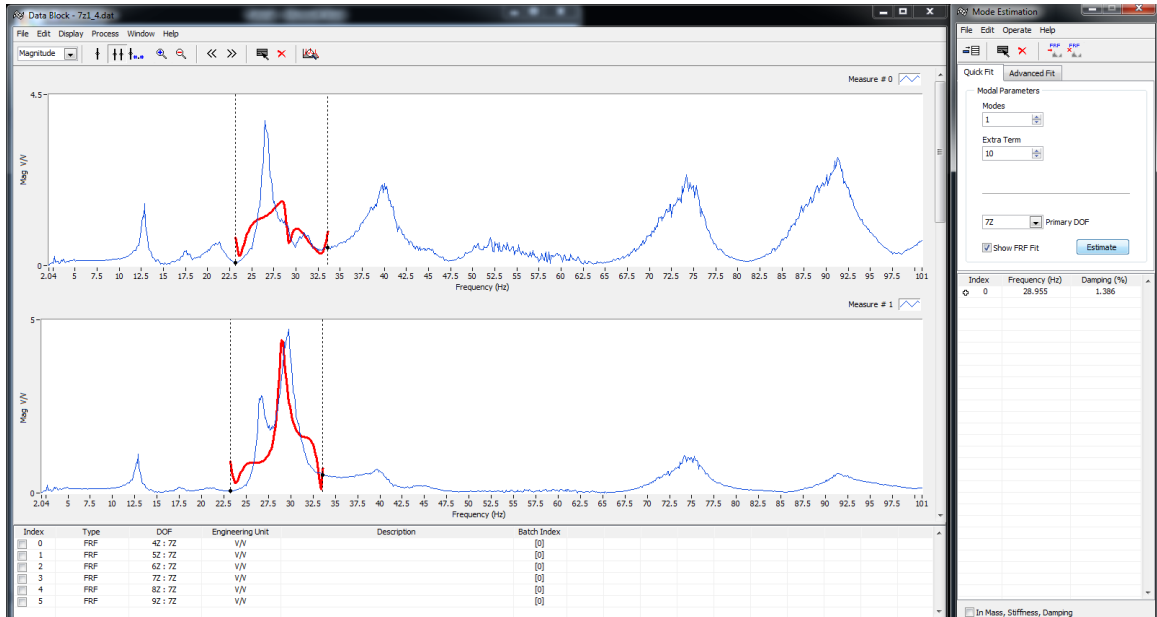


Figure 120. Estimated curve fit.

Increase the number of modes (click Estimate to refresh the curve fit) until there is a good curve fit. This can be seen in Figure 121.

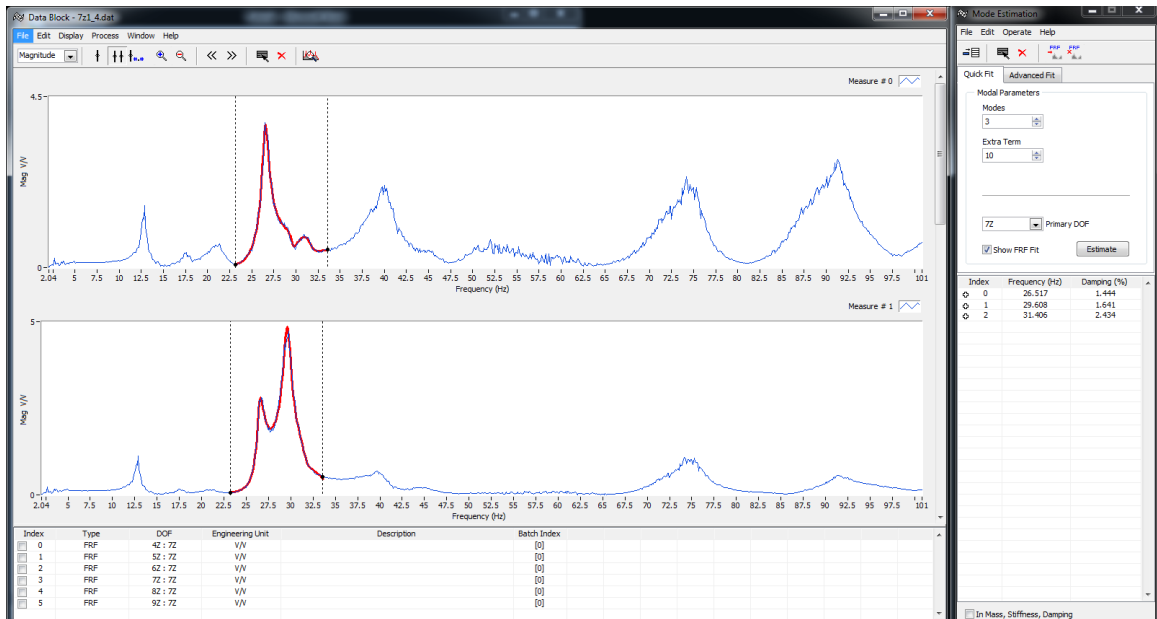



Figure 121. Good curve fit in modal estimation.

The natural frequency values corresponding to the modes are listed in the Mode Estimation window. To add these modes to the list, click the  button. Move the bands to the next area and repeat the curve fit steps. An example of this can be seen in Figure 122.

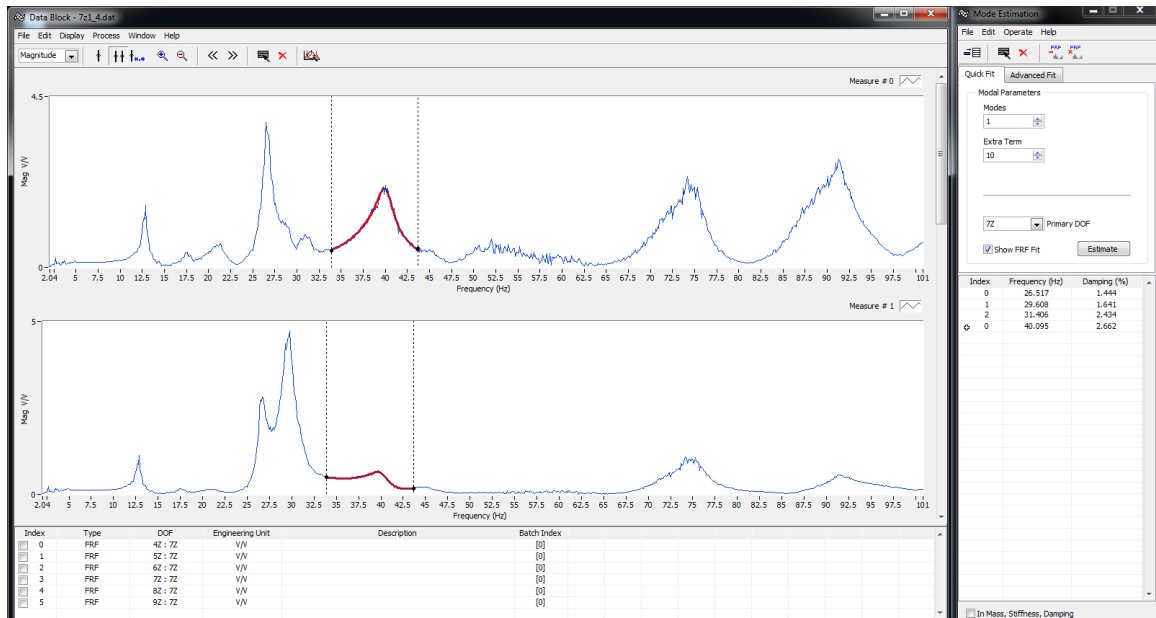


Figure 122. Further modal analysis.

Continue these steps until the modes have been found for the entire area of interest. When finished, click File > Save Mode Table in the Mode Estimation Window to save the mode table.

Modal Shape Animation

The last step is to animate the structure. Click the Modal Shape Animation link in the main window. The following window will open.

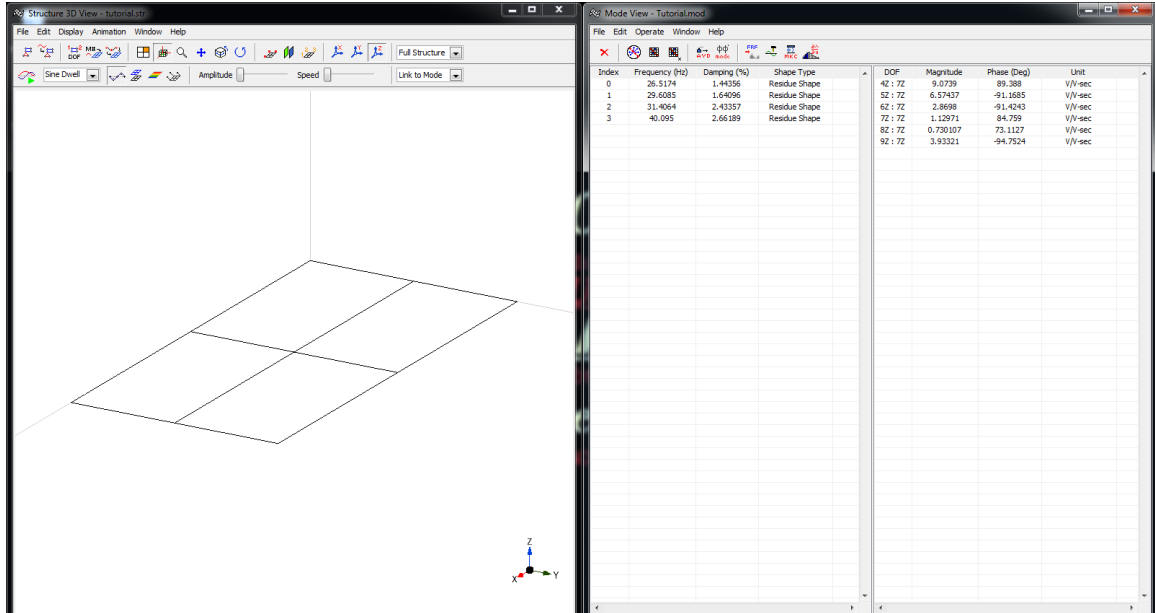




Figure 123. Modal Shape Animation window.

In the Structure 3D View Window click the Assign Measurements  button to automatically assign the measurements to the DOFs. Click the  button to start animation. Adjust the amplitude and speed of animation using the sliders. Click on different modes in the Mode View window to animate the modes. To export a movie, select the mode to export, set the desired amplitude, pause the animation, then click File > Export Movie. The frame rate of the movie is set in the main menu by clicking Operate > Options > Structure then adjusting the Frame Rate value.

REFERENCES

- [1] J. Alme, *Vivaldi Antenna Design for X Band Electronically-Steered Antenna Arrays and Phased Array Radars*, University of North Dakota: Department of Electrical Engineering, 2009.
- [2] D. Hajicek, *Electronically-Steered Phased Array Antenna Design for Integration Into Small Unmanned Aircraft Systems*, University of North Dakota: Department of Electrical Engineering, 2009.
- [3] K. J. Lemler and W. H. Semke, "Structural Analysis of the Effects of Wing Payload Pods on Small UAS," in *30th International Modal Analysis Conference*, Jacksonville, Florida, 2012.
- [4] M. W. Kehoe, "Aircraft Ground Vibration Testing at NASA Ames-Dryden Flight Research Facility," National Aeronautics and Space Administration, 1987.
- [5] J. Simisiriwong, *Structural Testing of an Ultralight UAV Composite Wing and Fuselage*, Mississippi State University: Department of Aerospace Engineering, 2009.
- [6] D. J. Ewins, *Modal Testing: theory, practice, and application*, 2nd Edition, Baldock, Hertfordshire, England: Research Studies Press Ltd., 2000.
- [7] M. Friswell and J. E. Mottershead, *Finite Element Model Updating in Structural Dynamics*, Dordrecht, Netherlands: Kluwer Academic Publishers, 1995.
- [8] M. Rades, *Mechanical Vibrations II: Structural Dynamic Modeling*, 2010.
- [9] R. J. Allemang, "The Modal Assurance Criterion (MAC): Twenty Years of Use and Abuse," in *20th International Modal Analysis Conference*, Los Angeles, CA, 2002.

- [10] S. Perinpanayagam and D. J. Ewins, "Free-Free, Fixed or Other Test Boundary Conditions," in *21st International Modal Analysis Conference*, Kissimmee, FL, 2003.
- [11] B. Peeters, J. Deblille and H. Climent, "Modern Solutions for Ground Vibration Testing of Small, Medium and Large Aircraft," *SAE International Journal of Aerospace*, vol. 1, pp. 732-742, 2009.
- [12] M. W. Kehoe and L. C. Freudinger, "Aircraft Ground Vibration Testing at the NASA Dryden Flight Research Facility," National Aeronautics and Space Administration, Edwards, CA, 1993.
- [13] G. A. Fleming and R. D. Buehrle, "Modal Analysis of an Aircraft Fuselage Panel using Experimental and Finite-Element Techniques," in *3rd International Conference on Vibration Measurements by Laser Techniques*, Ancona, Italy, 1998.
- [14] T. G. Carne and C. R. Dohrmann, "A Modal Test Design Strategy for Model Correlation," in *13th International Modal Analysis Conference*, Nashville, TN, 1995.
- [15] C. Stephan, "Sensor Placement for Modal Identification," *Mechanical Systems and Signal Processing*, vol. 27, pp. 461-470, 2011.
- [16] D. C. Kammer and M. L. Tinker, "Optimal Placement of Triaxial Accelerometers for Modal Vibration Tests," *Mechanical Systems and Signal Processing*, vol. 18, pp. 29-41, 2004.
- [17] M. Stabb and P. Blelloch, "A Genetic Algorithm for Optimally Selecting Accelerometer Locations," in *13th International Modal Analysis Conference*, Nashville, TN, 1995.
- [18] E. Balmes, "Orthogonal Maximum Sequence Sensor Placements Algorithms for Modal Tests, Expansion and Visibility," in *24th International Modal Analysis Conference*, Orlando, FL, 2005.
- [19] R. B. Jenal, W. J. Staszewski, A. Klepka and T. Uhl, "Structural Damage Detection Using Laser Vibrometers," in *2nd International Symposium NDT Aerospace*, Hamburg, 2010.
- [20] J. Lawson and J. Erjavec, *Modern Statistics for Engineering and Quality Improvement*, Pacific Grove, CA: Duxbury, 2001.

- [21] M. W. Kehoe, "A Historical Overview of Flight Flutter Testing," National Aeronautics and Space Administration, 1995.
- [22] C. De Marqui Jr., D. C. Rebolho, E. M. Belo and F. D. Marques, "Identification of flutter parameters for a wing model," *Journal of the Brazilian Society of Mechanical Sciences and Engineering*, vol. 28, no. 3, pp. 339-346, 2006.
- [23] J. R. Wright and J. E. Cooper, *Introduction to Aircraft Aeroelasticity and Loads*, Chichester, West Sussex, England: John Wiley & Sons Ltd., 2007.
- [24] C. Hebert, D. Cowan, P. J. Attar and C. D. Weisman, "Exploring Structural Dynamics," American Institute of Aeronautics and Astronautics.
- [25] R. Lind, "Flight-Test Evaluation of Flutter Prediction Methods," *Journal of Aircraft*, vol. 40, no. 5, pp. 964-970, 2003.
- [26] J. E. Cooper, P. R. Emmett, J. R. Wright and M. J. Schofield, "Envelope Function: A Tool for Analyzing Flutter Data," *Journal of Aircraft*, vol. 30, no. 5, pp. 785-790, 1993.
- [27] N. H. Zimmerman and J. T. Weissenburger, "Prediction of Flutter Onset Speed Based on Flight Testing at Subcritical Speeds," *Journal of Aircraft*, vol. 1, no. 4, pp. 190-202, 1964.
- [28] R. Lind and M. Brenner, "Flutterometer: An On-Line Tool to Predict Robust Flutter Margins," *Journal of Aircraft*, vol. 37, no. 6, pp. 1105-1112, 2000.
- [29] J. Cecrdle, J. Malacek and O. Cerny, "Aeroelastic Analysis of Twin Turboprop Utility Aircraft," *Journal of Aerospace Engineering*, vol. 225, no. 5, 2010.
- [30] J. Lau, B. Peeters, J. Debille, Q. Guzek, W. Flynn, D. S. Lange and T. Kahlmann, "Ground Vibration Testing Master Class: modern testing and analysis concepts applied to an F-16 aircraft," in *29th International Modal Analysis Conference*, Jacksonville, FL, 2011.
- [31] M. W. Kehoe, "Aircraft Flight Flutter Testing at the NASA Ames-Dryden Flight Research Facility," National Aeronautics and Space Administration, Edwards, CA, 1988.

- [32] B. Peeters, P. De Baets, L. Mosenich, A. Vecchio and H. Van der Auweraer, "Ground Vibration Testing in the Aeroelastic Design and Certification of a Small Composite Aircraft," in *American Institute of Aeronautics and Astronautics*, 2005.
- [33] C. Wojciech, "Flutter Calculation Based on GVT: results and theoretical mass model," *Aviation*, vol. 13, no. 4, p. 122, 2009.
- [34] C. R. Pickrel and P. J. White, "Flight Flutter Testing of Transport Aircraft: In-Flight Modal Analysis," in *21st International Modal Analysis Conference*, Kissimmee, FL, 2003.
- [35] A. Kayran, "Flight Flutter Testing and Aeroelastic Stability of Aircraft," *Aircraft Engineering and Aerospace Technology: An International Journal*, vol. 79, no. 5, pp. 494-506, 2007.
- [36] S. Potter and R. Lind, "Developing Uncertainty Models for Robust Flutter Analysis Using Ground Vibration Test Data," NASA Dryden Flight Research Center, Edwards, CA, April 2001.
- [37] L. C. Freudinger, "Flutter Clearance of the F-18 High-Angle-of-Attack Research Vehicle With Experimental Wingtip Instrumentation Pods," National Aeronautics and Space Administration, Edwards, CA, 1989.
- [38] J. Song, T. Kim and S. J. Song, "Experimental Determination of Unsteady Aerodynamic Coefficients and Flutter Behavior of a Rigid Wing," *Journal of Fluids and Structures*, vol. 29, pp. 50-61, 2012.